

Characterization and Catalytic Activity Study of
SBA-15-supported MoO_3 , MoS_2 , Ni or Co promoted
 MoS_2 and Co promoted WS_2



A thesis submitted to the

Faculty of Mathematics and Natural Sciences of the
Christian-Albrechts-Universität zu Kiel

for the degree of
Doctor rer. nat.

presented by

Zhida Huang

Kiel, May 2008

Examiner: Prof. Dr. Wolfgang Bensch,

Co-examiner: Prof. Dr. Norbert Stock,

Date of the oral examination: July 3th, 2008

To print approved: July 16th, 2008

The Dean

Affirmation

I declare that the work presented here was performed by myself, under the supervision of my scientific tutor, only using the devices, resources and media mentioned in the thesis. The PhD thesis is solely submitted to the University of Kiel.

Zhida Huang

Kiel, May 2008.

Zusammenfassung

Die Entschwefelungskatalysatoren (HDS-Katalysatoren) wurden durch thermische Zersetzung von (Alkyl)-Ammoniumthiomolybdat bzw. Ammoniumthiowolframat auf SBA-15 (6 und 9 nm) als Trägermaterial hergestellt. Vor den katalytischen Tests wurden die HDS-Katalysatoren entweder in einem H_2/N_2 -Gasstrom bei 773 K (*ex-situ*-Aktivierung) oder während der katalytischen Tests (*in-situ*-Aktivierung) aktiviert. Die Ergebnisse belegen, dass die Morphologie der MoS_2 -basierten Katalysatoren und somit auch die HDS-Aktivität empfindlich von den verwendeten Thiosalzen, der Imprägnierungsmethode und den Aktivierungsprozeduren abhängen. Die durch thermische *ex-situ*-Zersetzung von Ammoniumthiomolybdat (ATM) erhaltenen Katalysatoren (Ni)CoMo/SBA-15 zeigen bei hohem Mo-Beladungsgrad trotz einer vergleichsweise großen Anzahl an MoS_2 -Slabs (6 - 8 Schichten) eine höhere oder ähnliche katalytische Aktivität im Vergleich mit einem kommerziellen HDS-Katalysator auf $\gamma\text{-Al}_2\text{O}_3$ als Trägermaterial. Eine Schlussfolgerung der Untersuchungen ist, dass die Anzahl an MoS_2 -Slabs nicht die entscheidende Voraussetzung für eine hohe HDS-Aktivität ist. Die hohe HDS-Aktivität könnte jedoch auf das Vorhandensein einer großen Anzahl koordinativ ungesättigter Plätze (CUS) im MoS_2 zurückgeführt werden. Bei der Verwendung von Tetramethylammoniumthiomolybdat (TMATM) als Mo-Quelle führt die *ex-situ*-Aktivierung zur Bildung von fullerenartigen oder nanozwiebelartigen (Ni) MoS_2 - und nadelartigen (Co) MoS_2 -Strukturen, die weniger katalytisch aktive Zentren aufweisen und daher eine geringere HDS-Aktivität zeigen. Die katalytischen Tests haben auch ergeben, dass die *in-situ*-Aktivierung die günstigste Vorgehensweise zur Herstellung von CoMo/SBA-15 Katalysatoren ist, wenn kohlenstoffhaltige Mo-Thiosalze wie TMATM verwendet werden. Für die Herstellung von HDS-Katalysatoren auf der Basis von NiMo führt die *in-situ*-Aktivierung zu aktiveren Materialien als die *ex-situ*-Aktivierung aufgrund der positiven Kohlenstoffeffekte. Die Art des Thiosalzes und die Aktivierungsmethode haben nur einen geringen Einfluss auf die HDS-Selektivitäten.

MoO_3 /SBA-15 wurde durch Imprägnierung von SBA-15 mit Ammoniumheptamolybdat und anschließender Kalzinierung bei 773 K hergestellt. Die Bildung von metastabilem hexagonalem MoO_3 konnte mit EXAFS nachgewiesen werden. Das katalytische Verhalten von hex- MoO_3 /SBA-15 wurde in der Propenoxidationsreaktion untersucht. Dabei

hat sich interessanterweise ergeben, dass hex-MoO₃/SBA-15 über einen weiten Temperaturbereich stabil ist und eine deutlich höhere Aktivität und Selektivität aufweist als das stabile orthorhombische α -MoO₃. Ohne Zugabe anderer Übergangsmetalle wie W, V und Nb ist die Bildung von Acrylsäure bei der katalytischen Reaktion nachweisbar. Es konnte gezeigt werden, dass die offene Kanalstruktur von hex-MoO₃ eine entscheidende Rolle bei der Erzeugung neuer katalytischer Aktivitätszentren spielt.

Abstract

Hydrodesulfurization (HDS) catalysts supported on SBA-15 (6 and 9 nm) were prepared by thermal decomposition of (alkyl)ammonium thiomolybdate and ammonium thio tungstate using Co(Ni) acetate or Co(Ni) thiocarbamate (cobalt dimethyldithiocarbamate and nickel diethyldithiocarbamate) as the promoter atom sources. Prior to the catalytic test, the activations of the catalysts were carried out either under H₂/N₂ gas flow at 773 K (*ex-situ* activation) or during the catalytic tests (*in-situ* activation). The nature of the thiosalt precursor, the impregnation method as well as the activation mode show a strong influence on the MoS₂ morphology, which is of great importance for the HDS catalytic activity. Despite the high MoS₂ stacking, the *ex-situ* activated catalysts derived from ammonium thiomolybdate (ATM) at high Mo-loading exhibit higher HDS activity compared to a commercial γ -Al₂O₃-supported HDS catalyst. One important result of the studies is that the MoS₂ stacking is not a prerequisite for a good HDS performance and also not a sign for the deactivation or lower HDS activity. The presence of large amounts of coordinatively unsaturated sites (CUS) could be responsible for the high HDS activity. The experiments clearly show that the *ex-situ* activation is not beneficial for the preparation of HDS active phases when a carbon-containing Mo source like tetramethyl-ammonium thiomolybdate (TMATM) is employed. During the activation process MoS₂ particles with an unfavorable morphology are generated and big needle-like aggregates and closed shell structures are seen in the HRTEM pictures. The *in-situ* activation is found to be beneficial for the preparation of NiMo/SBA-15 catalysts with high activity. For CoMo/SBA-15 catalysts, the *in-situ* activation also results in an enhanced synergetic effect of Co by using TMATM. In this case, the improved HDS performance could be associated with the positive carbon effect. In contrast, the nature of the thiosalt precursor and the activation mode have only a negligible influence on the catalytic selectivity.

MoO₃ supported on SBA-15 was prepared by impregnation of SBA-15 with ammonium heptamolybdate followed by calcination at 773 K for 3 h in air. Interestingly, the presence of the hexagonal MoO₃ modification was unequivocally identified by evaluation of the EXAFS data. In addition, the catalytic behavior of the hex-MoO₃/SBA-15 in the propene oxidation reaction was investigated in the temperature range from 293 K to 773 K. The stabilized hex-MoO₃-SBA-15 is shown to be capable of directly oxidizing propene to acrylic

acid without the addition of further metal atoms as promoters. Intriguingly, the stabilized structure of hexagonal MoO_3 supported on SBA-15 possesses an open channel structure similar to that of the highly active Mo_5O_{14} or MoVNbTe catalysts. Hence, structural complexity of molybdenum oxides is sufficient to improve functional molybdenum sites for the activation of oxygen and alkene followed by selective oxidation of the alkene.

Contents

1	Introduction	1
1.1	Hydrodesulfurization (HDS)	1
1.1.1	HDS catalysts	4
1.1.2	The active sites of the HDS catalysts	7
1.1.3	The carbon effect and the chelate effect	12
1.2	Propene oxidation	13
2	Motivation	15
3	Experimental section	17
3.1	Characterization methods	17
3.1.1	The X-ray absorption spectroscopy (XAS)	17
3.1.2	Gas adsorption	18
3.1.3	Transmission electron microscopy (TEM)	23
3.1.4	High-angle annular darkfield (HAADF) technique	26
3.1.5	Chemical elemental analysis	26
3.1.6	FT-Raman spectroscopy	26
3.1.7	X-ray powder diffraction (XRD)	26
3.2	Catalytic activity test of HDS of DBT	26
4	Results and Discussion	29
4.1	SBA-15 as support for Mo and W sulfide based HDS catalysts	29
4.1.1	Characterization and HDS activity investigation of MoS ₂ /SBA-15 and (Ni)CoMo/SBA-15 using cobalt or nickel acetate as precursor	29
4.1.2	Characterization and HDS activity investigation of (Ni)CoMo/SBA-15 using cobalt(nickel) thiocarbamate as precursor	44
4.1.3	(Ni)CoMo/SBA-15 and CoW/SBA-15 catalysts prepared by the solvent evaporation route	91
4.1.4	Ti modified SBA-15 as support for HDS catalysts	94
4.2	SBA-15 as support for MoO ₃ catalysts	97

5	Conclusions	118
6	Appendix	120
6.1	Acknowledgements	120
6.2	List of Publications	121
6.3	Curriculum Vitae	123
	References	124

1 Introduction

Heterogeneous catalytic processes are one of the vital important technologies in the industry. In heterogeneous catalytic reactions, one or more of the reactants must be adsorbed at the surface of a catalyst and the products must diffuse away from the catalyst surface after the reaction. Therefore, the catalytic activity may strongly depend on the catalyst surface area. Since the discovery of mesoporous silicas (MCM-41 or MCM-48, the M41S family) by a group of Mobil scientists [1,2], such materials attract more and more attention for the application as support material for catalysts. In the meantime, new mesoporous phases including SBA-15, SBA-16 and others were prepared using triblock copolymers surfactants as structure directors [3,4]. These materials have some advantages compared to the members of MS41 family, like thicker pore walls and a higher stability under hydrothermal conditions.

Mesoporous silicas are applied as support for catalysts for several reasons. First, the large surface area (ca. $1000 \text{ m}^2 \text{ g}^{-1}$) increases the probability that a reactant molecule will come in contact with the catalyst surface and can be adsorbed. Secondly, the large pore size (2 - 20 nm) and ordered pore morphology ensure the reactant molecules diffusing into the pores. Finally, an enhanced catalytic activity may be achieved due to changes of the catalysts morphology because of specific interactions between the support and the catalyst.

1.1 Hydrodesulfurization (HDS)

Air pollution has become a serious problem in the recent years. One type of air pollution is the emission of noxious gases, such as sulfur dioxide, carbon monoxide, nitrogen oxides and chemical vapors. The exhaust from burning fuels sources in automobiles, homes and industries is a major source of air pollution. The two important burning fuels sources, fuel oil and gasoline (petrol), are produced from petroleum (crude oil), which is a naturally occurring liquid found in formations in the earth consisting of a complex mixture of hydrocarbons (mostly alkanes) of various lengths. In addition, petroleum contains also varying amounts of heteroatoms such as sulfur, nitrogen, oxygen and metals (predominantly vanadium and nickel). Depending on the crude origin, oil fractions in the diesel

boiling range contain between 0.1 and 1.5 wt.% sulfur, appearing as thiols, sulfides, disulfides and organosulfurs such as thiophenes, benzothiophenes and the dibenzothiophenes. Upon combustion, these sulfur compounds generate sulfur oxides pollution which is responsible for the generation of acid rain. For this reason (initially only for this reason) the sulfur in diesel fuels has long been an issue. Since the nineties, the discussion on sulfur emission changed and the total pollution was taken into account. Sulfur components have also been found to be one of the important poisons for the catalytic converters used for exhaust emission treatment in modern engines even in extremely low concentrations. Therefore, increasingly stringent environmental regulations were decided in the US and EU to reduce the sulfur content in diesel and gasoline to the lower level around 10 - 15 ppm [5] (Fig. 1). Furthermore, the tendency towards "zero sulfur" fuels will be rapidly becoming dominant in the near future [6].

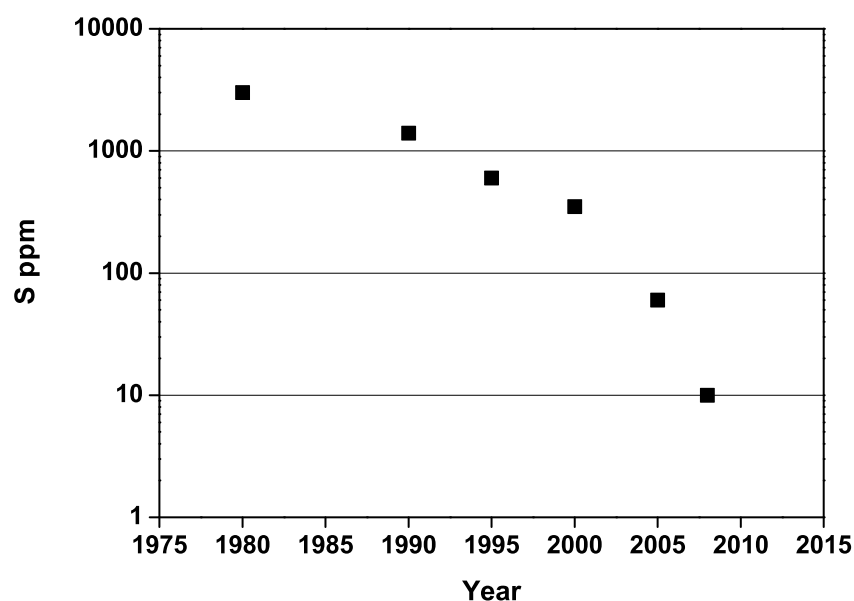


Fig. 1: Sulfur specifications in diesel oil (EU) from [5]

Hydrotreating refers to a series of hydrogenation reactions for the saturation of a variety of unsaturated hydrocarbons and for the removal of unwanted heteroatoms such as nitrogen (Hydrodenitrogenation, HDN), oxygen (hydrodeoxygenation, HDO) and metals

(hydrodemetalation, HDM). Hydrodesulfurization (HDS) is the most thoroughly studied and the most important reaction overall "hydrotreating processes" which is a catalytic chemical process widely used to remove sulfur from natural gas and refined petroleum products [7]. Compared to some easily removable sulfur compounds such as the thiols, sulfides and disulfides, the removal of (di)benzothiophenes (DBT) and alkyl-substituted (di)benzothiophenes is more difficult under the standard hydrotreating conditions [8]. This is a great challenge and a satisfactory solution has not yet been found. Generally, two important approaches can be applied to provide clean transportation fuels meeting the increased demanding requirements through the "deep desulfurization":

- modification of the operating conditions for hydrotreaters with respect to the reaction temperature and liquid hourly space velocity (LHSV);
- improvement of the activity of the HDS catalysts.

However, a high reaction temperature leads to rapid catalytic deactivation by coke formation and low LHSV results in decreased hydrotreating efficiency, thus, requiring additional reactor capacity. Consequently, the economical way to achieve the deep HDS is the development of a HDS catalyst with high catalytic activity. Recently, the applications of NEBULA and the KF STARS catalysts (Fig. 2) as well as the combination of both catalysts have enabled refiners to produce ultra low sulfur diesel (ULSD) to meet the new fuel specifications in time [5].

In a high pressure experiment, DBT is one of the most non-reactive sulfur compounds in higher boiling fractions of fossil fuels. It is commercially available and therefore it represents a good model compound for characterizing the HDS chemistry of heterocyclic sulfur compounds. The challenge for deep desulfurization of diesel fuel had stimulated numerous studies on the transformation of heavy refractory compounds and it is now admitted that the HDS of DBT can occur via two reaction pathways (Fig. 3):

- direct desulfurization (DDS) via C-S bond cleavage leading to the formation of biphenyl (BP);
- hydrogenation (HYD) to form phenylcyclohexane (PCH) as illustrated in Fig. 3. PCH is a secondary product yielded from the desulfurization of tetrahydrodibenzothiophene (TH-DBT) and hexahydrodibenzothiophene (HH-DBT).

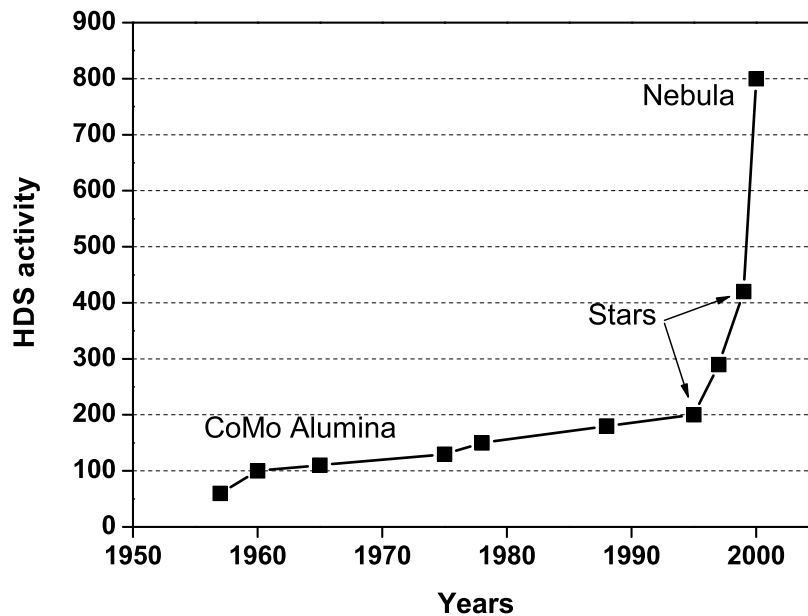


Fig. 2: Development of the HDS activity during the last fifty years [5]

Generally, the catalytic selectivity determined from the ratio between HYD and DDS can be approximated by: $S_{HYD}/S_{DDS} = ([PCH] + [TH-DBT])/[BP]$.

1.1.1 HDS catalysts

The most commonly used industrial hydrotreating catalysts are alumina supported transition metal sulfides, mainly molybdenum and tungsten disulfides promoted with cobalt or nickel. Generally, these hydrotreating catalysts are prepared via an oxide route. γ - Al_2O_3 is impregnated with transition metal salts like ammonium heptamolybdate, nickel (cobalt) nitrate or nickel (cobalt) acetate. The impregnated material is then calcined at elevated temperatures to produce stable oxides. The oxides must then be sulfided either prior to or during the start-up of the hydrotreatment process in a stream of H_2S (15%) in H_2 . The Co-Mo catalysts exhibit excellent HDS activity whereas Ni-Mo catalysts as well as Ni-W catalysts show a better performance for the HDN reaction, which is a competitive reaction for HDS. The concentration of cobalt or nickel are usually 1 - 5 wt.%, and the molybdenum content is commonly present in the 8 to 15 wt.% range (tungsten: 12 - 25

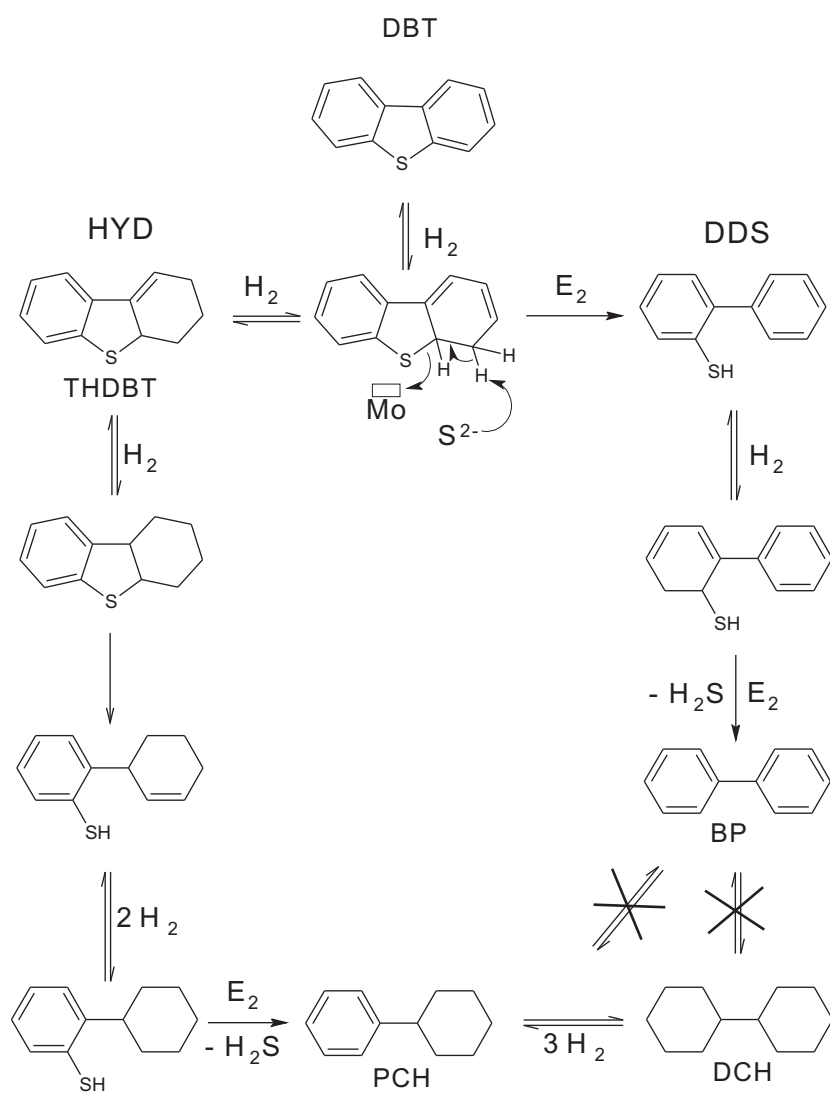


Fig. 3: Reaction network of the HDS of DBT from reference [9].

wt.%) [7, 10].

The origin of the most exclusive usage of alumina as support has to be ascribed to its outstanding textural and mechanical properties, its relatively low cost and furthermore to its ability to generate the catalytic activities. Nevertheless, recent studies have shown that alumina is not an inert support [11, 12]. Depending on the preparation conditions, the promoter ions, Co and Ni, can react with alumina to form catalytic inactive phases like CoAl_2O_4 and NiAl_2O_4 [11]. Recently, Carrier *et al.* [12] reported the formation of an Anderson-type heteropolymolybdate $[\text{Al}(\text{OH})_6\text{Mo}_6\text{O}_{18}]$ when heptamolybdate was deposited on alumina by the equilibrium adsorption method, indicating the strong interaction between molybdenum and the support. The metal-support interactions have a strong influence on the generation of catalytic active sites which was pointed out by Candia *et al.* [13] who assumed that the CoMoS-I phase (with Mo-O-Al anchors) is formed at low sulfiding temperatures and more CoMoS-II phase (without Mo-O-Al anchors) is obtained with increasing sulfiding temperatures. Moreover, the CoMoS-II phase represents much higher catalytic activity than the CoMoS-I phase. Consequently, many researchers investigated other metal oxide supports, such as TiO_2 , ZrO_2 and MgO . However, the surface area and the textural properties of these oxides must be improved. Several combinations of mixed oxides like $\text{SiO}_2\text{-Al}_2\text{O}_3$, $\text{SiO}_2\text{-TiO}_2$, $\text{SiO}_2\text{-ZrO}_2$, $\text{ZrO}_2\text{-TiO}_2$ and $\text{TiO}_2\text{-Al}_2\text{O}_3$ have been studied to increase the small surface areas of TiO_2 and ZrO_2 [14].

In the recent time the attention is shifted to zeolithes and mesoporous materials like MCM-41 and SBA-15 because of their acidity, well-defined hexagonal ordered pore structures and narrow pore diameters (3 - 30 nm). MCM-41 and SBA-15 have very high surface areas (more than $700 \text{ m}^2/\text{g}$) and offer several advantages in comparison with alumina. MCM-41 supported $\text{Co}(\text{Ni})\text{Mo}(\text{W})$ catalysts were investigated in the last decade [15–32]. The catalysts exhibited higher activities for conversion of DBT and petroleum residues than $\text{Co}(\text{Ni})\text{Mo}/\gamma\text{-Al}_2\text{O}_3$ at high molybdenum loading or high atomic ratios of $\text{Co}(\text{Ni})\text{-Mo}$ [28, 30]. Mesoporous SBA-15 presents larger pores, thicker pore walls and higher hydrothermal stability compared to MCM-41. Vradman *et al.* demonstrated the excellent potential of high loaded $\text{NiW}/\text{SBA-15}$ catalysts for deep hydrotreatment of petroleum feedstocks. An ultrasonication method was applied for the direct introduction of crystalline MoS_2 and WS_2 into the mesopores of SBA-15 [33]. SBA-15 was also found to be

a suitable support for Mo, CoMo, and NiMo catalysts by Rao *et al.* [34]. Furthermore, Al-, Ti- and Zr-containing SBA-15 supported NiMo catalysts were prepared by Klimova *et al.* [35,36] and Rao *et al.* [37]. Both groups observed that the modification of SBA-15 with these hetero-atoms (Al, Ti or Zr) provides better dispersion for the deposited Ni and Mo active species resulting consequently in a high activity for HDS of DBT.

Unsupported Ni/Co-Mo/W sulfides have also been reported by a large number of groups because such unsupported catalysts are more suitable for specific studies by advanced analytical techniques than their supported counterparts [38]. In other words, unsupported Ni/Co-Mo/W sulfides catalysts offer the possibility to study the effect of stacking of MS_2 slabs ($M = Mo, W$), the curvature of the MS_2 layers and the acidity/basicity of the MS_2 surface onto the catalytic activity. But compared to supported catalysts such unsupported materials are much more costly because a higher concentration of metals and higher density is needed. Therefore, only a few unsupported catalysts are commercially available in the present hydroprocessing market despite the appearance of a large amount of patents covering the large variety of developed unsupported catalysts [38]. The NEBULA catalysts family, representing a totally new technology developed by Albemarle Catalysts (former Akzo Nobel Catalysts) and ExxonMobil, is the only one group of unsupported commercial bulk hydroprocessing catalysts.

1.1.2 The active sites of the HDS catalysts

The structure of the thermodynamic stable crystalline MoS_2 is well known. Mo^{IV} ions are surrounded by six S atoms in the form of a trigonal prism. The MoS_6 prisms share common edges yielding layers which are stacked onto each other parallel to the crystallographic c axis. The interactions between the MoS_2 slabs are weak and of the van der Waals type (Fig. 4).

However, the structure and the exact nature of the catalytically active HDS sites of standard catalysts are still difficult to achieve due to the high dispersed catalytic particles (amorphous-like) and the presence of different types of phases. In the last decades, many surface sensitive techniques and analytical tools like scanning tunneling microscopy (STM) [39–41], transmission electron microscopy (TEM), Mössbauer spectroscopy [11,42] and extended X-ray absorption fine structure analyses (EXAFS) [42–45] as well as pow-

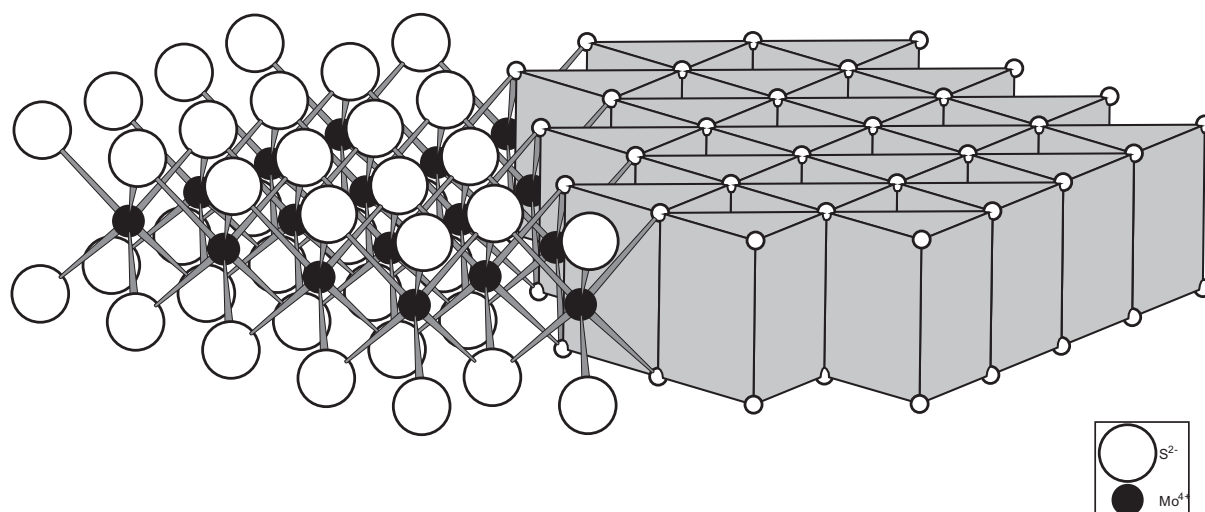


Fig. 4: MoS₂ structure

erful theoretical methods like density functional theory (DFT) [39, 40, 46, 47] have been extensively employed in order to tackle this complex problem. Several important models have been developed which are shortly summarized:

Co-Mo-S model

The most widely accepted model of the structure of promoted HDS catalysts is the Co-Mo-S model, which was proposed by Topsøe *et al.*. Several analytical methods like *in-situ* Mössbauer emission spectroscopy, EXAFS and infrared spectroscopy were applied to develop this model [11]. Depending on the relative concentration of cobalt or nickel and molybdenum and on the synthesis conditions, cobalt(nickel) atoms adopt three possible types of structures after sulfidation (Fig. 5):

- the so-called Co-Mo-S phase where the promoter atoms Co/Ni are adsorbed on the edges of MoS₂ crystallites (monolayer model);
- stable metal sulfides Co₈S₉ or Ni₃S₂ are formed on the support material (contact synergy model, see the following section);
- Co and Ni ions coordinated at the lattice sites of the support material (interaction model).

EXAFS and XRD results showed for $\text{CoMo}/\gamma\text{-Al}_2\text{O}_3$ catalysts that the Mo atoms are predominantly present in the MoS_2 structure, and the MoS_2 particles are present in the form of very small (1 nm) domains or crystallites. The results of combined activity/spectroscopy investigations clearly demonstrate that the catalytic activity is related to the fraction of Co atoms being present as Co-Mo-S phase. This structure model seems to be applicable for other related HDS catalysts such as Ni-Mo-S, Ni-W-S and Co-W-S. The precise position of promoter atoms and the exact structure of the catalysts are still under debate. EXAFS has provided direct structural information regarding the oxidation state and environment of Mo and Co. One model that is consistent with EXAFS data was proposed by Topsøe *et al.* [11]: Ni(Co) atoms are located at the substitution sites on the MoS_2 edges. The square pyramidal coordination of the Ni(Co) resembles that of the Millerite type structure, in which Co atoms are connected to the MoS_2 crystallite by four sulfur atoms, and an additional sulfur atom is attached in front of the Co atoms, as shown in Fig. 5.

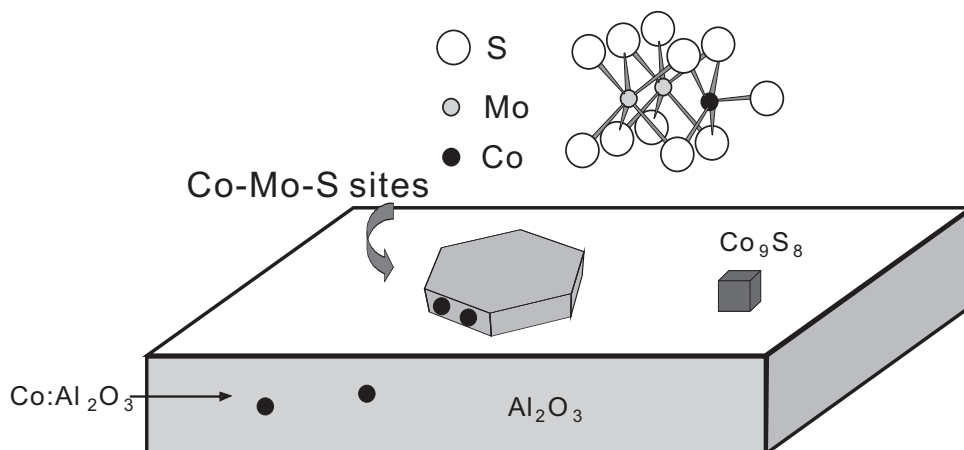


Fig. 5: Schematic representation of Topsøe’s Co-Mo-S model for a typical alumina-supported catalyst with the $\text{Mo}_2\text{CoS}_{11}$ unit at the edge of the Co-Mo-S site [7]

Concept of CUS

The concept of coordinatively unsaturated sites (“CUS” or “vacancies”) is a key element in the generation of the active sites during actual catalytic processes [7]. The CUS concentration has been claimed to be responsible for the high HDS activity and selectivity.

Such CUS-sites are thought to be created in the reducing atmosphere of H_2 , the “empty” coordination sites are generated after the formation of H_2S during the reaction of H_2 with surface sulfide groups. The presence of such CUS on the catalyst surface provides an enhancement for the ability of adsorption of sulfur from organosulfur compounds. It should be noted that the sulfur vacancies are expected to be Lewis acid sites and not to Brønsted acid sites [48]. According to the Co-Mo-S model, the apical sulfur atom on the square pyramidal structure around Co is known to be loosely bound and could be easily removed to create the necessary vacancies. It is well known that the impregnation of the promoter atoms such as Co and Ni leads to a strong enhancement of the HDS activity which is called synergistic effect [7].

Concept of “remote control”

According to the models discussed in the preceding sections, most of the catalytic activity is not associated with separated Co_9S_8 or NiS_x but with the promoter atoms in the Co-Mo-S phase. However, catalysts containing little or no “Me-Mo-S” (Me = Ni, Co) phase were found to be quite highly active. A remote control mechanism has been proposed by Delmon *et al.* [49] to explain this phenomenon: hydrogen is dissociated to spill-over hydrogen H_{SO} on Co_9S_8 or NiS_x . The generated H_{SO} migrates onto the surface of the other catalytic phase (MoS_2 , “Co-Mo-S”) creating catalytic centers on this phase.

Rim-Edge model

Nowadays the researchers pay a lot of attention to the edges of MoS_2 . The so-called Rim-Edge model was proposed by Daage and Chianelli in 1994 [50] to explain the relations between the MoS_2 morphology and the catalytic properties in unsupported molybdenum sulfide catalysts. The catalyst particles are treated as a stack of several discs. The rim sites refer to the top and bottom discs and the discs “sandwiched” between the top and bottom discs are viewed as the edge sites (Fig. 6). Sulfur hydrogenolysis occurs on both rim and edge sites, whereas the hydrogenation of DBT occurs exclusively on rim sites. Compared to these two catalytic active sites the basal plane has been shown to be catalytically inactive.

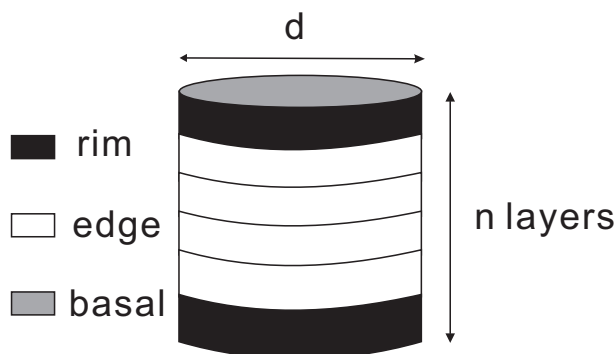


Fig. 6: Rim-edge model for unpromoted MoS₂ catalysts, from reference [50]

Brim sites

Recently, the scanning tunneling microscopy (STM) has been applied to investigate the real active phase in HDS catalysts [39–41]. With the aid of the STM technique, the atomic scale structures of unpromoted MoS₂, Co-Mo-S as well as Ni-Mo-S were reported by Besenbacher *et al.*, who obtained the images of such nanoclusters grown on a Au(111) surface. The important findings were the discovery of the so-called brim sites. It was shown that the (10 $\bar{1}$ 0) Mo edge exhibits a special electronic edge state, which can easily be identified in STM images of the nanoclusters as a very brim extending along the edges. These brim sites have a metallic character and are localized at the cluster edges. Unpromoted MoS₂ has shown a very regular triangular shape. A distinct change in morphology was observed if the promoter atoms Co or Ni are added. Co-Mo-S nanoclusters adopt a clear hexagonally truncated shape with Co atoms preferentially located at ($\bar{1}$ 010) edges with a 50% S coverage. For the Ni-Mo-S system the nature of the truncation depends on the cluster size. The large clusters (type A) are characterized by a hexagonally truncated shape similar to that of Co-Mo-S nanoclusters exposing fully Ni-substituted ($\bar{1}$ 010) edges with a 50% S coverage. On the other hand, the smaller clusters (type B) have a more complex dodecagonal morphology which was found to be terminated by 3 types of edges: the ($\bar{1}$ 010) edge, the (10 $\bar{1}$ 0) edge and a high-index (11 $\bar{2}$ 0) edge, all of which contain Ni promoter atoms fully or partially substituting the Mo atoms. The findings may shed more light on the different selectivities observed for the Co and Ni promoted hydrotreating catalysts. Nevertheless, it should be mentioned that the nanoclusters used for the STM investigations were prepared under very special experimental conditions, which are

very different from the conventional synthesis conditions of HDS catalysts.

1.1.3 The carbon effect and the chelate effect

A positive effect of carbon on the activity of hydrotreating catalysts has long been recognized. An increase of the catalytic activity has been observed by using carbon-containing sulfiding agents such as CS_2 , RSH and $\text{CH}_3\text{-S-S-CH}_3$ instead of $\text{H}_2/\text{H}_2\text{S}$. The positive role of C-containing molecules during the sulfidation process could be ascribed to two important effects [51]:

- A support effect where carbon species may be intercalated between the carrier and the active sulfide phase, resulting in a reduced interaction of the active phase with the support and, in turn, in an enhanced activity. Carbon covered alumina catalysts have already been reported to enhance the hydrotreating properties.
- A chemical effect, i.e., a more active carbide-like structure denoted as “CoMoC” may be formed at the surface of the sulfide particles.

But carbon deposited on the surface of the catalyst has been stated as one cause of catalysts deactivation. As reported by Nava *et al.* [52], excess carbon could hamper the interaction between the promoter atoms Co/Ni and Mo/W and block the migration of promoter atoms to Mo(W) S_2 edges.

Remarkable improvements of the HDS activity of CoMo, NiMo and NiW catalysts can be achieved by adding some chelating compounds such as nitriloacetic acid (NTA) or ethylene diamine tetraacetic acid (EDTA) to the impregnation solution. Such catalysts are characterized by the formation of the highly active Co-Mo-S type II sites with an extremely high selectivity [53–55]. On alumina the Co-Mo-S type II phase is present as a multilayer structure, whereas type I exists as a single-slab (monolayer) structure [56]. These chelating ligands have been found to screen the Ni cations and prevent their interactions with the support. Moreover, Ni sulfidation is delayed resulting in the simultaneous sulfidation of the promoter and Mo/W and, therefore, in less promoter segregation [57].

1.2 Propene oxidation

Propene oxidation is one of the catalytic selective partial oxidations which belong to the most important industrial processes. About 25% of all organic products worldwide are synthesized via selective partial oxidations. Propene oxidation has been highly developed because of the high economic importance. Molybdenum and vanadium oxide catalysts are commonly used for the selective oxidation reactions. Industrially, acrylic acid is obtained by the selective oxidation of propene [58] (Fig. 7):

- The dehydrogenation of propane to propene proceeds in the presence of a vanadium based oxide or platinum catalyst;
- the selective oxidation of propene into acroleine in the presence of a BiMo oxide catalyst;
- and the subsequent oxidation of acroleine into acrylic acid in the presence of a MoVW oxide catalyst.

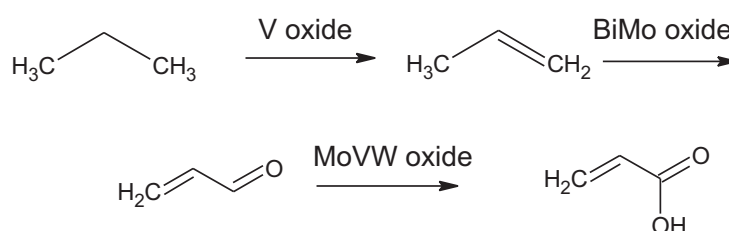


Fig. 7: Industrially utilized selective oxidation catalysts [58]

Moreover, MoVTeNb oxides can promote a direct conversion of propane into acrylic acid which is the desired process for future application in industry. Recently, Grasselli [59,60] summarized seven fundamental principles important for selective heterogeneous oxidation catalysis, the so-called "seven pillars": lattice oxygen, metal oxygen bond strength, host structure, redox, multifunctionality of active sites, site isolation and phase cooperation.

1. Lattice oxygen: the flexible coordination geometry of transition metals and the variability of the valence of metal atoms facilitate the lattice oxygen transfer between bulk metal oxide and species adsorbed on the oxide surface.

2. Metal oxygen bond strength: this determines the oxidizing power of the surface lattice oxygen.
3. Host structure: the structure of the host material should accommodate the desired lattice oxygen(s) and concomitant desired metaloxygen.
4. Redox properties: the redox reaction takes place in the selective oxidation reaction; regeneration of the reduced metal oxide must be faster than its reduction for the system to function as a catalyst.
5. Site isolation: the amount of surface lattice oxygen atoms at a site determines the stoichiometry of the reaction and the products formed.
6. Multifunctional active sites: different functional sites perform various functions in the catalytic cycle such as chemisorption of the substrate, abstraction of hydrogen from the substrate, insertion of oxygen or nitrogen species into the adsorbed and activated substrate, and desorption of the product.
7. Phase cooperation: in case that the key catalytic functions cannot be incorporated into one single host structure, the next best approach is to find two or more phases containing separately the diverse but necessary functions for a catalytic reaction.

2 Motivation

The hydrotreating catalysts are normally prepared via an oxide route. The support materials like γ -Al₂O₃, MCM-41 or SBA-15 are first impregnated with transition metal salts like ammonium heptamolybdate, nickel (cobalt) nitrate or nickel (cobalt) acetate. The impregnated supports are then calcined to produce stable oxides. In the next step these oxides are activated by *ex-situ* treatment in a stream of H₂S/H₂(15% H₂S) or by an *in-situ* activation in the presence of an organic solvent during the HDS reaction of DBT.

As mentioned above, the silica SBA-15 offers some superior properties compared to the widely used support γ -Al₂O₃: a very large surface area, a narrow and variable pore size distribution and a regular arrangement of the pores. In the past only a few studies were reported using SBA-15 as a support for (W)MoS₂ based HDS catalysts derived from thiomolybdate or thiotungstate compounds as starting material. In addition, an all sulfide synthetic route where oxygen containing precursors are avoided was not explored until now. Furthermore, the application of ammonium heptamolybdate as Mo source leads to an intermediate MoO₃. The structure of this intermediate MoO₃ species supported on SBA-15 is still under debate.

The aims of the present thesis are:

- The preparation and full characterization of promoted SBA-15-supported molybdenum and tungsten sulfide based HDS catalysts using (alkyl)ammonium thiomolybdates or ammonium thiotungstates as precursor materials.
- The promotion of the catalysts with different sources like cobalt(nickel) acetate or cobalt(nickel) thiocarbamate allowing to study the effect of the type of the source onto the structure and catalytic activity.
- Avoidance of the activation of the catalysts in toxic H₂S atmosphere. Instead of the treatment in H₂S, the catalysts are either activated *ex-situ* under a H₂/N₂ (10% H₂) gas flow at 773 K or *in-situ* during the catalytic test.
- Investigation of the pore sizes (6 and 9 nm) of SBA-15 onto the properties and catalytic performance of the materials. Applying a support with two different pore sizes allows a detailed study of the support effect onto the HDS reactions.

- The preparation and full characterization of MoO₃ supported on SBA-15, and test of the material in the propene oxidation reaction.

Further improvements of the catalytic activity are a real challenge for the industrial developer or researcher and can only be achieved if a fundamental understanding is reached about the structures-catalytic activity relationship of the catalysts.

3 Experimental section

3.1 Characterization methods

Various characterization methods were performed to investigate the starting material SBA-15 and the SBA-15-supported catalysts. The characterization techniques are: high resolution transmission electron microscopy (HRTEM), X-ray absorption spectroscopy (XAS), X-ray diffraction (XRD), N₂ physisorption and Fourier transform (FT) Raman spectroscopy.

3.1.1 The X-ray absorption spectroscopy (XAS)

The variation in the absorption coefficient μ of matter with photon energy is explored by the technique of X-ray absorption spectroscopy [61]. Beyond the absorption edge the intensity of a monochromatic X-ray passing through a medium of thickness t will follow Lambert-Beers law:

$$I = I_0 e^{-\mu t} \quad (1)$$

where I is the transmitted intensity, t is the material thickness traversed and I_0 is the incident beam intensity. In general, the absorption coefficient decreases gradually with increasing photon energy until the core-level binding energy is reached, whereupon the absorption spectra show a steep rise. Based on the ejected electron ($E - E_0$), the XAS spectra are usually divided in two regions:

- the X-ray absorption near edge structure (XANES): $\approx 0 - 40$ eV above E_0 where multiple scattering by the first and even higher coordinating shells provide information about chemical states and symmetries.
- the extended X-ray absorption fine structure (EXAFS): $\approx 40 - 1000$ eV where single scattering by the nearest neighboring atoms dominates yielding the information of coordination numbers and inter-atomic distances.

The interference of the ejected photoelectron wave and the backscattered wave (scattered by neighboring atoms) causes the EXAFS oscillations which contain the relevant

information like type of backscatterer atom, interatomic distances and coordination number. The EXAFS function, $\chi(k)$, is described by the following formula:

$$\chi(k) = \sum_j S_0^2(k) \frac{N_j}{kr_j^2} e^{-2\sigma_j^2 k^2} e^{-2\frac{r_j}{\lambda_j(k)}} A_j(k) \sin [2kr_j + \phi_j(k)] \quad (2)$$

with

$$k = \sqrt{\frac{2m}{\hbar^2}(E - E_0)} \quad (3)$$

k = photoelectron wavevector modulus; j = coordination shell index; r = distance between the absorbing atom and a neighbor; N = number of (identical) atoms in the same coordination shell; $A(k)$ = backscattering amplitude; σ = total Debye-Waller factor; $\phi(k)$ = total phase shift; $\lambda(k)$ = photoelectron mean free path; $S_0^2(k)$ = amplitude reduction factor due to many-body effects; E = photon energy; m = electron mass; E_0 = threshold energy and $e^{-2\frac{r}{\lambda(k)}}$ determines the finite photoelectron lifetime.

To estimate the structural parameters, i.e., the coordination number (N), the interatomic distance (r) and the Debye-Waller factor (σ), the atomic parameters: $\lambda(k)$, $A(k)$, $\phi(k)$ and $S_0^2(k)$ must be known from a theoretical calculation or an experimental determination by using a standard reference. By applying a Fourier transformation, the structural parameters can be determined separately for each coordination shell.

The EXAFS experiments in this work were performed at the INE beamline at the ANKA 2.5 GeV synchrotron radiation facility. For details about the instrumentation at this beamline see [62]. For energy monochromatization, a Lemonnier-type [63] double-crystal monochromator equipped with Ge(422) crystal was employed, leading to a minimum energy step width of 0.2 eV. For calibration a photon energy of 20 keV was assigned to the first inflection point of the K-edge spectrum of a molybdenum foil.

3.1.2 Gas adsorption

Adsorption processes are classified as physical and chemical adsorption according to the types of interaction between the adsorbate and the absorbent [64]. Physical adsorption is a result of relatively weak interaction of the van der Waals type. Therefore, the physically adsorbed gas molecules on the solid can be almost removed by evacuation. Chemical adsorption (chemisorption) occurs due to specific chemical interactions, thus chemisorption

can be applied to determine the number of active sites on a surface. Gas physisorption is commonly used for the determination of surface area and pore size distribution of a solid from the adsorption isotherm (the graph of amount of adsorbed molecules (V) against the adsorption pressure (p) at constant temperature) whose shape is not only related to the specific surface area but also to the pore structure. According to the isotherm shapes, the majority of isotherms may be grouped in six types of isotherms distinguished in the Fig. 8.

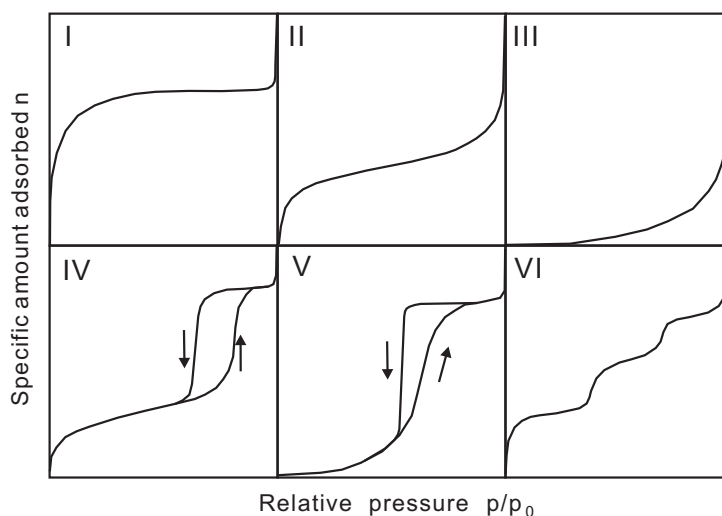


Fig. 8: The IUPAC classification for adsorption isotherms

Type I isotherm characterizes microporous adsorbents. Types II and III describe adsorption on macroporous adsorbents with strong and weak adsorbate-adsorbent interactions, respectively. The characteristic feature of Type IV and V adsorption isotherms is the hysteresis loop. Type IV and V isotherms are observed for many mesoporous adsorbents. Similar to the Type III isotherm, the Type V isotherm results from a weak adsorbate-adsorbent interaction. The Type VI isotherm represents a stepwise multilayer adsorption on a uniform non-porous substrate.

i) Surface area determination

ia) Langmuir isotherm

The Langmuir model is a theory restricted to monolayer molecular adsorption with the

following hypotheses [65]: 1) adsorption is localized (lattice model) and 2) the adsorption energy ΔH_{ads} is independent of the surface coverage. The Langmuir equation is usually given as follows:

$$\frac{p}{V} = \frac{1}{bn_m} + \frac{p}{n_m} \quad (4)$$

where:

p = pressure;

V = volume of gas adsorbed at pressure p ;

n_m = volume of adsorbate at full monolayer coverage;

b = a constant dependent on temperature. A plot of p/V against p yields the monolayer volume n_m which can be used for the calculation of the surface area:

$$S_w = \frac{N\sigma n_m}{M_v} \quad (5)$$

with S_w being the mass specific surface area, N is the Avogadro constant 6.023×10^{23} molecules mol^{-1} and σ is the area occupied by one adsorbate molecule.

ib) BET isotherm

Based on the Langmuir equation, the BET equation has been developed by Brunauer, Emmett and Teller [66] for the surface area determination for multilayer molecular adsorption based on the following assumption: (1) the surface is energetically homogeneous; (2) gas molecules physically adsorb on a solid in layers infinitely; (3) horizontal interactions are neglected; and (4) the Langmuir theory can be applied to each layer. The commonly known BET equation is expressed as

$$\frac{1}{V[(p/p_0) - 1]} = \frac{1}{cn_m} + \frac{c-1}{cn_m} \frac{p}{p_0} \quad (6)$$

where p_0 is the saturation pressure of adsorbates and c is named as BET constant which is approximately determined by:

$$c = \exp\left(\frac{Q_1 - Q_L}{RT}\right) \quad (7)$$

with Q_1 and Q_L being the heat of adsorption of the first layer and the heat of liquefaction of the bulk liquid, respectively. A plot of $\frac{1}{V[(p/p_0) - 1]}$ against p/p_0 (BET plot) yields a

straight line with a slope $\frac{c-1}{cn_m}$ and intercept $\frac{1}{cn_m}$. The linear relationship of this equation has been found to hold in the range of $0.05 < p/p_0 < 0.35$.

ii) Pore size distribution

iii) The hysteresis loop

According to the IUPAC classification four types of hysteresis loops have been considered as shown in Fig. 9. Type H₁ is associated with agglomerates or compacts of uniform spheres in a fairly regular array and hence to a narrow distribution of pore sizes. Type H₂ occurs for a none uniform pore distribution and the role of networks must be taken into account. Type H₃ is observed with aggregates of plate-like particles giving rise to slit-shaped pores. Type H₄ describes the presence of micro-pores as well as slit-shaped pores.

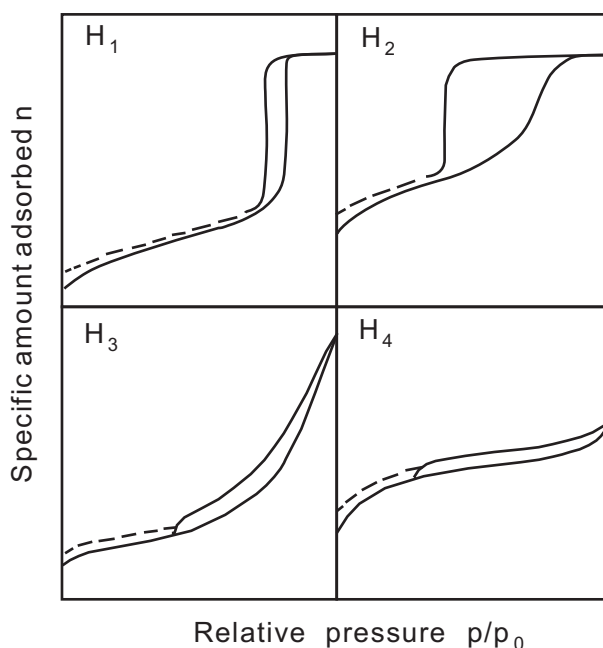


Fig. 9: Types of hysteresis loops (IUPAC)

iib) the Kelvin equation

The Kelvin equation relates the equilibrium vapor pressure p of a liquid to the curvature of the liquid-vapor interface:

$$\ln \frac{p}{p_0} = \frac{-2\gamma V_m \cos \theta}{RT r_K} \quad (8)$$

where:

p - actual vapor pressure;

p_0 - saturated vapor pressure;

γ - surface tension;

V_m - molar volume;

R - universal gas constant;

r_K - the Kelvin radius;

θ - wetting angle which is taken as zero;

T - temperature.

iic) BJH model

The BJH method has been described by Barret, Joyner and Halenda [67] for adsorbents with cylindrical pores based on the premise that the thickness of the residual layer is the same in the pores as it would be on a plane surface. Two parts of the gas adsorption have been considered: 1) the volume of condensate in all pores is smaller than some characteristic size which depends on current relative pressure $r_c(x_k)$, 2) a volume of an adsorbed film on all larger pores (equation 9 and Fig. 10):

$$V_{ads}(x_k) = \sum_{i=1}^k \Delta V_i(r_i \leq r_c(x_k)) + \sum_{i=k+1}^n \Delta S_i t_i(r_i > r_c(x_k)) \quad (9)$$

here $V_{ads}(x_k)$ is the volume of adsorbate at the relative pressure of $x_k = \frac{p_k}{p_0}$, V is the pore volume, S is surface area and t is the thickness of the adsorbed layer. $r_c(x_k)$ is given by the Kelvin equation (10):

$$r_c(x_k) = -\frac{\gamma V_m \cos(\theta)}{RT} \left(\frac{1}{\ln x_0} - \frac{1}{\ln x_k} \right) \quad (10)$$

where $x_0 = 1$ and for pore radius r_i (11):

$$r_i = r_c(x_i) + t \quad (11)$$

Therefore, it is necessary to determine the thickness t for the evaluation of the pore size distribution. The thickness has been found to be associated with the volume of the adsorbed molecules (12):

$$t = y \frac{V}{n_m} \quad (12)$$

where y is the thickness of one layer.

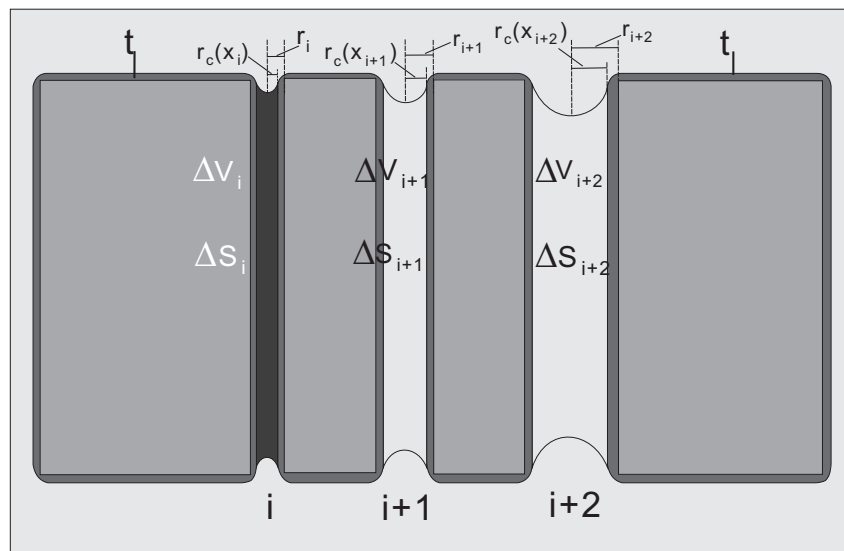


Fig. 10: The cylindrical pore model

3.1.3 Transmission electron microscopy (TEM)

As shown in Fig. 11, a modern TEM is composed of an illumination system, a specimen stage, an objective lens system, the magnification system, the data recording system and the chemical analysis system. Electrons in illumination system are generated by a thermionic discharge (typically LaB_6 thermionic emission) or by field emission. The heart of a TEM is the objective lens system, which determines the limit of image resolution. A magnification up to 1.5 million can be obtained in the magnification system which is composed of an intermediate lens and a projection lens. The data recording system

equipped with a charge coupled device (CCD) gives the possibility for the data processing and quantification. Finally, the chemical composition and electronic structure of the specimen can be probed in a chemical analysis system by using the energy dispersive X-ray spectroscopy (EDS) and/or electron energy-loss spectroscopy (EELS).

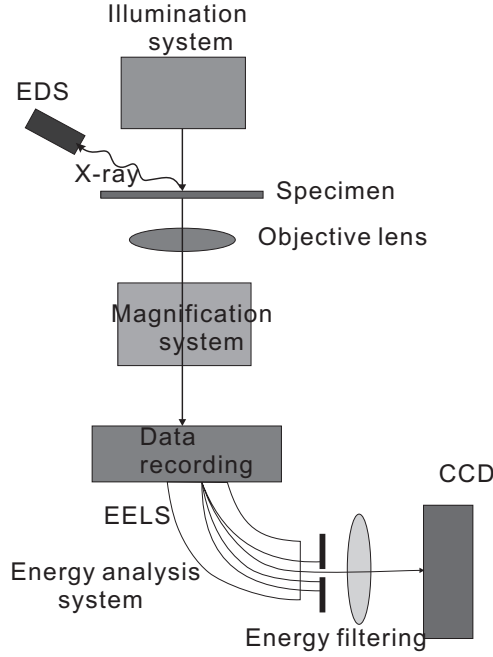


Fig. 11: Schematic drawing of a transmission electron microscope from [61].

The image formation process is displayed in Fig. 12. If a high-energy electron beam hits a thin specimen, the waves scattered under different angles θ are brought together at a point on the back-focal plane yielding a diffraction pattern. The diffraction amplitude at the back-focal plane can be determined by

$$\Psi'(u) = \Psi(u)e^{i\chi(u)} \quad (13)$$

where $\Psi(u)$ is the Fourier transformation of the wave $\Psi(r)$ and the reciprocal vector $u = 2 \sin \theta / \lambda$ with λ being the wave length of the electrons. $\chi(u)$ can be described by

$$\chi(u) = \frac{\pi}{2} C_s \lambda^3 u^4 - \pi \Delta f \lambda u^2 \quad (14)$$

where C_s is the spherical abberation coefficient, Δf is the lens defocus. The electron image is calculated according to

$$I(x, y) = |\Psi(r) \otimes t_{obj}(x, y)|^2 \quad (15)$$

where $t_{obj}(x, y)$ is the inverse Fourier transformation of the phase function $e^{i\chi(u)}$, and \otimes is a convolution calculation of (x, y) . A TEM can be modified to a scanning transmission electron microscope (STEM) by the addition of a system that scans the beam across the sample to form the image, combined with suitable detectors. Two types of contrast are generally present in a TEM: the diffraction contrast produced by crystal orientation and specimen thickness and the phase contrast which is sensitive to the types of atoms and atom distribution in the specimen.

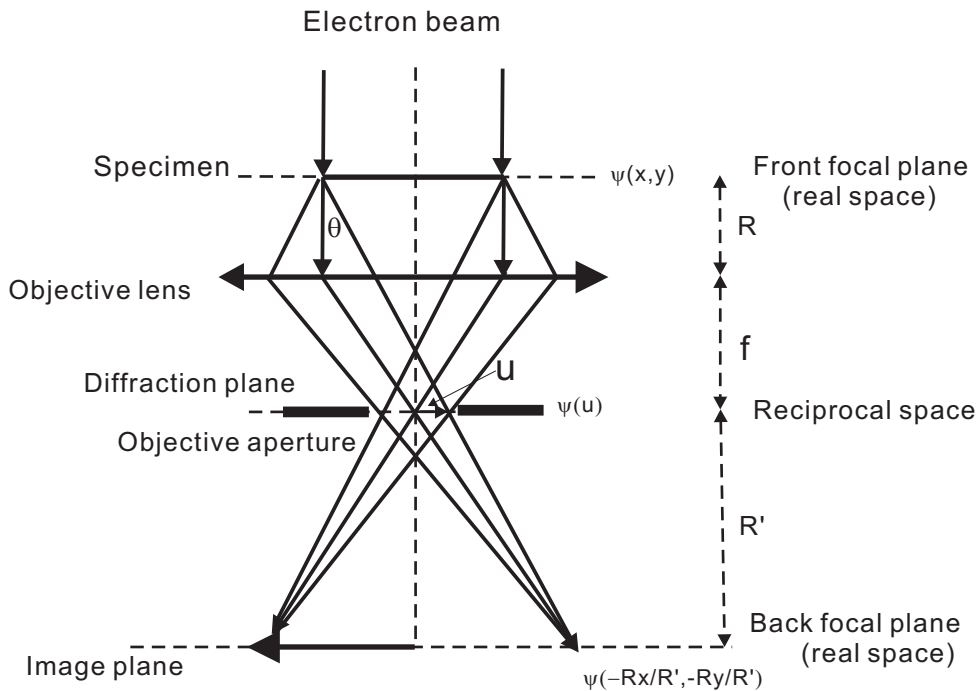


Fig. 12: Abbe's theory of image formation in a one-lens transmission electron microscope from reference [61]

In the present work, high-resolution transmission electron microscopy (HRTEM) and selected area electron diffraction (SAED) were performed with a Philips CM30ST microscope (300 kV, LaB₆ cathode, CS = 1.15 mm, Max-Planck-Insitut für Festkörperforschung, Stuttgart, PD Dr. L. Kienle). A perforated carbon/copper net served as support of the particles of supported catalysts. SAED patterns were obtained using a diaphragm which limited the diffraction to a circular selected area (diameter: 250 nm). All images were recorded with a Gatan Multiscan CCD camera and evaluated (including Fourier analyses) with the program Digital Micrograph 3.6.1 (Gatan). EDX analyses were performed in the

nanoprobe mode of CM30ST with a Si/Li detector (Noran, Vantage System).

3.1.4 High-angle annular darkfield (HAADF) technique

HAADF images were obtained in a VG HB501UX dedicated scanning transmission electron microscope. In this imaging mode the brightness is proportional to Z^n , where Z denotes the atomic number and $n \approx 1.7$. The combined energy-dispersive X-ray analysis (EDXS) with a spatial resolution of about 1 nm was performed for the determination of the metal content.

3.1.5 Chemical elemental analysis

Chemical elemental analyses were performed on a EURO Vector EURO EA combustion analyzer; using zinc sample holders with 2 - 3 mg per sample, heated up to 1273 K under oxygen atmosphere and the gases were then detected by a thermal conductivity system using helium 5.0.

3.1.6 FT-Raman spectroscopy

Fourier transform (FT) Raman spectra were recorded with a Bruker FT-106 Raman module, equipped with a Ge detector cooled by liquid nitrogen and connected to a Bruker FT-IR 66 interferometer and a continuous wave diode-pumped Nd:YAG Laser with a radiation wavelength of 1064 nm (9398.5 cm^{-1}). The laser power was set to 300 mW and the spectral resolution was 2 cm^{-1} .

3.1.7 X-ray powder diffraction (XRD)

X-ray powder diffraction experiments were performed with a Siemens D5000 diffractometer at room temperature using Cu K_α radiation. The collected data were processed with the STOE WinXpow software.

3.2 Catalytic activity test of HDS of DBT

The catalytic activity tests were carried out in a Parr model 4522 high-pressure batch reactor in the Centre of Advanced Materials Research, CIMAV, in Chihuahua, Mexico.

Ca. 1 g of the catalyst and 75 mL of a freshly prepared solution of DBT in decaline (5% wt./wt., $[\text{DBT}]_0 = 0.1195 \text{ mol/L}$) were placed in the reactor. The reactor was then purged and pressurized with H_2 to 3.37 MPa and heated up to 623 K at 10 K/min heating rate, see Fig. 13. The stirring of the reaction mixture was sufficiently intensive to exclude external diffusion limitations (checked by varying amounts of the catalyst and the power of stirring (1000, 800 and 700 rpm). When the working temperature was reached, the evolved gaseous samples were collected for chromatographic analysis every half an hour to determine conversion-time dependence during 5 h. A Perkin Elmer gas chromatograph model Auto-System XL with a 9 ft long, 1/8 inch packed column containing OV-3 (phenylmethyl-dimethyl silicone, 10% phenyl) as separating phase was applied to analyze the gases collected in the batch after the reaction. Estimated errors in the activity measurements are 2%.

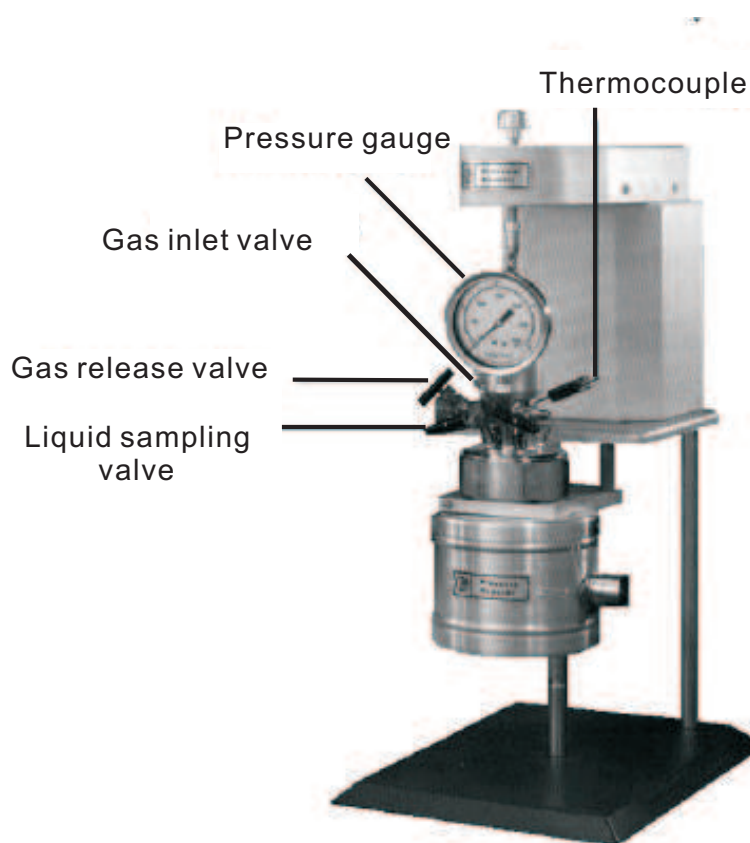


Fig. 13: High-pressure batch reactor for the HDS of DBT

Table 1: Purity of used chemicals

Chemical	Marker	Purity
Ammonia 20 % (in H ₂ O)	Merck	Technical grade
Ammonium heptamolybdate tetrahydrate	Merck	p.a.
Dibenzothiophene	Aldrich	98%
Decahydronaphthalene (Decaline, cis + trans)	Aldrich	98%
Ethanol	Roth	≥ 99.8%
Hydrogen sulfide	Messer-Grieheim	99.99%
Tetramethylammonium bromide	Fluka	≥ 97%
Forming gas (H ₂ 10% N ₂ 90%)	Linde Gas	Technical grade
Sodium dimethyldithiocarbamate hydrate	Aldrich	98%
Sodium diethyldithiocarbamate trihydrate	Aldrich	Technical grade
Nickel(II)perchlorate hexahydrate	Aldrich	Technical grade
Tungstic acid	ABCR	99%
Poly(ethylene glycol)- <i>block</i>		
-poly(propylene glycol)- <i>block</i>	Aldrich	Technical grade
-poly(ethylene glycol)		
Aluminum oxide, activated, neutral	Aldrich	Technical grade
Tetraethyl-orthosilicate	Fluka	≥ 99%
Phosphorus pentoxide	Riedel–de Haeen	≥ 98.5%
Trichloromethane	Fluka	≥ 99.8%
Cobalt(II)acetate tetrahydrate	ABCR	98%
Nickel(II)acetate tetrahydrate	ABCR	98%

4 Results and Discussion

4.1 SBA-15 as support for Mo and W sulfide based HDS catalysts

SBA-15 supported molybdenum and tungsten sulfide based HDS catalysts derived from (alkyl)ammonium thiomolybdate and ammonium thiotungstate as sources have been investigated by various characterization methods like XRD, N_2 physisorption and HRTEM. The HDS activity study was carried out at $T = 623$ K and $P_{H_2} = 3.4$ Mpa in a Parr Model 4520 high-pressure batch reactor using dibenzothiophene (DBT) as model molecule. Both cobalt or nickel acetate and cobalt or nickel thiocarbamate have been employed as the precursor of the promoter atoms.

4.1.1 Characterization and HDS activity investigation of MoS_2 /SBA-15 and (Ni)CoMo/SBA-15 using cobalt or nickel acetate as precursor

i) *NiMo/SBA-15 catalysts*

NiMo/SBA-15 catalysts were prepared by impregnation of SBA-15 (6 and 9 nm) with nickel acetate followed by calcination at 773 K for 3 h as the first step. The obtained NiO/SBA-15 was then stirred in aqueous solutions of ammonium thiomolybdate $(NH_4)_2MoS_4$ (ATM) with appropriate concentrations. After 20 h stirring at room temperature the products were filtered without washing and the catalyst activation was carried out at 773 K for 3 h in a H_2/N_2 ($H_2 = 10\%$) flow. The low angle XRD pattern (Fig. 14) and the N_2 adsorption isotherms (Fig. 15) show the typical features of the pristine SBA-15 support which gives evidences for the preservation of the structure of SBA-15. The BET and the normalized surface areas are summarized in Table 2. Compared to the catalysts supported on 6 nm SBA-15, Ni(1.5)Mo(16)/SBA(9 nm) reveals a higher normalized surface area (0.91, Table 2) suggesting that a lower pore blocking can be obtained applying 9 nm support material.

The NiMo/SBA-15 catalysts exhibit a HDS activity with a slight preference for the DDS pathway ($HYD/DDS \approx 0.80$, Table 2), indicating the presence of the catalytic active NiMoS phase. The catalytic activity of all NiMo/SBA-15 catalysts is considerably lower

than that of the commercial NiMo/ γ -Al₂O₃ catalyst (1.2×10^{-6} mol s⁻¹ g⁻¹). Furthermore, no dependence of the HDS activity upon the Mo concentration and the SBA-15 pore sizes could be detected. One possible explanation is that the generated stable NiO phase is difficult to be sulfided and consequently a few catalytic active NiMoS particle are generated under the actual experimental conditions.

Table 2: Surface areas, normalized surface areas, initial rate constants (k) and selectivity HYD/DDS of the NiMo/SBA-15 catalysts during the HDS reaction of DBT.

Catalysts	Mo wt. %	Ni wt. %	surface area m ² g ⁻¹	surface area normalized	rate constants $\times 10^{-7}$ mol s ⁻¹ g ⁻¹	HYD/DDS
SBA-15(6 nm)	-	-	842	1	-	-
Ni(1.5)Mo(7)/SBA(6 nm)	7.1	1.5	486	0.60	4.4	0.93
Ni(1.5)Mo(16)/SBA(6 nm)	16.4	1.5	370	0.59	3.0	0.76
SBA-15(9 nm)	-	-	467	1	-	-
Ni(1.5)Mo(16)/SBA(9 nm)	16.1	1.5	289	0.91	4.3	0.84

ii) *Mo/SBA-15 and CoMo/SBA-15 catalysts*

Analogously to the preparation of NiMo/SBA-15 catalysts, CoMo/SBA-15 was prepared by impregnation of SBA-15 (6 and 9 nm) with cobalt acetate in the first step. However, during calcination in air no cobalt oxides were formed but a blue cobalt silicate was generated. In a H₂S atmosphere the Co/SBA-15 material reacted easily to form CoS_x/SBA-15 which was then impregnated with ATM. The activation of the catalysts was carried out at 773 K for 3 h under H₂/N₂ (H₂ = 10%) gas stream prior to the catalytic test.

XRD and TEM investigations confirm that MoS₂ and Co-MoS₂ were incorporated into the pore channels of the SBA-15 support without destroying the mesoporous structure. For MoS₂/SBA-15 catalysts the pore size enhancement of the SBA-15 support from 6 to 9 nm results interestingly in an increase of HDS activity with a higher hydrogenation reactivity. This finding can be regarded as a confinement effect because hydrogenation of DBT occurs through a flat π adsorption via the aromatic systems which is the sterical demanding pathway of the reaction [68]. For Co promoted catalysts the confinement effect is less pronounced and the selectivity change observed for CoMo/SBA-15 catalysts

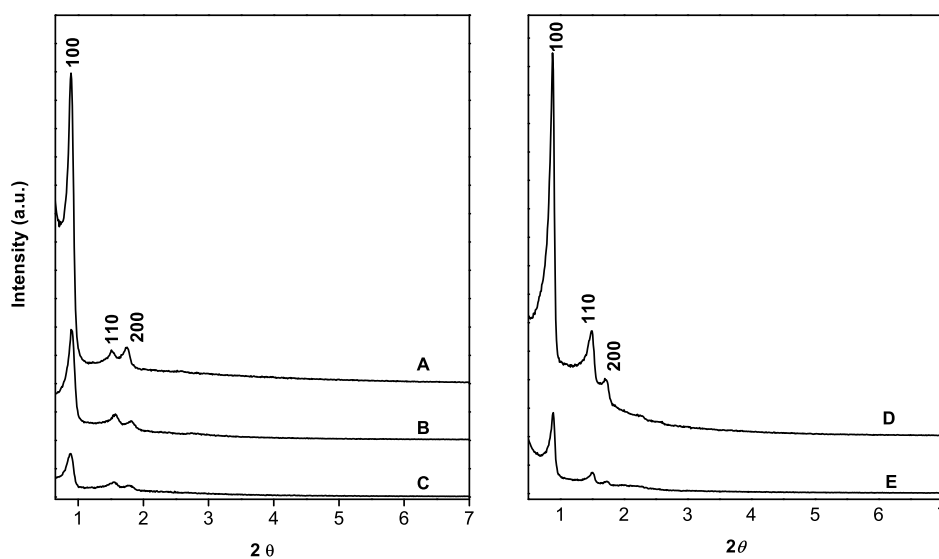


Fig. 14: Low angle XRD patterns of (A) parent SBA-15 (6 nm), (B) Ni(1.5)Mo(7)/SBA(6 nm), (C) Ni(1.5)Mo(16)/SBA(6 nm), (D) parent SBA-15 (9 nm) and (E) Ni(1.5)Mo(16)/SBA(9 nm).

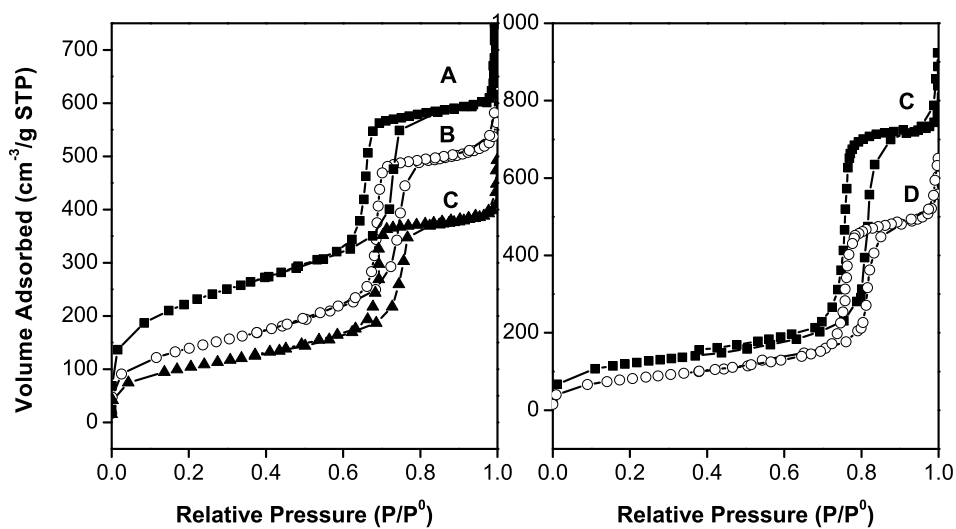


Fig. 15: Nitrogen adsorption/desorption isotherms of (A) parent SBA-15 (6 nm), (B) Ni(1.5)Mo(7)/SBA(6 nm), (C) Ni(1.5)Mo(16)/SBA(6 nm), (C) parent SBA-15 (9 nm) and (D) Ni(1.5)Mo(16)/SBA(9 nm).

is most likely due to the so-called synergistic effect of the promoter. The addition of Co yields a strong improved HDS performance compared to the pure MoS₂ catalyst which is due to the enhanced direct desulfurization (DDS) activity. Despite the presence of pronounced MoS₂ stacking, most of the CoMo/SBA-15 catalysts show interestingly higher HDS activity compared to a commercial CoMo/ γ -Al₂O₃. MoS₂ stacking is therefore not prerequisite for a high HDS performance. The presence of the CoMoS phase and the creation of a large number of coordinatively unsaturated sites (CUS) can be regarded as the main cause for the high HDS activity with a strong preference for the DDS pathway.

Catal Lett (2008) 122:57–67
DOI 10.1007/s10562-007-9351-y

SBA-15 as Support for MoS₂ and Co-MoS₂ Catalysts Derived from Thiomolybdate Complexes in the Reaction of HDS of DBT

Z.-D. Huang · W. Bensch · L. Kienle ·
S. Fuentes · G. Alonso · C. Ornelas

Received: 11 September 2007 / Accepted: 8 November 2007 / Published online: 27 November 2007
© Springer Science+Business Media, LLC 2007

Abstract Molybdenum sulfide and cobalt-molybdenum sulfide catalysts supported on mesoporous SBA-15 were prepared by thermal decomposition of ammonium thiomolybdate (ATM). SBA-15 was synthesized at 353 K and 413 K to obtain pore diameters of about 6 and 9 nm, respectively. The (Co)-MoS₂/SBA-15 catalysts were characterized with X-ray diffraction (XRD), N₂-physisorption and high-resolution transmission electron microscopy (HRTEM). HRTEM images give evidence for the presence of a poorly dispersed MoS₂ phase with long MoS₂ slabs and a pronounced MoS₂ stacking. The catalytic performance in the hydrodesulfurization (HDS) reaction of dibenzothiophene (DBT) was examined at $T = 623$ K and $P = 3.4$ MPa. The Co-MoS₂/SBA-15 materials show a relatively high catalytic activity with a strong preference for the direct desulfurization (DDS) pathway. This is an interesting result in view of the significant stacking of MoS₂ particles and the size of the slabs. The generation of the catalytically active CoMoS phase and a large number of coordinately unsaturated sites (CUS) may explain the high performance of Co promoted MoS₂/SBA-15 catalysts in the HDS reaction.

Z.-D. Huang · W. Bensch (✉)
Institut für Anorganische Chemie, University of Kiel,
Olshausenstraße 40-60, 24098 Kiel, Germany
e-mail: wbensch@ac.uni-kiel.de

L. Kienle
Max-Planck-Institut für Festkörperforschung, Heisenbergstr. 1,
70506 Stuttgart, Germany

S. Fuentes
Centro de Ciencias de la Materia Condensada, UNAM,
Ensenada, Baja California C.P. 22860, Mexico

G. Alonso · C. Ornelas
Centro de Investigación en Materiales Avanzados S. C.,
Chihuahua, Chih. C.P. 31109, Mexico

A confinement effect of the mesoporous channels of SBA-15 is observed for the unpromoted MoS₂/SBA-15 catalysts. SBA-15 with 9 nm channel diameter with 11 wt.% Mo loading shows a higher selectivity for the hydrogenation pathway than SBA-15 with 6 nm channel and 16 wt.% Mo loading.

Keywords Hydrodesulfurization · Ammonium thiomolybdate · Co-MoS₂/SBA-15 catalysts · HRTEM · Coordinately unsaturated sites (CUS) · SBA-15 support

1 Introduction

More stringent limitations to sulfur contents of transportation fuels lead to continuing quest for better performing hydrodesulfurization (HDS) catalysts. One of the successful ways to improve the catalyst activity is to synthesize transition metal sulfides on a porous support material which can well control the structure of the catalyst. Most commercially available HDS catalysts are supported on alumina with a surface area of about 200 m²/g. Mesoporous silica materials such as MCM-41 [1, 2] and SBA-15 [3] with their well ordered hexagonal pore structures, narrow pore diameters (3–30 nm) and higher surface areas (more than 700 m²/g) offer several advantages in comparison with alumina. MCM-41 supported Co(Ni)Mo catalysts were investigated in the last decade [4–7]. The catalysts exhibited higher activities for conversion of dibenzothiophene (DBT) and petroleum residues than Co(Ni)-Mo/ γ -Al₂O₃ at high molybdenum loading [4] or high atomic ratio Co(Ni)-Mo [5, 6]. More recently, mesoporous SBA-15 has been in the focus of research interests due to the larger pores, thicker pore walls and higher hydrothermal stability compared to MCM-41. Indeed, Vradman et al. [8, 9]

demonstrated the excellent potential of high loading Ni-W/SBA-15 catalysts for deep hydrotreatment of petroleum feedstocks. The catalysts prepared by an ultrasonication route showed a high HDS activity. Mesoporous SBA-15 was also found to be a suitable support for Mo, CoMo, and NiMo catalysts as reported by Rao and co-workers [10]. Furthermore, Al, Ti and Zr containing SBA-15 supported NiMo or CoMo catalysts were prepared by Klimova and co-workers [11, 12], Rao and co-workers [13] and Fierro and co-workers [14]. They observed that SBA-15 modified with these hetero-atoms (Al, Ti, Zr) provides better dispersion for the deposited Ni(Co) and Mo active species and yields considerably high activity for HDS of DBT.

In the majority cases these hydrotreating catalysts were prepared via an oxide route, i.e. the MCM-41 or SBA-15 materials containing transition metal salts like ammonium heptamolybdate, nickel (cobalt) nitrate or nickel (cobalt) acetate were calcined to produce stable oxides. The oxides must then be sulfided either prior to or during the start-up of the hydrotreatment process in a stream of H₂S (15%) in H₂. Catalysts processed with such a procedure exhibit HDS activity being strongly influenced by the calcination temperature, the temperature and pressure for transformation to the sulfide [15]. On the other hand, molybdenum and tungsten sulfide catalysts for hydrotreating reactions can be obtained directly by decomposition of the corresponding thiometalates. It was observed that the thermal decomposition of molybdenum and tungsten thiosalts is an effective method for the production of improved unsupported catalysts. One reason is that no metal-sulfur bond formation is required which is necessary applying the oxide route [16–19]. However, to the best of our knowledge only a few studies have been performed to investigate supported MoS₂ catalysts derived from ammonium thiomolybdate (ATM) as precursor [20, 21].

The aim of this work was to study the SBA-15 support with different pore sizes (6 nm and 9 nm) for MoS₂ and MoS₂ promoted with Co catalysts using ATM as molybdenum source in the HDS of DBT reaction. The supported catalysts were characterized with X-ray diffractometry (XRD), nitrogen physisorption using the Brunauer, Emmett and Teller (BET) method and high-resolution transmission electron microscopy (HRTEM).

2 Experimental

2.1 Sample Preparation

2.1.1 Synthesis of Pristine Mesoporous SBA-15 [22–24]

Eight gram of poly(ethyleneglycol)-block-poly(propyleneglycol)-block-poly(ethyleneglycol) triblock copolymer

(Aldrich, pluronic, P-123) was dissolved in 240 g of water and 28.6 g of concentrated hydrochloric acid at 303 K on a water bath. After drop wise addition of 16 g of tetraethyl-orthosilicate (TEOS), the reaction mixture was stirred for 24 h at 303 K. The resulting gel was transferred into a Teflon bottle and heated to 353 K and 413 K for 24 h to obtain SBA-15 with 6 nm and 9 nm pores, respectively. The resulting white powder was filtered and washed with deionized water, and the surfactant was removed by Soxhlet extraction at 351 K with a mixture of 970 mL of ethanol and 30 mL of concentrated hydrochloric acid. After washing with ethanol, the white powder was dried at room temperature under vacuum for about one week.

2.1.2 Synthesis of MoS₂/SBA-15

Typically, 2 g of SBA-15 was stirred in aqueous solutions of ammonium thiomolybdate (NH₄)₂MoS₄ (ATM) with different concentrations. After stirring at room temperature for 20 h the products were filtered without washing. Materials containing different Mo concentrations were prepared using appropriate concentrations of ATM and the final products were stored in dry air. The synthesized samples are denoted as Mo(X)/SBA-15(Y) in the figure legends, where X is the Mo loading in wt.% and Y is the pore size of SBA-15.

2.1.3 Synthesis of Co-MoS₂/SBA-15

Supported Co-Mo catalysts were prepared by impregnation of SBA-15 with Co(CH₃COO)₂·4H₂O followed by evaporation of H₂O and CH₃COOH at 773 K for 3 h. At this temperature the pink (CH₃COO)₂Co·4H₂O/SBA-15 material turned blue indicating the formation of Co silicates. Under H₂S atmosphere the blue Co/SBA-15 reacted easily to form CoS_x/SBA-15. It was stirred in aqueous solutions of ATM and then treated with the same procedure used for the synthesis of MoS₂/SBA-15 to prepare Co-Mo/SBA-15. The samples are named as Co(X)Mo(Y)/SBA-15(Z) in the figure legends, where X is the Co loading in wt.%, Y is the Mo loading in wt.%, and Z is the pore size of SBA-15.

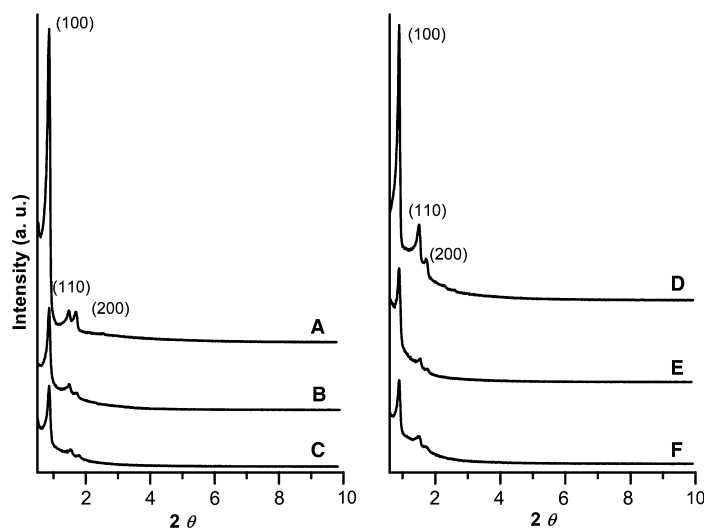
2.2 Sample Characterization

X-ray diffraction (XRD) patterns were obtained on a Bruker D8 Advance diffractometer at room temperature using CuK_{α1} radiation. Nitrogen adsorption measurements were carried out at 77 K on a Sorptomatic 1990 adsorption analyzer. Before the measurements, the samples were out gassed for at least 24 h at 393 K. The BET surface areas

were calculated from $p/p_0 = 0.03\text{--}0.3$ in the adsorption branch.

A prominent classical method used for the analysis of the pore size distributions (PSD) from sorption isotherms is the Barrett-Joyner-Halenda (BJH) approach, which is based on macroscopic thermodynamic models such as the modified Kelvin equation for cylindrical pores [25]. The evaluation of the PSD of mesoporous materials applying the BJH method is widely used in literature (see for example references [8, 10–12, 14, 22, 23]). Compared to other methods like the non-local density functional theory (NLDFT) the BJH analysis slightly underestimates the pore size of mesoporous materials [26, 27]. Nevertheless, the BJH method yields reasonable values for the PSD and changes of the pore size due to the presence of guest species in the channels are undoubtedly detected. In the present work the BJH method was applied for the calculation of the PSD using the desorption branch of the adsorption isotherms. HRTEM and SAED were performed with a Philips CM 30ST microscope (300 kV, LaB₆ cathode, $C_s = 1.15$ mm). A perforated carbon/copper net served as support for the particles of Co-Mo/SBA-15 (9 nm). SAED patterns were obtained using a diaphragm which limited the diffraction to a circular selected area (diameter: 250 nm). All images were recorded with a Gatan Multiscan CCD camera and evaluated (including Fourier analyses) with the program Digital Micrograph 3.6.1 (Gatan). EDX analyses were performed in the nanoprobe mode of CM30ST with a Si/Li detector (Noran, Vantage System). The Mo and Co contents of the different materials were determined by means of Inductively Coupled Plasma (ICP) analyses.

Fig. 1 XRD patterns of (A) SBA-15 (6 nm), (B) Mo(9)/SBA-15 (6 nm), (C) Co(2)Mo(10)/SBA-15 (6 nm), (D) SBA-15 (9 nm), (E) Mo(11)/SBA-15 (9 nm) and (F) Co(2)Mo(10)SBA-15 (9 nm)



Prior to the catalytic test, the catalysts were activated at 500 K for 3 h under a H₂/N₂ (H₂, 10%) gas flow at atmospheric pressure. HDS of DBT was carried out in a Parr model 4522 high-pressure batch reactor. One gram of the catalyst and 150 mL of the freshly prepared solution of DBT in decaline (5% w/w [DBT]₀ = 0.2388 mol/L) was introduced in the reactor. The reactor was then purged and pressurized to 3.4 MPa (490 psi) with hydrogen and then heated up to 623 K at a rate change for with slope of 10 K/min and continuous stirring of 600 rpm. After reaching the working temperature, the products were collected for chromatographic analysis every half an hour to determine the conversion-time dependence during 5 h. After the reaction, the used catalysts were filtered, washed and stored in inert atmosphere. The reaction products were analyzed using a Perkin-Elmer Auto-system chromatograph with a 9 ft long × 1/8 inch diameter packed column containing chromosorb W-AW 80/100 mesh 3% OV-17 (phenyl methyl silicone 50% phenyl) as a separating phase. Estimated errors in the activity measurements are ±2%.

3 Results and Discussion

3.1 Powder XRD

In Fig. 1 the XRD patterns of MoS₂/SBA-15 and MoS₂/SBA-15 promoted with Co (6 nm and 9 nm) are displayed. An intense peak at about 1.0° 2θ and two distinct weak reflections between 1.5 and 2.0° 2θ are observed which are the characteristic reflections (100), (110), and (200) of

hexagonal mesoporous SBA-15 with space group $p6mm$. The existence of these characteristic peaks evidences that the primary structure of the material consists of well ordered channels which are maintained after the Co and Mo incorporation. However, after loading of SBA-15 with $\text{MoS}_2/\text{Co-MoS}_2$ the intensity of the reflections decreased. This phenomenon is well known and is caused by the strong absorption of X-rays by Mo and/or a partial loss of the high order of the mesostructure [11].

Wide-angle XRD patterns of Co-Mo catalysts supported on SBA-15 with pore size of 6 nm are shown in Fig. 2. In addition to a broad modulation at about $22^\circ 2\theta$ caused by SBA-15, reflections at 14.4 , 33 , 40 , and $58^\circ 2\theta$ correspond to the poorly crystalline structure of 2H-MoS_2 in all patterns. The asymmetric shape of the reflections at 33 , 40 , and $58^\circ 2\theta$ is a typical feature of layered materials with a partial turbostratic disorder. The average particle size of MoS_2 can be estimated from the peak width using the Scherrer formula, $d = 0.941\lambda/B \cos\theta_B$, where d is the mean diameter of the particle, λ is the wavelength of the Cu $K_{\alpha 1}$ line (0.154056 nm), θ_B is the angle between the incident beam and the reflecting lattice planes, and B is the width of the diffraction peak. The average crystallite size of MoS_2 estimated from the (002) reflection is typically about 4 nm (see Table 1), i.e., on average six layers of MoS_2 form the stacks in the c direction. The mean crystallite size of MoS_2 increases with increasing Mo loading for catalysts with the same Co content (Table 1). Comparing the sizes of MoS_2 nanoparticles with the pore diameters of the SBA-15 materials, a possible explanation is that the crystallites are located inside the channels of SBA-15 being directed along the channel axis. With increasing Co content up to ca. 3 wt.% an enlargement of the particle size of MoS_2 to about 6 nm is

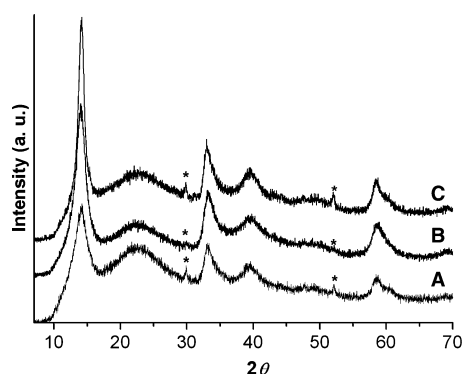


Fig. 2 Wide-angle XRD patterns of (A) Co(2)Mo(10)/SBA-15 (6 nm), (B) Co(2)Mo(20)/SBA-15 (6 nm); (C) Co(3)Mo(14)/SBA-15 (6 nm). (*) Co_9S_8

observed (Table 1, Fig. 2C). It suggests that the CoS_x particles inside the channels hinder the dispersion of ATM along the channels. In addition to the reflections of MoS_2 , reflections of the stable Co_9S_8 phase appear at 30 and $52^\circ 2\theta$. The peaks of Co_9S_8 are almost absent for high Mo-loading (Fig. 2B), which indicates the generation of an increasing amount of the catalytically active CoMoS phases.

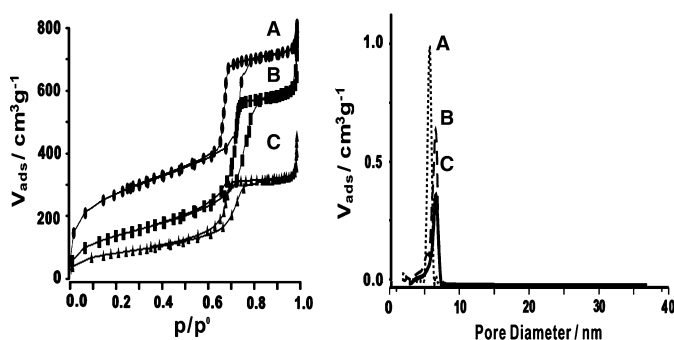
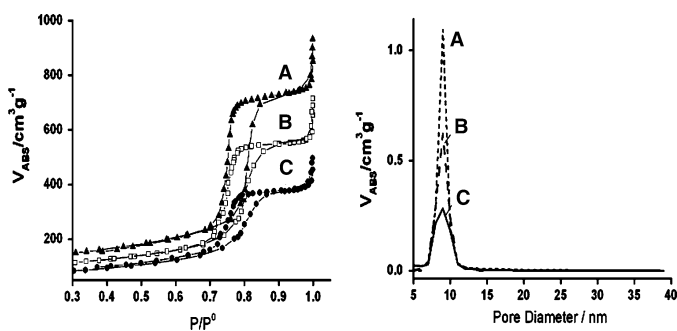
3.2 Nitrogen Physisorption

In Figs. 3 and 4 the N_2 adsorption–desorption isotherms (at 77 K) and the pore-size distribution of SBA-15 and the impregnated SBA-15 materials with different metal loading are displayed. The amount of adsorbed nitrogen, which is associated with the specific surface area, is clearly larger for SBA-15 synthesized at 353 K in comparison with SBA-15 prepared at 413 K. The specific surface areas and pore volumes were determined by application of the BET equation and the numerical data are listed in Table 1. The capillary condensation step shows as a sharp increase of the adsorbed N_2 volume at a relative pressure $p/p_0 = 0.6$ – 0.8 with a hysteresis loop type H1 typically of mesoporous materials. The sharpness of this condensation step indicates the uniformity of mesopore sizes. The pore sizes were calculated from the desorption branch of the isotherms. For SBA-15 materials as well as the $\text{MoS}_2/\text{SBA-15}$ and $\text{Co-MoS}_2/\text{SBA-15}$ catalysts a type IV isotherm is observed, which is the typical feature for mesoporous materials [28], evidencing that the incorporation of Co and Mo species does not destroy the mesoporous structure of SBA-15. However, the nitrogen physisorption isotherm of impregnated SBA-15 materials displays some changes: (1) The mean pore diameter is shifted marginally towards higher values after introduction of Mo and Co in SBA-15, a phenomenon which was reported previously [13]; (2) The normalized surface area and pore volume decrease after the incorporation of metal sulfides (Table 1). This effect may be caused by partial pore blocking by the $\text{MoS}_2/\text{Co-MoS}_2$ phases, because the formation of Mo and Co sulfides inside the channels of the SBA-15 material should not significantly affect the pore volume due to their high density. Moreover, the normalized surfaces areas which are related to the pore blocking effects are higher for the $\text{Co-MoS}_2/\text{SBA-15}$ (9 nm) samples (>0.9) than for the catalysts supported on SBA-15 (6 nm) (0.55–0.70). The large pore diameter of 9 nm seems to be more suitable for the application as catalyst support because of the less pronounced pore blocking effects. It should be noted that the surface area of 9 nm SBA-15 (ca. $467 \text{ m}^2/\text{g}$) is obviously lower compared to the 6 nm SBA-15 (ca. $842 \text{ m}^2/\text{g}$, see Table 1).

Table 1 Specific surface area, normalized surface area, pore volume and normalized pore volume of SBA-15 support and Co-Mo sulfide catalysts supported on SBA-15 and the mean MoS₂ crystal size supported on SBA-15

Catalysts	Mo (wt.%)	Co (wt.%)	Pore volume (cm ³ g ⁻¹)		BET surface area (m ² g ⁻¹)		MoS ₂ mean crystal size (nm)
			Normalized	Normalized	Normalized	Normalized	
SBA-15 (6 nm)	0	0	1.11	1	842	1	–
Mo(4)/SBA-15 (6 nm)	3.5	0	0.79	0.75	549	0.70	3.1
Mo(9)/SBA-15 (6 nm)	9.1	0	0.70	0.74	505	0.71	3.6
Mo(16)/SBA-15 (6 nm)	16.3	0	0.58	0.70	388	0.63	3.8
Co(2)Mo(7)/SBA-15 (6 nm)	6.7	1.7	0.63	0.66	474	0.64	3.5
Co(2)Mo(10)/SBA-15 (6 nm)	10.4	1.9	0.53	0.62	363	0.55	3.1
Co(3)Mo(14)/SBA-15 (6 nm)	14.4	2.8	0.52	0.65	396	0.64	6.7
Co(2)Mo(20)/SBA-15 (6 nm)	19.6	1.7	0.39	0.57	299	0.58	4.0
SBA-15 (9 nm)	0	0	1.13	1	467	1	–
Mo(11)/SBA-15 (9 nm)	11.2	0	0.86	0.93	376	0.98	3.4
Co(2)Mo(11)/SBA-15 (9 nm)	11.1	2.0	0.81	0.97	350	0.96	3.9
Co(2)Mo(20)/SBA-15 (9 nm)	20.0	1.7	0.58	0.88	263	0.92	5.1

Normalized(X) = $X_{(Co)_yMo}/((1-y) X_{SBA-15})$, where X is specific surface area (pore volume), y is weight fraction of (Co)Mo sulfides

Fig. 3 Nitrogen adsorption/desorption isotherms (*left*) and BJH pore-size distribution (*right*). (A) SBA-15 (6 nm); (B) Mo(9)/SBA-15 (6 nm) and (C) Co(2)Mo(20)/SBA-15 (6 nm)**Fig. 4** Nitrogen adsorption/desorption isotherms (*left*) and BJH pore-size distribution (*right*). (A) SBA-15 (9 nm); (B) Mo(11)/SBA-15 (9 nm) and (C) Co(2)Mo(20)/SBA-15 (9 nm)

3.3 Transmission Electron Microscopy

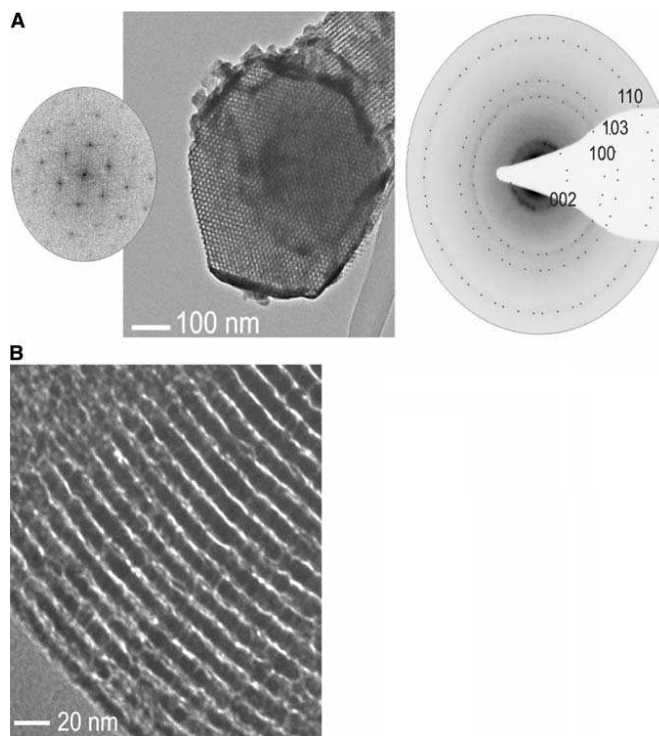
All particles exhibit a well ordered arrangement of cylindrical mesopores as expected for filled SBA-15. The

perfection of the mesoporous structure along the channels axes is exemplified in the bright-field image of Fig. 5a. The hexagonal arrangement of the spots indicates the periodicity which is also supported by the attached Fourier

62

Z.-D. Huang et al.

Fig. 5 Bright field images of Co-Mo/SBA-15 (9 nm): **(a)** Recorded along the channels axis with FFT (left, calculated on a square section) and SAED pattern (right, the d -values match MoS_2); and **(b)** recorded perpendicular to the channels axis



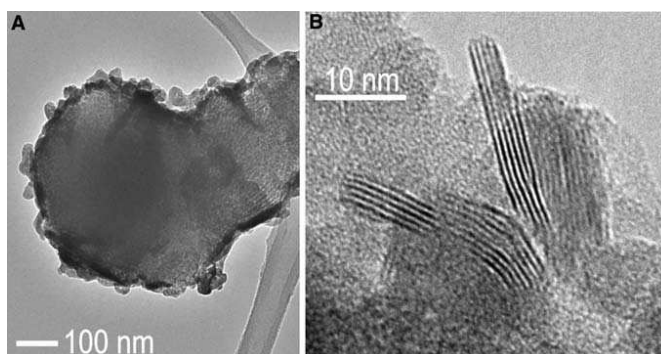
transform (FFT in Fig. 5a, left). The latter exhibits sharp peaks with significant intensity even for the higher order signals. The d -spacing of ca. 10.4 Å matches an average value of d_{100} determined on different particles and in distinct orientations. EDX spectra contain separated peaks for the metals, namely Co- and Mo-K, but coinciding peaks for Mo and S (Mo-L and S-K). Therefore, only the presence of Mo and Co can unambiguously be analyzed. The ratio of Mo:Co varies significantly in different particles. SAED patterns display faint diffuse intensities located on concentric rings around 000. The d -values are close to those expected for MoS_2 (see brackets, [29]): $d_{002} = 6.2$ (6.15) Å, $d_{100} = 2.80$ (2.74) Å, $d_{103} = 2.31$ (2.28) Å, $d_{110} = 1.60$ (1.58) Å supporting the presence of randomly oriented and nanosized CoMoS_2 crystals.

In some areas the diffuse intensity is resolved into broad reflections indicating larger CoMoS_2 crystals which were found to adhere to the surface of the mesoporous host. To check whether the metal containing components are also located inside the pores wide angle tilting and EDX were combined. The particle of Fig. 5b was not covered with Co promoted MoS_2 crystals on the surface as shown by wide

angle tilting, however EDX spectra indicate the presence of Mo and Co, respectively. When aligning the particle perpendicular to the channels axis, the interior of the parallel channels display a random arrangement of dark spots suggesting the presence of CoMoS_2 -nanoparticles inside the host.

In an independent approach in situ transformation was applied to demonstrate the filling of the mesoporous host. The particle of Fig. 5a was irradiated under massive exposure conditions by removing the condenser aperture (increase of the beam current by a factor of 40). The mesoporous structure collapses immediately and releases many CoMoS_2 -nanoparticles onto the surface of the host as evidenced by EDX and SAED, see Fig. 6a. HRTEM micrographs performed on single CoMoS_2 -nanoparticles show the layered structure of the MoS_2 -type, see Fig. 6b. The FFT of a square region of Fig. 6b indicates a layer spacing close to 6.2 Å which corresponds with d_{002} . Such experiments were repeated several times on distinct particles, giving clear evidence for the presence of Co promoted MoS_2 inside the channels of SBA-15. MoS_2 crystallites with average length of 15 nm and average stacking of

Fig. 6 (a) Particle of Fig. 5a after in situ transformation and (b) HRTEM micrograph of MoS₂ particles promoted with Co nanocrystals



about 6 layers (~ 4 nm, in good agreement with the XRD measurements) are observed (Fig. 6b), which are obviously larger than the SBA-15 supported MoS₂ catalysts synthesized from the oxide precursors (length = 2–6 nm, average stacking = 3.5 [11].) The thermal decomposition of ATM on SBA-15 leads to a relatively poor MoS₂ dispersion which may be attributed to the weak interaction between the sulfides and the SBA-15 support with a low number of Si-OH groups and a low acidity.

3.4 Catalytic HDS Activity and Selectivity

The HDS of DBT can occur by two reactions pathways: (I) direct desulfurization (DDS) via C–S bond cleavage leading to the formation of biphenyl (BP), and (II) hydrogenation (HYD) to form phenylcyclohexane (PCH), which is a secondary product yielded from the desulfurization of tetrahydrodibenzothiophene (TH-DBT) and hexahydrodibenzothiophene (HH-DBT). For Ni(Co)-MoS₂ catalysts only TH-DBT can be observed [30]. Therefore, the catalytic selectivity determined from the ratio between HYD and DDS can be approximated by the following equation:

$$S_{\text{HYD}}/S_{\text{DDS}} = ([\text{PCH}] + [\text{TH-DBT}])/[\text{BP}]$$

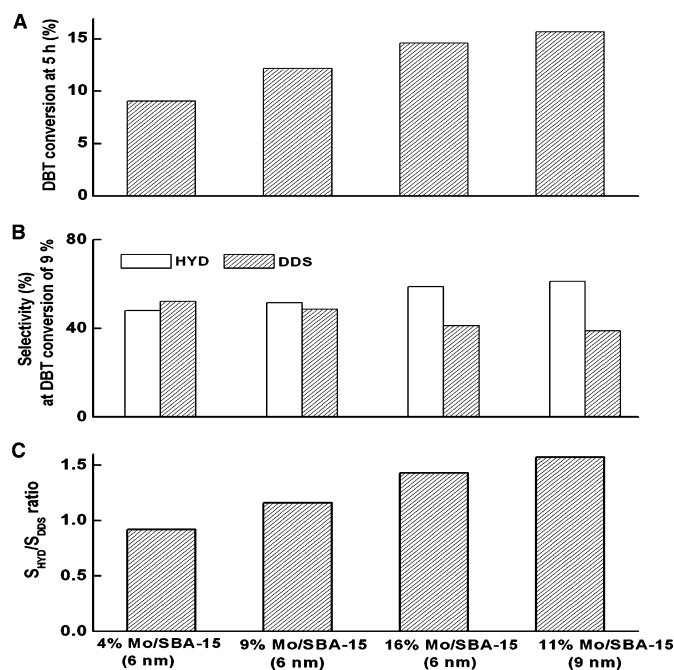
In the present study, the catalytic activity of MoS₂/SBA-15 and Co-MoS₂/SBA-15 catalysts was examined in the HDS of DBT. Several effects can be observed analyzing the measurement results carefully.

Figure 7 illustrates the dependency of DBT conversion and catalytic selectivity as function of Mo loading and pore diameter of SBA-15 for MoS₂/SBA-15 catalysts. For the catalysts supported on 6 nm SBA-15, the increasing catalytic activity is accompanied by a significant increase of the yields of hydrogenation products such as PCH and TH-DBT.

According to the study of Prins et al. [30] the two HDS pathways are determined by the orientation of the adsorbed DBT molecules with respect to the catalysts surface. The DDS pathway occurs through σ adsorption via the sulfur atom and HYD through π adsorption via the aromatic system. The π adsorption is a flat adsorption of the molecules covering a large part of the catalyst surface. Therefore, hydrogenation of DBT should be a sterical demanding reaction pathway. To explain the catalytic selectivity during HDS the rim-edge model was presented by Daage and Chiannelli [31]. The model proposes that hydrogenation of DBT occurs exclusively on rim sites, whereas direct HDS occurs on both rim and edges sites. Assuming this model, the increase of HYD products of the MoS₂/SBA-15 catalysts may be probably caused by the development of a larger amount of rim sites in the active phase. But it should be emphasized that the rim-edge model was proposed for unsupported MoS₂ catalysts. An increasing amount of MoS₂ slabs with increasing Mo loading might be located on the external surface of SBA-15. Therefore, with increasing Mo loading more hydrogenation products can be obtained from the reaction occurring on these externally located MoS₂ slabs because there is no sterical hindering. But one should keep in mind that the external surface area is much smaller compared to the internal surface area.

A confinement effect [17] is obvious comparing MoS₂ catalysts supported on 6 nm and 9 nm SBA-15: a significant enhancement of the hydrogenation reactivity is observed for MoS₂ supported on SBA-15 with the larger diameter of about 9 nm ($S_{\text{HYD}}/S_{\text{DDS}} = 1.57$, 11 wt.% Mo, see Fig. 7), despite the lower Mo loading compared to the catalyst supported on 6 nm material (16 wt.% Mo; $S_{\text{HYD}}/S_{\text{DDS}} = 1.43$). This finding highly suggests that the mesoporous channels of the support are responsible for this effect. The channel diameter of SBA-15 may hinder the sterically demanding π adsorption of DBT molecules and

Fig. 7 HDS of DBT over MoS₂/SBA-15 at $T = 623$ K, $P = 3.4$ MPa: (a) total DBT conversion at 5 h of reaction time; (b) selectivities achieved at a DBT conversion of ca. 9% (different reaction times); (c) $S_{\text{HYD}}/S_{\text{DDS}}$ selectivity ratio achieved at DBT conversion of ca. 9% (different reaction times).



induces the lower $S_{\text{HYD}}/S_{\text{DDS}}$ ratio for 6 nm SBA-15 which shows in addition a significant pore blocking (see the results of nitrogen physisorption measurements).

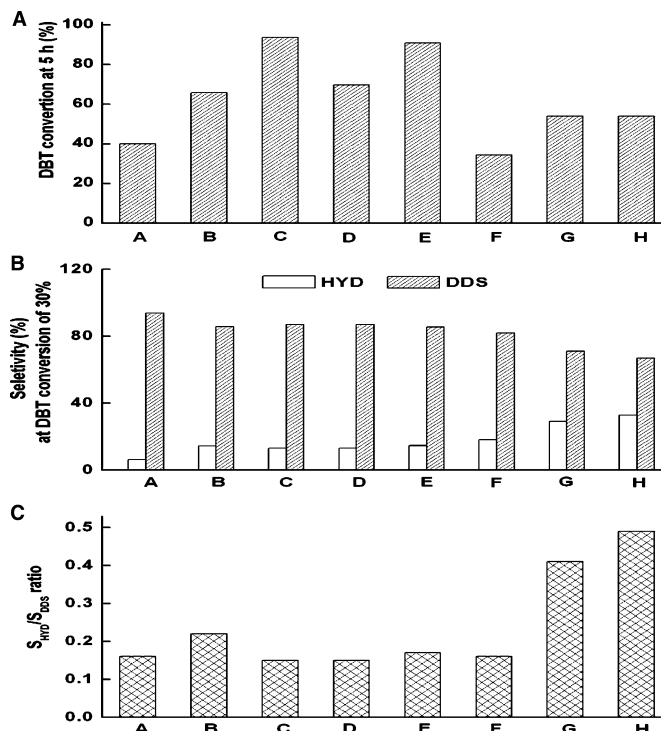
Figure 8 shows the HDS performance and the selectivity of Co-MoS₂/SBA-15 catalysts and the two references taken from [13]. It is obvious that the incorporation of Co yields significantly higher conversions of DBT (4–6 times) compared to the unpromoted MoS₂/SBA-15 catalysts. The catalytic activities of Co-MoS₂/SBA-15 show a systematic increase with increasing Mo content. Moreover, MoS₂/SBA-15 promoted with Co at Mo loadings up ca. 10 wt.% displays also a higher catalytic activity (ca. 62–93% DBT conversion after 5 h) compared with Co-MoS₂/SBA-15 prepared by the oxide precursors (10 wt.% Mo loading, ca. 54% DBT conversion [14]) as well as the commercial CoMo/γ-Al₂O₃ (ca. 53% DBT conversion [14]), despite the presence of the pronounced stacking of MoS₂ slabs and the low Co content (ca. 2%). The enhancement of the catalytic activity is mainly due to the preference for the DDS pathway during the desulfurization of DBT (Fig. 8).

The high HDS activity suggests that MoS₂ stacking is not a prerequisite for a good performance and also not a sign of deactivation or lower activity. This suggestion is in agreement with the study of Eijsbouts et al. [32]. In this study the catalytic activity of unsupported liquid-phase-

sulfided Type 2 commercial ULSD catalysts was compared with respect to the size, shape and stacking of MoS₂. The main result of the investigations is that the synthesis procedure determines the activity of a catalyst. From the occurrence or absence of MoS₂ stacking one cannot conclude whether a catalyst is more or less active. But such a systematic study of supported HDS catalysts was not performed until now.

It is well known that a high HDS performance of the catalysts is connected with the presence of the so-called CoMoS phase with Co atoms being located at the edges of the layered MoS₂ structure [33]. In our experiments the cobalt sulfide is formed first and part of Co species may migrate to the edges of MoS₂ yielding the catalytic active CoMoS phase during the thermal decomposition of ATM. The XRD measurements indicate an increasing formation of CoMoS phase with increasing Mo loading. Moreover, segregated Co₉S₈ (Fig. 2) may play a distinct catalytic role according to the “Remote Control” concept [34]: hydrogen is dissociated to spill-over hydrogen H₂SO on Co₉S₈; it migrates to the surface of MoS₂ or CoMoS phases. In addition, “vacancies” or coordinatively unsaturated sites (“CUS”) which are created by the reaction of hydrogen with surface sulfide groups during the thermal treatment of the ATM precursor in a H₂/N₂ atmosphere may be

Fig. 8 HDS of DBT over Co-Mo/SBA-15 at $T = 623$ K, $P = 3.4$ MPa: (a) Total DBT conversion at 5 h of reaction time; (b) Selectivities achieved at a DBT conversion of ca. 30% (different reaction times); (c) $S_{\text{HYD}}/S_{\text{DDS}}$ selectivity ratio achieved at DBT conversion of ca. 30% (different reaction times), for the samples A: Co(2)Mo(7)/SBA-15 (6 nm); B: Co(2)Mo(10)/SBA-15 (6 nm); C: Co(2)Mo(20)/SBA-15 (6 nm); D: Co(2)Mo(10)/SBA-15 (9 nm); E: Co(2)Mo(20)/SBA-15 (9 nm); F: Co(3)Mo(14)/SBA-15 (6 nm); G: Co(3)Mo(10)/SBA-15 (reported by [13]); and H: CoMo/Al₂O₃ [13]



responsible for high activity of the catalysts. In view of the results of the HRTEM study (poor dispersion of MoS₂ phase) it is most likely that the CUS mainly contribute to the unexpected high catalytic activity.

The selectivity expressed as the $S_{\text{HYD}}/S_{\text{DDS}}$ ratios for our Co-MoS₂/SBA-15 catalysts (~ 0.20) is apparently higher compared to the unpromoted MoS₂/SBA-15 and the commercial CoMo/ γ -Al₂O₃ catalysts (~ 0.49) (Fig. 8), i.e., the Co promoted catalysts show a much lower HYD than DDS in agreement with observations made previously [35]. The significant increase of the selectivity going from pure MoS₂ to Co promoted catalysts is a strong evidence for the generation of the active CoMoS phases. Another factor for the high selectivity may be the special features of the mesoporous SBA-15 support as shown for the unpromoted MoS₂/SBA-15 catalysts. It seems that the mesopores of SBA-15 hinder the flat DBT adsorption through the adsorption of π electrons of DBT (HYD pathway) and favor the direct C–S bond cleavage (DDS pathway) leading to an enhancement of the selectivity (confinement effect). A similar observation was made by Fierro and co-workers where Co-MoS₂/SBA-15 catalysts showed a slightly higher selectivity ($S_{\text{HYD}}/S_{\text{DDS}} \sim 0.4$) compared to a CoMo/ γ -

Al₂O₃ catalyst (~ 0.49) despite that both materials have been prepared via the same route [14]. However, no changes of the selectivity are observed by increasing the Mo loading. In addition, the enlargement of the pore size of SBA-15 from 6 nm to 9 nm (Fig. 8) has also no effect onto the selectivity. Obviously, the confinement effect due to the mesopore channels is here not the dominating effect. An interesting finding is that our catalysts have a clearly higher selectivity (~ 0.2 vs. ~ 0.4) compared to the Co-MoS₂/SBA-15 catalysts prepared by Fierro and co-workers despite the same support material (SBA-15) (Fig. 8). A large number of studies suggest that the hydrogenolysis and hydrogenation reactions occur on separate sites, Lewis acid sites (vacancies) and Brønsted acid sites, respectively [14]. The absence of Brønsted acid sites of the SBA-15 support has been confirmed by means of FTIR spectroscopy [14]. Therefore, the pronounced selectivity for the DDS route could be related to the presence of a large amount of CUS (Lewis acid sites) in our catalysts, which were formed during the thermal treatment of the ATM material under H₂/N₂ atmosphere. Moreover, the hydrogenation of DBT is a steric demanding reaction and the decrease of HYD production may indicate an inhibition of

the flat DBT adsorption on the active sites. Applying the rim-edge model proposed by Daage and Chianelli, the lower HYD activity observed for our catalysts compared to the Co-MoS₂/SBA-15 catalysts prepared by Fierro and co-workers may be due a smaller amount of rim sites in the catalytic active phases.

Based on simple considerations one would expect that 9 nm SBA-15 supported catalysts with a negligible pore blocking should have a significantly higher HDS activity compared with the 6 nm SBA-15 support (larger pore blocking). However, Co-MoS₂/SBA-15 (6 nm) exhibits the highest catalytic activity (Fig. 8) due to the larger specific surface area with respect to 9 nm SBA-15. The optimal atomic Co/Mo ratio of 0.4 was found for γ -Al₂O₃ supported HDS catalysts [36]. Consequently, the cobalt loading was increased in the SBA-15 supported catalysts as an attempt to increase the HDS activity. But the relative high Co loading of about 3 wt.% leads to lower catalytic activity (Fig. 8f) which may be due to the formation of a smaller amount of the active CoMoS phases. Eventually, the higher Co concentration causes a partial pore blocking of the SBA-15 channels thus hindering the dispersion of ATM along the channel walls leading to a poor dispersion of MoS₂ particles (Table 1).

4 Conclusions

We have demonstrated that catalytically active MoS₂ and MoS₂ promoted with Co phases located inside of the pores of the support SBA-15 (HRTEM) can be prepared by thermal decomposition of suitable thiosalt precursors. Despite the large MoS₂ stacking and the presence of long slabs (HRTEM, XRD) the catalysts show a higher HDS activity compared to a commercial CoMo/ γ -Al₂O₃ catalyst. This observation suggests that a good performance for the HDS reaction is not simply related to these structural features of the catalytically active material. An explanation for the observed high HDS activity bases on the co-operative or synergistic effect of a CoMoS phase, Co₉S₈ as well as a large amount of vacancies (CUS). The latter are introduced during the thermal treatment of the ATM precursor in a reducing atmosphere. Hence, the present results are another example that the synthetic route plays an important role for the preparation of active catalysts. For unpromoted MoS₂/SBA-15 catalysts a confinement effect caused by the different sizes of the mesoporous channels is observed. SBA-15 support with the larger channel diameter of 9 nm and a Mo loading of 11 wt.% has a higher activity for the HYD pathway compared to SBA-15 with 6 nm channel diameter and 16 wt.% Mo loading. This result demonstrates the importance of the support for the catalytic activity which was recently discussed in detail [37, 38]. For the catalysts

promoted with Co supported on SBA-15 the confinement effect seems to be less pronounced. Co-MoS₂/SBA-15 (6 nm) exhibits the highest catalytic activity despite the more significant pore blocking compared to Co-MoS₂/SBA-15 (9 nm) (nitrogen physisorption experiments). This observation may be attributed to the larger surface area of the SBA-15 support with the smaller pore size of 6 nm. In total, the results demonstrate that Co-Mo sulfide catalysts using ATM as precursor supported on SBA-15 are good candidates for the conversion of DBT and petroleum residues. Further studies are under way to explore different synthesis routes for the preparation of more active catalysts using SBA-15 as support material.

Acknowledgment The financial support of the Deutsche Forschungsgemeinschaft (DFG) and of the State of Schleswig-Holstein is greatly acknowledged.

References

1. Beck JS, Vartuli JC, Roth WJ, Leonowicz ME, Kresge CT, Schmitt KD, Chu CT-W, Olson DH, Sheppard EW, McCullen SB, Higgins JB, Schlenker JL (1992) *J Am Chem Soc* 114:10834
2. Kresge CT, Leonowicz ME, Roth WJ, Vartuli JC, Beck JS (1992) *Nature* 359:710
3. Zhao D, Feng J, Huo Q, Melosh N, Fredrickson GH, Chmelka BF, Stucky GD (1998) *Science* 279:548
4. Song CS, Reddy KM (1999) *Appl Catal A – Gen* 176:1
5. Wang AJ, Wang Y, Kabe T, Chen YY, Ishihara A, Qian WH (2001) *J Catal* 199:19
6. Wang AJ, Wang Y, Kabe T, Chen YY, Ishihara A, Qian WH, Yao PJ (2002) *J Catal* 210:319
7. Sampieri A, Pronier S, Blanchard J, Breyse M, Brunet S, Fajerweg K, Louis C, Pérot G (2005) *Catal Today* 107–108:537
8. Vradman L, Landau MV, Herskowitz M, Ezersky V, Talianker M, Nikitenko S, Koltypin Y, Gedanken A (2003) *J Catal* 213:163
9. Vradman L, Landau MV, Herskowitz M, Ezersky V, Talianker M, Nikitenko S, Koltypin Y, Gedanken A (2003) *Stud Surf Sci Catal* 146:721
10. Dhar GM, Kumaran GM, Kumar M, Rawat KS, Sharma LD, Raju BD, Rao KSR (2005) *Catal Today* 99:309
11. Gutiérrez OY, Fuentes GA, Salcedo C, Klimova T (2006) *Catal Today* 116:485
12. Gutiérrez OY, Valencia D, Fuentes GA, Klimova T (2007) *J Catal* 249:138
13. Kumaran GM, Garg S, Soni K, Kumar M, Sharma LD, Dhar GM, Rao KSR (2006) *Appl Catal A – Gen* 305:123
14. Nava R, Ortega RA, Alonso G, Ornelas C, Pawelec B, Fierro JLG (2007) *Catal Today* 127:70
15. Coulier L, Kishan G, van Veen JAR, Niemantsverdriet JW (2002) *J Phys Chem B* 106:5897
16. Alonso G, Del Valle M, Cruz J, Petranovskii V, Licea-Claverie A, Fuentes S (1998) *Catal Today* 43:117
17. Alonso G, Berhault G, Aguilar A, Collins V, Ornelas C, Fuentes S, Chianelli RR (2002) *J Catal* 208:359
18. Nava H, Ornelas C, Aguilar A, Berhault G, Fuentes S, Alonso G (2003) *Catal Lett* 86:257
19. Huirache-Acuña R, Albitier MA, Ornelas C, Paraguay-Delgado F, Martínez-Sánchez R, Alonso-Núñez G (2006) *Appl Catal A – Gen* 308:134

20. Brito JL, Severino F, Delgado NN, Laine J (1998) *Appl Catal A – Gen* 173:193
21. Rivera-Muñoz ER, Lardizabal D, Alonso G, Aguilar A, Siadati MH, Chianelli RR (2003) *Catal Lett* 85:147
22. Brieler FJ, Fröba M, Chen LM, Klar PJ, Heimbrodt W, von Nidda HAK, Loidl A (2002) *Chem Eur J* 8:185
23. Brieler FJ, Grundmann P, Fröba M, Chen LM, Klar PJ, Heimbrodt W, von Nidda HAK, Kurz T, Loidl A (2004) *J Am Chem Soc* 126:797
24. Huang Z-D, Bensch W, Sigle W, van Aken PA, Kienle L, Vitoya T, Modrow H, Ressler T (2007) *J Mater Sci* in press
25. Barrett EP, Joyner LG, Halenda PP (1951) *J Am Chem Soc* 73:373
26. Thommes M, Köhn R, Fröba M (2000) *J Phys Chem B* 104:7932
27. Thommes M, Köhn R, Fröba M (2002) *Appl Surf Sci* 196:239
28. Appendix to IUPAC Manual of symbols and terminology, Part 1 (1972) *Pure Appl Chem* 31:579
29. Bronsema KD, de Boer JL, Jellinek F (1986) *Z Anorg Allg Chem* 540:15
30. Prins R, Egorova A, Rothlisberger A, Zhao Y, Sivasankar N, Kukula P (2006) *Catal Today* 111:84
31. Daage M, Chianelli RR (1994) *J Catal* 149:414
32. Eijsbouts S, van den Oetelaar LCA, van Puijenbroek RR (2005) *J Catal* 229:352
33. Topsøe H, Clausen BS (1984) *Catal Rev – Sci Eng* 26:395
34. Karroua M, Matralis H, Grange P, Delmon B (1993) *J Catal* 139:371
35. Bataille F, Lemberon J-L, Michaud P, Pérot G, Vrinat M, Lemaire M, Schulz E, Breyse M, Kasztelan S (2000) *J Catal* 191:409
36. Al-Zeghayer YS, Sunderland P, Al-Masry W, Al-Mubaddel F, Ibrahim AA, Bhartiya BK, Jibril BY (2005) *Appl Catal A – Gen* 282:163
37. Dhar GM, Srinivas BN, Rana MS, Kumar M, Maity SK (2003) *Catal Today* 86:45
38. Breyse M, Afanasiev P, Geantet C, Vrinat M (2003) *Catal Today* 86:5

4.1.2 Characterization and HDS activity investigation of (Ni)CoMo/SBA-15 using cobalt(nickel) thiocarbamate as precursor

Using cobalt acetate as precursor has been demonstrated to be an effective way for the preparation of CoMo/SBA-15 catalysts with high HDS activity. This synthesis method is however not suitable for the preparation of NiMo/SBA-15 catalysts due to the formation of stable NiO during the thermal treatment. Therefore, instead of Co or Ni acetate sulfur-containing Co and Ni complexes (cobalt dimethyldithiocarbamate (CoDMTC), nickel diethyldithiocarbamate (NiDETC)) were applied as precursors in following approach. Moreover, the application of Co and Ni thiocarbamate could retard the sulfidation of Co and Ni promoters beyond the sulfidation of the Mo species, leading to efficient promotion of MoS₂ and a reduced formation of bulk Co or Ni sulfides. In addition to ATM, carbon-containing tetramethylammonium thiomolybdate (TMATM) was also employed. The catalysts were activated either under H₂/N₂ (H₂ = 10%) gas flow at 773 K (*ex-situ*) or during the catalytic test (*in-situ*).

In line with the previous study, the *ex-situ* activated catalysts derived from ATM at high Mo loading exhibit interestingly comparable HDS activities of DBT to a commercial HDS catalyst despite the presence of a large MoS₂ stacking number. The *ex-situ* activation under H₂/N₂ of the catalysts prepared with ATM is beneficial for the generation of large amounts of active sites (CUS). The *ex-situ* activated catalysts using TMATM as precursor represent apparently a lower HDS activity than the catalysts obtained from ATM. A more significant pore blocking is visible for the catalysts prepared with TMATM and therefore pore blocking may be of great importance for HDS activity. Moreover, the catalysts obtained by *ex-situ* decomposition of ATM display MoS₂ slabs, whereas catalysts prepared with TMATM are present as nano-onions of NiMo sulfides or big needle-like aggregates of slabs in the case of CoMo sulfides. The closed shell structure of the nano-onions and the needle-like aggregates of MoS₂ offer a low amount of HDS active edge-sites.

For the *ex-situ* activated catalysts, the HDS activity of CoMo/SBA-15 is higher than for NiMo/SBA-15 catalysts with the same metal loading level, which could be related to the distinct behavior of the promotion atom Co or Ni. In contrast to the absence of Co-rich particles in the CoMo/SBA-15 catalysts, the amorphous and crystalline Ni sulfides enveloped by MoS₂ slabs can be easily detected in the NiMo/SBA-15 catalysts (HRTEM).

Table 3: Comparison of the initial rate constants (k), selectivity HYD/DDS, MoS₂ crystal size (determined from XRD) and BET surface areas of the *ex-situ* and *in-situ* activated HDS catalysts. A: prepared from ATM and B: from TMATM.

Catalysts	Mo wt. %	Co/Ni wt. %	rate constants $\times 10^{-6} \text{ mol s}^{-1} \text{ g}^{-1}$	HYD/DDS	MoS ₂ size nm	BET surface area m ² /g
CoMo/SBA-15(A) <i>ex-situ</i>	11	1.5	1.39	0.24	3.4	303.6
CoMo/SBA-15(A) <i>in-situ</i>	11	1.5	1.10	0.31	2.1	381.5
CoMo/SBA-15(B) <i>ex-situ</i>	11	1.5	7.3	0.23	3.0	227.2
CoMo/SBA-15(B) <i>in-situ</i>	11	1.5	1.26	0.26	2.0	310.1
NiMo/SBA-15(A) <i>ex-situ</i>	10	1.5	0.54	0.79	3.8	314.7
NiMo/SBA-15(A) <i>in-situ</i>	10	1.5	1.28	0.84	2.1	491.5

Using the carbon containing molybdenum compound (TMATM) as precursor, the synergetic effect of the Co promoter is improved by activating the material under *in-situ* conditions (Table 3). An enhancement of the synergetic effect of Ni was already observed for the catalysts prepared from ATM (Table 3). N₂ adsorption-desorption isotherms of the SBA-15-supported Ni(Co)Mo sulfide catalysts keep the characteristic shape of the isotherm of the pristine material (Fig. 16), indicating that the incorporation of Ni(Co)Mo sulfides and the thermal treatment during the catalytic test does not affect the original pore structure of the parent material. Moreover, a less pronounced blocking of the pores is observed for the *in-situ* activated catalysts, which exhibit higher surface areas (Table 3). The enhanced HDS activity observed for the *in-situ* activated catalysts can be explained by the improved MoS₂ dispersion (see Table 3, Fig. 17) ascribed to the positive geometrical effect of carbon and the low pore blocking. The HRTEM investigations are under way to study the change of MoS₂ morphology. In summary, one can conclude that the synergetic effect of Co and Ni depends on both the nature of the precursors and the activation mode.

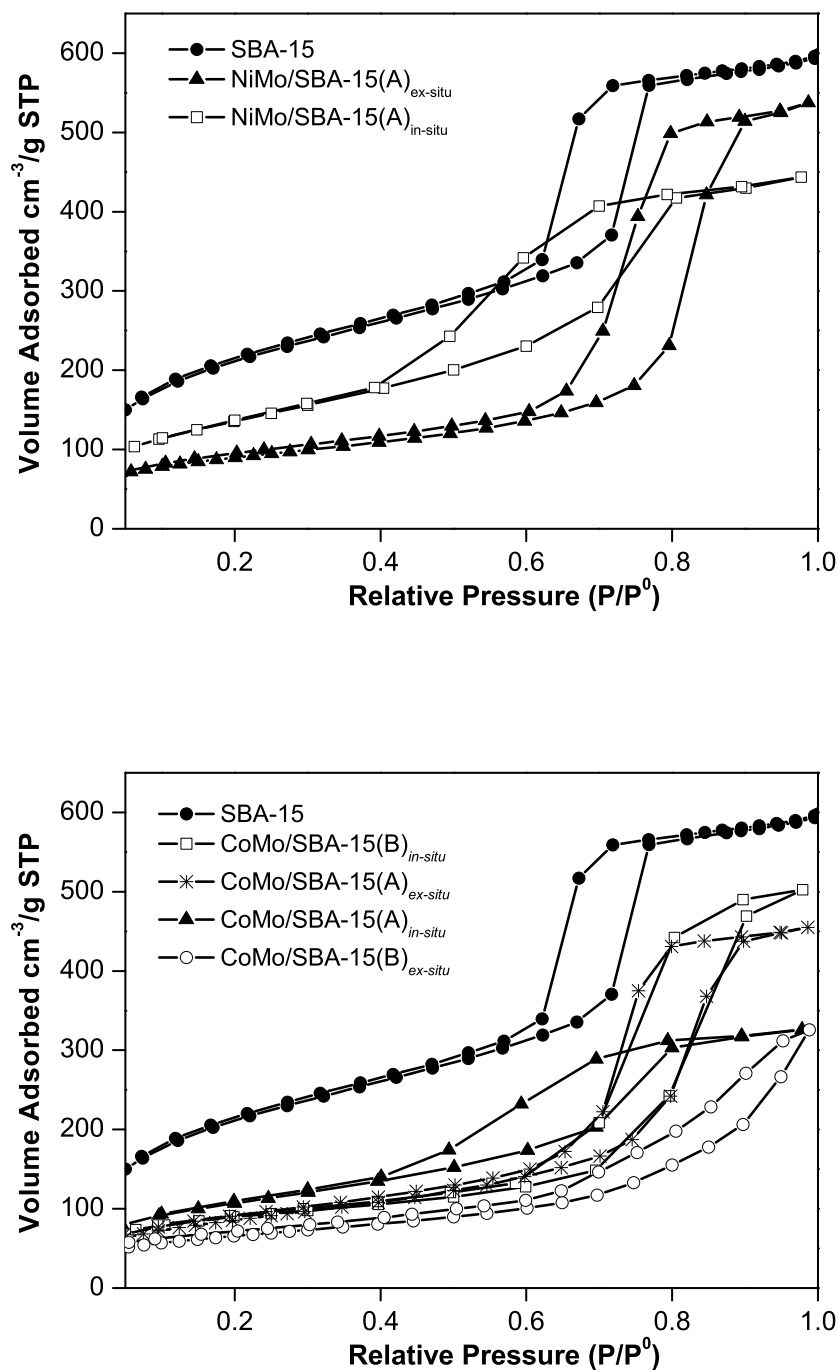


Fig. 16: Nitrogen adsorption-desorption isotherms of SBA-15 and the SBA-15-supported Ni(Co)Mo sulfide catalysts

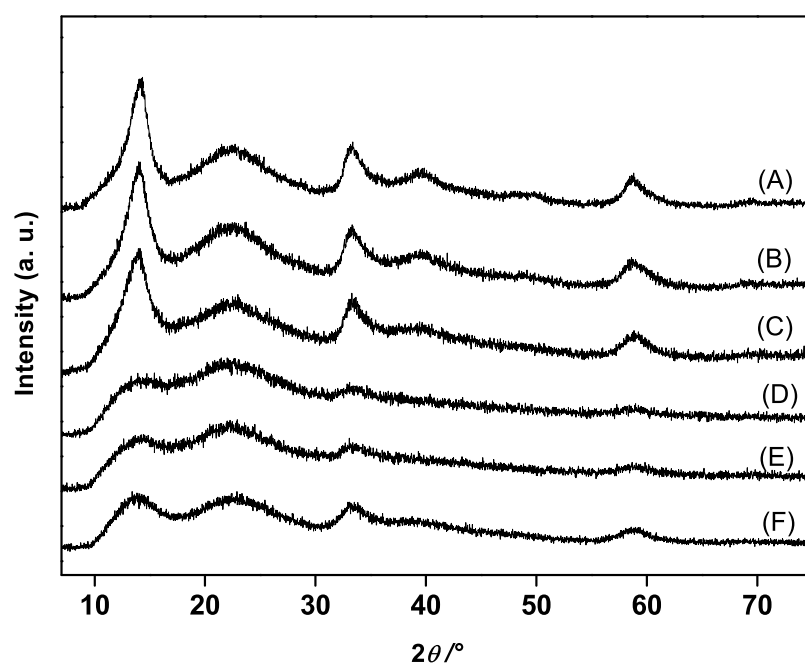


Fig. 17: Wide angle XRD patterns of (A) NiMo/SBA-15(A)_{ex-situ}, (B) CoMo/SBA-15(A)_{ex-situ}, (C) CoMo/SBA-15(B)_{ex-situ}, (D) NiMo/SBA-15(A)_{in-situ}, (E) CoMo/SBA-15(B)_{in-situ} and (F) CoMo/SBA-15(A)_{in-situ}

Catal Lett
DOI 10.1007/s10562-008-9516-3

Preparation and Characterization of SBA-15 Supported Cobalt–Molybdenum Sulfide Catalysts for HDS Reaction: An All Sulfide Route to Hydrodesulfurization Catalysts

Z.-D. Huang · W. Bensch · L. Kienle · S. Fuentes ·
G. Alonso · C. Ornelas

Received: 18 March 2008 / Accepted: 3 May 2008
© Springer Science+Business Media, LLC 2008

Abstract MoS₂ hydrodesulfurization (HDS) catalysts promoted with Co supported on SBA-15 were synthesized from sulfur-containing Mo sources [ammonium thiomolybdate (ATM), and tetramethylammonium thiomolybdate (TMATM)] and Co complexes cobalt dimethylthiocarbamate by using different synthesis strategies in order to achieve active catalysts. The (Co)-MoS₂/SBA-15 catalysts were characterized with X-ray diffraction, N₂-physisorption and High-Resolution Transmission Electron Microscopy. The catalytic performance in the HDS reaction of dibenzothiophene was examined at $T = 623$ K and $P_{H_2} = 3.4$ MPa. The results of the experiments suggest that the sequence of impregnation steps has no significant influence on the HDS activity. On the other hand, the use of different thiomolybdate precursors significantly affects the catalytic activity. The catalysts derived from TMATM show lower HDS activities compared to the catalysts synthesized from ATM which is probably due to the presence of pronounced pore blocking as well as the generation of big needle-like aggregates of the Co–MoS₂ phase. It seems

that the formation of intermediate MoS₃ is not a prerequisite for the generation of catalytic active CoMoS phases. The high activity and high selectivity for the direct desulfurization pathway of catalysts prepared with ATM despite the large MoS₂ stacking could be due to the generation of a large number of coordinately unsaturated sites.

Keywords Hydrodesulfurization · Methylammonium thiomolybdate · Cobalt dimethylthiocarbamate · Co–MoS₂/SBA-15 catalysts · HRTEM · CUS · SBA-15 support · MoS₂ morphology

1 Introduction

Environmental regulation requires lower content of sulfur in diesel engine fuel to 50 ppm by the year 2005 and the sulfur content will be probably reduced even further in the near future. This worldwide environmental pressure on fuel manufacturing has awoken a renewed interest in the preparation of more efficient hydrotreating catalysts. Various preparation methods have been applied to obtain hydrotreating catalysts including comaceration [1], homogenous sulfide precipitation [2] and thiosalt decomposition [3]. Traditionally, hydrodesulfurization (HDS) catalysts contain Mo or W sulfides supported on alumina and promoted with Co or Ni. Recently, mesoporous SBA-15 has been studied as catalyst support material due to the larger pores, thicker pore walls and higher hydrothermal stability compared to other silica molecular sieves such as HMS or MCM-41 [4]. Indeed, Vradman et al. demonstrated the excellent potential of high loading Ni-W/SBA-15 catalysts for deep hydrotreatment of petroleum feedstocks [5]. These catalysts were prepared by ultrasonication deposition of WS₂. SBA-15 supported Mo, CoMo and

Z.-D. Huang · W. Bensch (✉)
Institut für Anorganische Chemie, University of Kiel,
Olshausenstraße 40-60, 24098 Kiel, Germany
e-mail: wbensch@ac.uni-kiel.de

L. Kienle
Max-Planck-Institut für Festkörperforschung, Heisenbergstr. 1,
70506 Stuttgart, Germany

S. Fuentes
Centro de Ciencias de la Materia Condensada, UNAM,
Ensenada, Baja California C.P.22860, Mexico

G. Alonso · C. Ornelas
Centro de Investigación en Materiales Avanzados S. C.,
Chihuahua, Chihuahua C.P. 31109, Mexico

NiMo catalysts was also found by Rao et al. to present higher HDS activity compared to alumina supported catalysts prepared in a similar manner [6]. Further, SBA-15 can be easily modified with various hetero-atoms like Al, Ti and Zr. It was reported by Klimova et al., Rao et al. and Fierro et al. that modified SBA-15 supports exhibit stronger metal-support interactions with respect to pure SBA-15 yielding a high dispersion of the deposited Ni(Co) and Mo active species and consequently greater activity in the HDS [7–10]. In the majority of cases these catalysts were prepared via an oxide route, i.e., SBA-15 was impregnated with transition metal salts like ammonium heptamolybdate, nickel (cobalt) nitrate or nickel (cobalt) acetate and these materials were the calcined to produce stable oxides. Finally, the oxide catalysts were then activated either prior to (ex situ) or during the start-up (in situ) of the hydro-treatment process. However, the calcination step can cause a loss of active metals on the support and a complete sulfidation of the active phase is difficult to achieve [11]. Recently, we reported the synthesis and catalytic performance of SBA-15 supported Co–Mo sulfide catalysts derived from ammonium thiomolybdate (ATM) [12]. The catalysts activated by a gas mixture H_2/N_2 ($H_2 = 10\%$) showed a higher HDS activity compared to a commercial $CoMo/\gamma-Al_2O_3$ material, despite the pronounced MoS_2 stacking and the presence of long MoS_2 slabs. Cobalt acetate has been applied as the Co source and the precursor was sulfided in a H_2S atmosphere to form $CoS_x/SBA-15$ prior to the impregnation with the Mo compound. Moreover, the cobalt sulfide Co_9S_8 was easily detected by X-ray powder diffractometry. In the literature [13–15] it has been reported that the sequence of the formation of the metal sulfides has an important effect onto the development of HDS catalysts. Complexation of Co and Ni with a chelating agent retards the sulfidation of Co and Ni promoters beyond the sulfidation of the Mo species, leading to efficient promotion of the MoS_2 phase and a reduced formation of bulk Co or Ni sulfides. These observations encouraged us to apply a cobalt complex (cobalt dimethylthiocarbamate, CoDMTC) as a precursor instead of Co acetate or Co nitrate for the synthesis of Co promoted MoS_2 catalysts hoping that the generation of less active binary Co sulfide phases will be inhibited by this new approach.

The objectives of the present work are to explore the HDS activity of Co–Mo catalysts supported on mesoporous SBA-15, which were synthesized from S containing Mo sources ATM (TMATM) and the S containing Co complex CoDMTC. The synthesis strategy presented here allows the decomposition of the precursor materials in a H_2/N_2 ($H_2 = 10\%$) gas flow avoiding the usage of toxic H_2S . In general, consecutive impregnation of the support with Co and Mo sources was carried out whereas first CoDMTC was applied

followed by the Mo source. Experiments were also performed with impregnation of the material with CoDMTC after the formation of (Co)Mo sulfides on SBA-15. The different syntheses should allow monitoring the influence of the impregnation order onto the HDS activity of the materials. The supported catalysts were characterized by X-ray diffractometry (XRD), nitrogen physisorption using the Brunauer, Emmett and Teller method (BET) and High-Resolution Transmission Electron Microscopy (HRTEM).

2 Experimental Section

2.1 Sample Preparation

2.1.1 Synthesis of Pristine Mesoporous SBA-15

Eight grams of poly(ethyleneglycol)-block-poly(propylene glycol)-block-poly(ethyleneglycol) triblock copolymer (Aldrich, pluronic, P-123) was dissolved in 240 g of water and 28.6 g of concentrated hydrochloric acid at 303 K on a water bath. After drop wise addition of 16 g of tetraethyl-orthosilicate, the reaction mixture was stirred for 24 h at 303 K. The resulting gel was transferred into a Teflon bottle and heated to 353 K to obtain SBA-15 with 6 nm pores. The resulting white powder was filtered and washed with deionized water, and the surfactant was removed by Soxhlet extraction at 351 K with a mixture of 970 mL of ethanol and 30 mL of concentrated hydrochloric acid. After washing with ethanol, the white powder was dried at room temperature under vacuum for about 1 week.

2.1.2 Synthesis of Co– MoS_2 /SBA-15

Typically, 2 g of SBA-15 was stirred for 4 h in 100 mL of a saturated CoDMTC chloroform solution. Afterwards, the solid was obtained by filtration and the product CoDMTC/SBA-15 was dried under vacuum over night. The precursor material CoDMTC/SBA-15 was stirred in 150 mL of saturated aqueous solutions of ATM at 298 K or (TMATM at 328 K). After 4 h of stirring the products were filtered without washing and then they were activated at 773 K for 3 h under a H_2/N_2 ($H_2 = 10\%$) gas flow at atmospheric pressure. The impregnation/activation cycle was carried out twice to prepare Co– MoS_2 /SBA-15 catalysts with higher Co and Mo loading. Catalysts are named according to their metal loading and type of precursors employed as, e.g., Co(X)Mo(Y)/SBA-15(A) (X is wt% Co and Y is wt% Mo loading, respectively, and A means catalysts prepared from ATM). Co(X)Mo(Y)/SBA-15(B) (B means catalysts synthesized from TMATM).

Two additional samples were prepared through post-impregnation with CoDMTC. The first one was prepared to

enhance the Co concentration of Co–MoS₂/SBA-15. Co–MoS₂/SBA-15 which has been prepared in the above described way using ATM as precursor was treated with 100 mL of a saturated CoDMTC chloroform solution and the product was then activated under the above mentioned conditions. The second catalyst was prepared as follows: 2 g SBA-15 was stirred in 150 mL of saturated aqueous solution of ATM at 298 K. After filtration, the catalyst was calcined at 773 K for 3 h in a H₂/N₂ (H₂, 10%) gas flow at atmospheric pressure. The MoS₂/SBA-15 was treated with a saturated chloroform solution of CoDMTC. After filtration the catalyst was activated applying the above mentioned conditions. These two catalysts are denoted as Co(X)Mo(Y)/SBA-15(C).

For comparative purposes, two unsupported catalysts were prepared as follows: mixtures of the ATM (TMATM) and CoDMTC were manually ground in an agate mortar and Co/Mo ratios were kept at 0.2. The products were then decomposed in a H₂/N₂ (H₂, 10%) atmosphere at 773 K for 3 h. These two catalysts are designed as CoMo(ATM) and CoMo(TMATM).

The precursors ATM and TMATM were synthesized using the method reported previously [16] and the preparation of CoDMTC has been reported by Cambi et al. [17].

2.2 Sample Characterization

X-ray diffraction patterns were measured on a Siemens D5000 diffractometer at room temperature using CuK α radiation ($\lambda = 0.154056$ nm). Nitrogen adsorption measurements were carried out at 77 K on a Quantachrom Autosorb-1. Samples were degassed under flowing argon at 473 K for 2 h before N₂ adsorption. The BET surface areas were calculated from $p/p_0 = 0.03$ – 0.3 in the adsorption branch. The chemical composition of the catalysts (in wt%, average of five measurements at different points of the sample) was determined with energy dispersive X-ray spectroscopy (EDS) analysis with a Philips ESEM XL 30 microscope.

High-Resolution Transmission Electron Microscopy and SAED were performed with a Philips CM 30ST microscope (300 kV, LaB₆ cathode, $C_S = 1.15$ mm). A perforated carbon/copper net served as support of the particles of Co–MoS₂/SBA-15 (6 nm). SAED patterns were obtained using a diaphragm which limited the diffraction to a circular selected area (diameter 250 nm). All images were recorded with a Gatan Multiscan CCD camera and evaluated (including Fourier analyses) with the program Digital Micrograph 3.6.1 (Gatan). EDS analyses were performed in the nanoprobe mode of CM30ST with a Si/Li detector (Noran, Vantage System).

Hydrodesulfurization of dibenzothiophene (DBT) was carried out in a Parr model 4522 high-pressure batch

reactor. 1.0 g of the catalyst and 150 mL of the freshly prepared solution of DBT in decaline (5% wt/wt., [DBT]₀ = 0.2388 mol/L) were introduced in the reactor. The reactor was then purged and pressurized to 3.4 MPa (490 psi) with hydrogen and then heated up to 623 K at a rate of 10 K/min and continuous stirring of 600 rpm. After reaching the working temperature, the products were collected for chromatographic analysis every half an hour to determine the conversion-time dependence during 5 h. After the reaction, the used catalysts were filtered, washed and stored in inert atmosphere. The reaction products were analyzed using a Perkin-Elmer Auto-system chromatograph with a 9 feet long \times 1/8 inch diameter packed column containing chromosorb W-AW 80/100 mesh 3% OV-17 (phenyl methyl silicone 50% phenyl) as a separating phase.

The HDS of DBT occurs by two parallel reaction pathways [18]: (I) direct desulfurization (DDS) via C–S bond cleavage and (II) hydrogenation (HYD). The obtained main products are biphenyl (BP, via DDS), cyclohexylbenzene (CHB, via HYD) and tetrahydrodibenzothiophene (TH-DBT, via HYD). The ratio between HYD and DDS can be approximated in terms of the experimental selectivity according to the following equation:

$$\text{HYD/DDS} = [(\text{PCH}) + (\text{TH} - \text{DBT})]/(\text{BP})$$

The rate constant was determined from the DBT conversion as function of time assuming that DBT conversion being a pseudo-zero order reaction [2] by using of following equation:

$$X_{\text{DBT}} = (1 - \eta_{\text{DBT}})/\eta_{\text{DBT}} = (k/\eta_{\text{DBT},0})t$$

where X_{DBT} is the fraction conversion of DBT, η_{DBT} = moles of DBT, k = pseudo zero order rate constant, t = time in seconds and $k/\eta_{\text{DBT},0}$ is the slope. The mean standard deviation for catalytic measurements was ca. 2.5%.

3 Results

3.1 X-ray Diffraction

X-ray diffraction patterns of SBA-15 and Co–Mo sulfide catalysts supported on SBA-15 are displayed in Fig. 1. For all samples a prominent diffraction peak at about 1.0° 2θ and two distinct weaker reflections between 1.5° and 2.0° 2θ are observed which are the characteristic reflections (100), (110) and (200) of SBA-15 with space group $p6mm$. The occurrence of the characteristic peaks for all catalysts indicates that loading with Co and Mo species does not deteriorate the primary mesostructure of the SBA-15 support. In addition, the intensity of these diffraction peaks

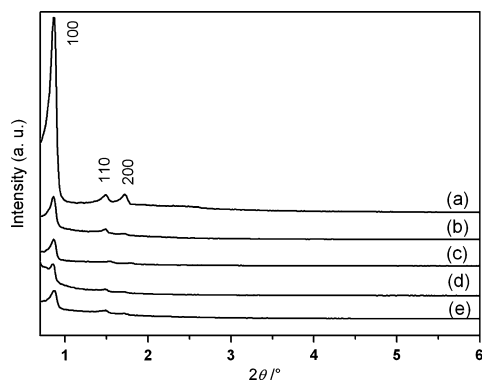


Fig. 1 X-ray diffractometry patterns of **a** parent SBA-15 (6 nm), **b** Co(1.5)Mo(11)/SBA-15(A), **c** Co(2.5)Mo(20)/SBA-15(B), **d** Co(4.0)Mo(20)/SBA-15(C), **e** Co(1.5)Mo(11)/SBA-15(C)

(Fig. 1) decreases after the Co and Mo incorporation. The reduction of the intensity can be explained by the strong absorption of X-rays by Mo(Co) and/or a partial loss of the high order of the mesostructure. The same phenomenon was observed in previous studies [9, 12, 19].

In Fig. 2 the XRD patterns of Co–Mo sulfide catalysts supported on SBA-15 are displayed for the 2θ range from 7° to 75° . The broad modulation at about $22^\circ 2\theta$ is caused by the amorphous silica. For all catalysts typical diffraction patterns of poorly crystalline 2H–MoS₂ with the characteristic reflections at 14.4, 33, 40 and $58^\circ 2\theta$ are observed. The asymmetric shape on the low angle side of the reflections at 33° , 40° and $58^\circ 2\theta$ is a typical feature of layered materials

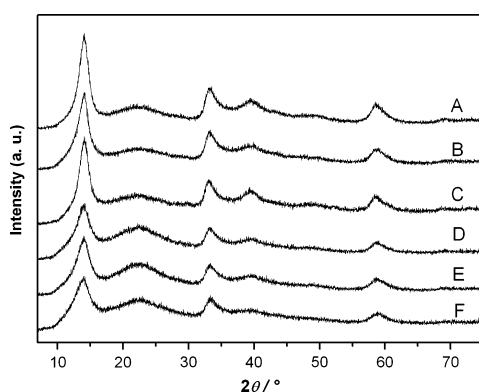


Fig. 2 Wide-angle XRD patterns of **a** Co(2.5)Mo(20)/SBA-15(A), **b** Co(2.5)Mo(20)/SBA-15(B), **c** Co(4.0)Mo(20)/SBA-15(C), **d** Co(1.5)Mo(11)/SBA-15(C), **e** Co(2.5)Mo(11)/SBA-15(A), **f** Co(2.5)Mo(11)/SBA-15(B)

with a partial turbostratic disorder [12, 20]. The average MoS₂ particle size can be determined from the peak width (full width at half maximum, FWHM) and the reflection position using the Scherrer formula, $d = 0.94\lambda / B \cos\theta_B$, where d is the mean diameter of the particle, λ is the wavelength of the Cu K_{α1} line, θ_B is the angle between the incident beam and the reflecting lattice plane and B is the width of the diffraction peak. Using the (002) reflection, the mean MoS₂ particle size is estimated to be 3–4 nm (Table 1), which corresponds to an average of five to six stacked MoS₂ layers along the c -axis assuming 0.613 nm for the MoS₂ slabs. The size of the MoS₂ nanocrystals is smaller than the pore diameter of the SBA-15 material (ca. 6 nm) and it can be assumed that the MoS₂ particles are located inside the channels of SBA-15. From the data compiled in Table 1 it is obvious that the size of the MoS₂ nanocrystals increases with increasing Mo loading. Interestingly, the catalysts derived from the TMATM precursor present somewhat smaller MoS₂ particles compared to the catalysts obtained from ATM. Furthermore, the introduction of Co by post-impregnation seems to have minor influence onto the crystallinity of the MoS₂ particles (Fig. 2d). Independent of the Co content no reflections corresponding to cobalt sulfides can be detected (Fig. 2), indicating that Co is very well-dispersed on the catalytically active material.

3.2 Nitrogen Physisorption

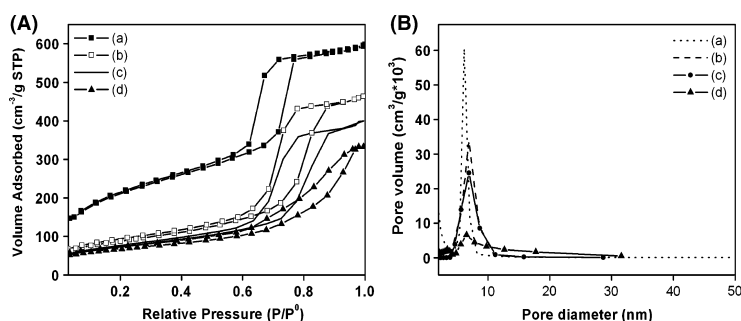
The N₂ adsorption–desorption isotherms (77 K) of the materials are illustrated in Fig. 3. For all Co–MoS₂/SBA-15 catalysts a type IV isotherm is observed, which is the typical feature for mesoporous materials, evidencing that the incorporation of Co and Mo species does not destroy the mesoporous structure of SBA-15. Particularly, the loading of Co–Mo sulfides derived from TMATM led to a typical ink-bottle shape [5] [Fig. 3c, Co(1.5)Mo(11)/SBA-15(B)] caused by small Co–Mo sulfide particles settling within the mesopores. The mean pore diameter is shifted marginally toward higher values after introduction of Mo and Co in SBA-15 suggesting minor changes occurring after the introduction of Mo and Co. A similar phenomenon was described in previous reports [8, 12]. The specific surface areas of SBA-15 and the Co–MoS₂/SBA-15 catalysts are summarized in Table 1. The normalized surface areas were calculated considering dilution effects of the metal loading as described in [21]. The impregnation of the SBA-15 pores with Co–Mo sulfides results in a decrease of surface areas which is caused by a partial pore blocking by the Co–MoS₂ phases, because the formation of Mo and Co sulfides inside the channels of the SBA-15 material should not significantly affect the surface areas due to their high density. A more pronounced blocking of the pores is observed for the catalysts prepared with TMATM, which exhibit the lowest normalized surface areas (Table 1). Moreover, comparing

Preparation and Characterization of SBA-15 Supported Cobalt–Molybdenum Sulfide Catalysts for HDS Reaction

Table 1 Specific surface areas, normalized surface areas of SBA-15 support and SBA-15 supported Co–Mo sulfide catalysts and the mean MoS₂ crystal size supported on SBA-15

Catalysts	Mo (wt. %)	Co (wt. %)	BET surface area (m ² g ⁻¹)		MoS ₂ mean crystallite size (nm)
				Normalized	
SBA-15	0	0	742.2	1	–
Co(1.5)Mo(11)/SBA-15(A)	11	1.5	303.6	0.52	3.4
Co(2.5)Mo(20)/SBA-15(A)	20	2.5	253.7	0.55	4.3
Co(1.5)Mo(11)/SBA-15(B)	11	1.5	227.2	0.39	3.0
Co(2.5)Mo(20)/SBA-15(B)	20	2.5	182.3	0.41	3.6
Co(1.5)Mo(11)/SBA-15(C)	11	1.5	316.4	0.53	3.2
Co(4)Mo(20)/SBA-15(C)	20	4	248.4	0.55	4.4
CoMo(ATM)	67	8	–	–	3.0
CoMo(TMATM)	67	8	–	–	2.1

Normalized (S) = $S_{\text{Co-Mo}} / [(1 - w_f) S_{\text{SBA-15}}]$, where S is the specific surface area, w_f is the weight fraction of CoMo sulfides

Fig. 3 Nitrogen adsorption/desorption isotherms (A) and pore size distribution of (a) parent SBA-15, (b) Co(1.5)Mo(11)/SBA-15(A), (c) Co(2.5)Mo(20)/SBA-15(A) and (d) Co(1.5)Mo(11)/SBA-15(B)

the results obtained for Co(1.5)Mo(11)/SBA-15(A) and Co(1.5)Mo(11)/SBA-15(C) it is obvious that the sequence of the impregnation steps has only a small influence onto the alteration of the surface area. An increase of the Co promoter concentration from 2.5 wt% (Co(2.5)Mo(20)/SBA-15(A)) to 4 wt% (Co(4)Mo(20)/SBA-15(C)) yields no significant change of the surface area (Table 1).

3.3 Transmission Electron Microscopy

The hexagonal mesostructure of the SBA-15 support is preserved after all impregnation procedures, however, the samples prepared from ATM and TMATM exhibit distinct real structure phenomena. Both Co(4)Mo(20)/SBA-15(A) and Co(2.5)Mo(20)/SBA-15(A) obtained from ATM are characterized by a high density of slabs with a low aspect ratio dispersed on the SBA-15 support (Fig. 4). EDS analyses indicate the presence of the slabs by strong peaks of Mo–K and S–K (coinciding with Mo–L) and weak intensity assigned to Co–K. The ratio of Mo:S was calculated to be close to 0.5 in many cases. SAED patterns recorded on the SBA-15 particles show broad diffuse rings with the diameters in good agreement to calculated values based on the metrics of Co–MoS₂ slabs. Bright-field images of these selected areas display a high density of Co–

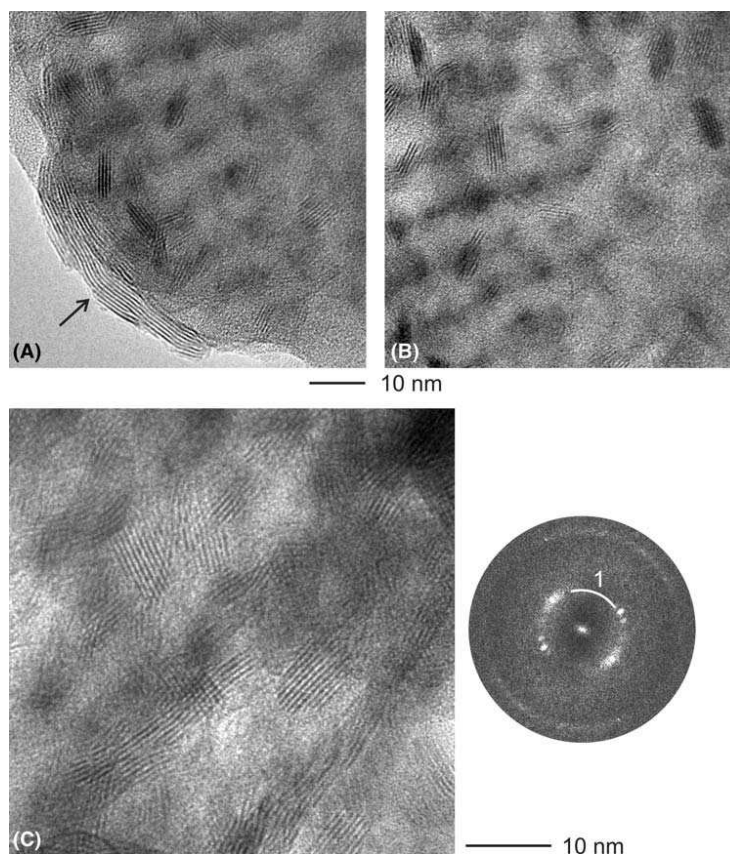
MoS₂ slabs with a typical thickness of ca. 4 nm along the *c*-axis of a MoS₂-type structure. As evidenced by HRTEM these slabs are built from five to eight consecutive (001) layers. With respect to their length, the MoS₂ slabs can be separated in two groups, furthermore a characteristic spatial distribution of short and long slabs is observed (Fig. 4).

(1) Very long slabs which cover the edges of the SBA-15 particles (see arrow in Fig. 4a). The long slabs are frequently bent and exhibit prominent stacking faults. (2) Short slabs with an estimated aspect ratio between 1.5 and 3. They are usually observed apart from the edges of the support, see Fig. 4a (right) and b. HRTEM micrographs (see Fig. 4c) indicate a high density of rotationally disordered slabs with a preferred orientation along the zone axes [*uv*0]. Like electron diffraction patterns, the FFTs of the micrographs contain the high-intensity (002) peak of the Co–MoS₂ phases, see intensity on circle 1 in Fig. 4c, right. For the Co-rich sample Co(4)Mo(20)/SBA-15(A) the slabs do not exhibit a higher Co content. The combined approach of electron diffraction and EDS analyses demonstrate that the Co excess covers wide areas of the SBA-15 support.

The distribution of short and long slabs was not observed for the samples prepared from TMATM, particularly not for the sample Co(2.5)Mo(20)/SBA-15(B). As a rule, areas like the one presented in Fig. 5a with a high density of short slabs

Z.-D. Huang et al.

Fig. 4 Electron microscopy performed on sample Co(2.5)Mo(20)/SBA-15(A). **a** Bright-field image recorded on the edge of a particle of the SBA-15 support. **b** Bright-field image recorded in the center of the particle of image. **c** Bright-field image of SBA-15 support covered by a high density of Co–MoS₂ slabs with attached Fourier transform (calculated inside a circular area of image c)



are rarely observed. The Co–MoS₂ species preferably form big needle-like aggregates of slabs (Fig. 5b). The single slabs are oriented perpendicular to the needles' axes which coincide with the *c* axis of the MoS₂-type structure. Figure 5c displays the HRTEM micrograph recorded on the edge of one needle shown in Fig. 5b. The attached SAED pattern was oriented like the Fourier transform of the HRTEM micrograph. The low resolution of the SAED pattern correlates with the low crystalline perfection of the needle perpendicular to *c* axis. Such phenomenon can be rationalized taking into account the strong bending of adjacent (001) layers which compensates stacking faults.

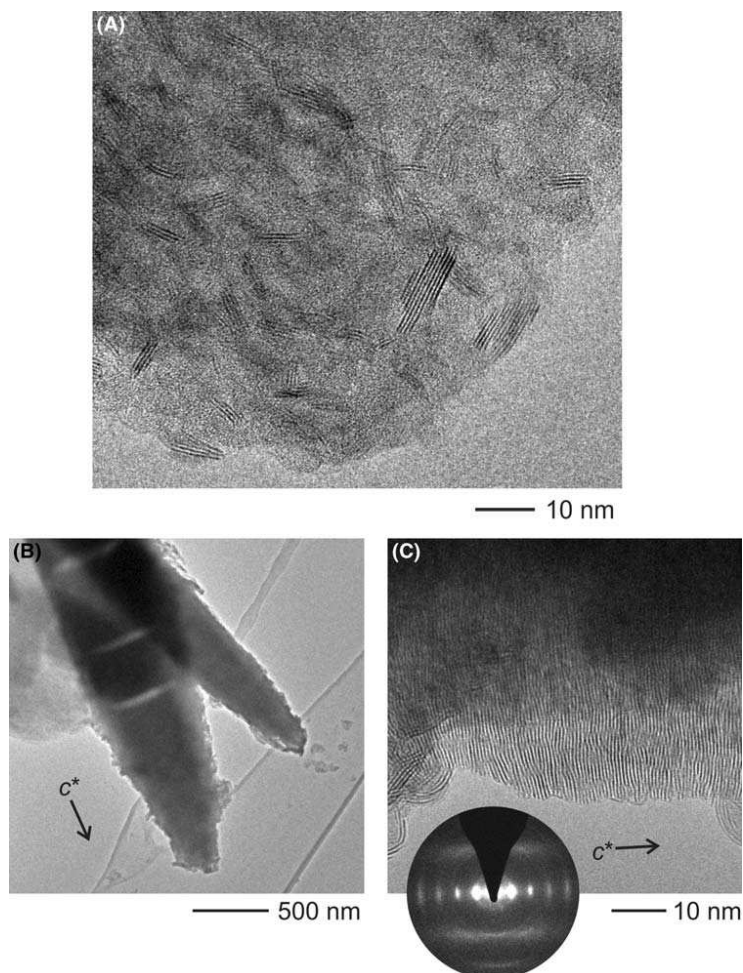
3.4 Catalytic Activity and Selectivity

The results of HDS activity test reactions for Co–MoS₂/SBA-15 catalysts expressed as conversion of DBT as function of the reaction time are displayed in Fig. 6. The

curves show an approximate linear relationship between conversion of DBT and reaction time supporting the assumption of pseudo-zero order kinetics occurring under the experimental conditions. However, deviations from the linear behavior is observed at the end of the reaction for the catalyst with high activity (Fig. 6, Co(4)Mo(20)/SBA-15(C)). Such deviations are due to an inhibiting effect of H₂S accumulated in the reactor. Table 2 presents the calculated pseudo-zero order rate constants for DBT and the selectivity expressed as the ratio HYD/DDS. The results demonstrate that the impregnation order has a smaller influence onto the activity than the nature of the thiomolybdate precursor. For both supported and unsupported catalysts the materials derived from ATM reveal about 40% higher activity than the analogous samples achieved from TMATM (Fig. 6). In addition, all catalysts, regardless of the type of the thiomolybdate source, show a high selectivity at DBT conversions of ca. 30% (HYD/

Preparation and Characterization of SBA-15 Supported Cobalt–Molybdenum Sulfide Catalysts for HDS Reaction

Fig. 5 Electron microscopy performed on sample Co(2.5)Mo(20)/SBA-15(B). **a** Bright-field image of Co–MoS₂ slabs on SBA-15 support. **b** Thick needle of MoS₂ (direction of growth highlighted). **c** HRTEM micrograph recorded at the edge of the needle with attached SAED pattern



DDS ~ 0.2), being in good agreement with the results published in a previous study [12]. The total DBT conversions after 5 h reaction time for all catalysts are displayed in Fig. 7 together with data taken from [12, 22] for comparison. Analyzing the results it is obvious that an increase of Mo and Co loading leads to an increase of the activity, and the catalyst with the highest Co content is the most active in the HDS reaction. With the exception of Co(1.5)Mo(20)/SBA-15(B), all SBA-15 supported catalysts exhibit higher catalytic activity than the commercial CoMo/ γ -Al₂O₃ sample. The unsupported catalyst CoMo(ATM) has a higher HDS performance compared to the catalyst prepared from TMATM, indicating that the Mo

source seems to be important also for unsupported catalysts.

4 Discussion

The thermal decomposition of molybdenum thiosalts was applied as an alternative method for the preparation of HDS catalysts. Using Mo precursors containing alkyl groups instead of the small ammonium ion yield a new type of sulfide materials during the thermal decomposition which could be called “amorphous mesoporous sulfide” catalysts with a remarkable increase of the HDS catalytic

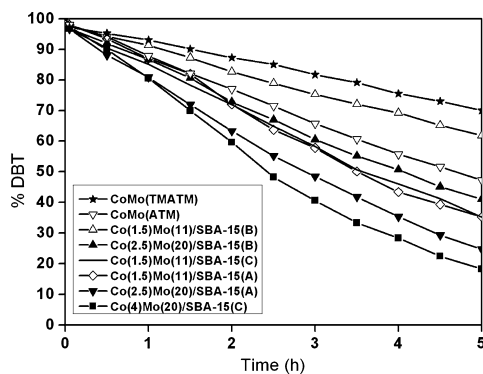


Fig. 6 Dibenzothiophene conversion as function of reaction time for the Co-MoS₂/SBA-15 catalysts

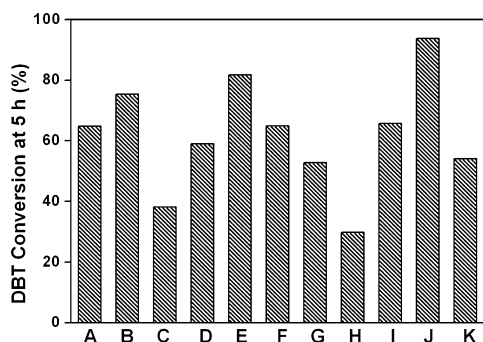


Fig. 7 Total DBT conversion at 5 h of reaction time for the samples **a** Co(1.5)Mo(11)/SBA-15(A); **b** Co(2.5)Mo(20)/SBA-15(A); **c** Co(1.5)Mo(11)/SBA-15(B); **d** Co(2.5)Mo(20)/SBA-15(B); **e** Co(4)Mo(20)/SBA-15(C); **f** Co(1.5)Mo(11)/SBA-15(C); **g** CoMo(ATM); **h** CoMo(TMATM); **i** Co(2)Mo(10)/SBA-15 from reference [12]; **j** Co(2)Mo(20)/SBA-15 from reference [12]; **k** CoMo/Al₂O₃ from reference [22]

activity [20, 23, 24]. Recently, the decomposition of ATM was successfully applied for the preparation of catalysts supported on SBA-15 [12]. In the present study the catalytic active Co-Mo sulfides supported on SBA-15 were obtained using S containing Mo and Co sources ATM, TMATM, and CoDMTC, avoiding any step where an oxidic compound must be transformed to a sulfide. In agreement with previous results [12], the catalysts derived from ATM exhibit interesting high activity at high metal loading despite the relatively pronounced MoS₂ stacking (compare Fig. 4). Such a good HDS performance indicates the presence of a large amount of catalytic active sites, “vacancies” or co-ordinatively unsaturated sites (“CUS”). Nowadays, the most widely accepted model for the

structure of promoted HDS catalysts is the model developed by Topsøe [25]. It was reported that Co substitutes Mo atoms at the S edge creating a tetrahedral environment of Co (Co-Mo-S edge) [26], and it was shown for CoMoS phases that a S atom having bonds to Mo and Co is less strongly bound than a S atom with bonds to two Mo atoms and therefore such a S atom can be removed easily creating a vacancy [25]. The presence of Co located on the MoS₂ slabs confirmed by EDS analyses (see HRTEM) indicates the formation of the CoMoS phase. On the other hand it may be possible that more CUS are generated during the thermal decomposition of the ATM precursor in a H₂/N₂ atmosphere. A high catalytic activity of WS₂ catalysts prepared by decomposition of ammonium tetrathiotungstate in H₂ was reported by Wilkinson et al. to be attributed probably to the presence of more anion vacancies (or more CUS) [27]. However, an improvement of the HDS performance could not be observed compared with the catalysts which were studied by us very recently containing crystalline Co₉S₈ [12]. This finding is somewhat surprising because in the X-ray powder patterns of the present catalysts no hints for crystalline Co sulfides are found (Fig. 2). But it was also reported in the literature that segregated Co₉S₈ might play a distinct catalytic role according to the “Remote Control” concept [28]. This would explain that the present catalysts exhibit a HDS activity comparable to catalysts containing crystalline Co sulfide [12]. But the relatively high HDS activity is in agreement with the results of the study of Eijssbouts et al. [29], who investigated the catalytic activity of unsupported liquid-phase-sulfided Type 2 commercial ULSD catalysts. They pointed out that MoS₂ stacking is not a prerequisite for a good performance and also not a sign of deactivation or lower activity.

The decomposition of TMATM leads to a somewhat lower stacking number of MoS₂ slabs compared to that of ATM (Table 1, Fig. 2). But in addition, the TMATM precursor causes a more pronounced pore blocking (Table 1, Fig. 3) and this effect may be of importance for the catalytic activity. A partial blocking of the pore entrance may lead to a decrease in accessibility of the reactants to the active sites [30, 31]. Moreover, the unsupported CoMo catalyst derived from ATM presents a higher HDS activity than the material prepared from TMATM (Figs. 6, 7 histograms G and H). To explain this result one should therefore consider the different behavior of the two precursors during the thermal decomposition reaction. It was suggested that intermediately formed MoS₃ plays an important role in the formation of the active catalyst supported on so-called activated-carbon [32]. It is well-established that the thermal decomposition of ATM proceeds via intermediately formed MoS₃, whereas TMATM is decomposed directly to a carbon containing

Preparation and Characterization of SBA-15 Supported Cobalt–Molybdenum Sulfide Catalysts for HDS Reaction

Table 2 Initial rate constants (*k*) and selectivity HYD/DDS (estimated at a DBT conversion of ca. 30%) of the Co–MoS₂/SBA-15 catalysts during the HDS reaction of DBT

Catalysts	<i>k</i> (specific) (1 × 10 ^{−7} mol/g s)	HYD/ DDS ratio
Co(1.5)Mo(11)/SBA-15(A)	13.9	0.24
Co(2.5)Mo(20)/SBA-15(A)	15.2	0.19
Co(1.5)Mo(11)/SBA-15(B)	7.3	0.23
Co(2.5)Mo(20)/SBA-15(B)	11.8	0.21
Co(1.5)Mo(11)/SBA-15(C)	13.6	0.21
Co(4)Mo(20)/SBA-15(C)	19.2	0.18
CoMo(ATM)	11.0	0.41
CoMo(TMATM)	5.7	0.29

Mo sulfide [16]. In the case of Co–MoS₂/SBA-15(A), CoDMTC is decomposed simultaneously during the generation of MoS₂ from ATM and Co–MoS₂/SBA-15(C) was prepared by post-impregnation of (Co)MoS₂/SBA-15 with CoDMTC. Both synthesis methods yield catalysts with a comparable surface area. Moreover, at the same Mo and Co loading, the two catalysts present a similar HDS activity (Table 2, Fig. 6 and 7). This result indicates that the Co atoms are able to migrate directly to the edges of MoS₂ to form the active CoMoS phase in both cases. The intermediate MoS₃ seems to be not a prerequisite for the generation of active CoMoS phases under the actual synthesis conditions.

On the other hand, the Co promoting effect might be hindered strongly by carbon entities formed during the decomposition of a tetraalkylammonium thiomolybdate precursor [33], e.g. the cobalt synergetic effect could be completely suppressed like for the ex situ activated Co promoted catalyst using TMATM as Mo source [33]. Unfortunately, the suppression of such a synergetic effect cannot be evaluated by the HRTEM imaging technique. But, the precursor type has shown a strong influence on the MoS₂ morphology detected in HRTEM micrographs. High density of short slabs appears on the catalysts derived from ATM, whereas for the catalysts using TMATM the CoMo species preferably form big needle-like aggregates of slabs with a low crystalline perfection perpendicular to the *c* axis (compare Figs. 4, 5). The distinct MoS₂ morphologies should be mainly responsible for the observed different HDS performance. In summary, it can be concluded that the efficiency of the decomposition process to generate good catalysts depends on the type of the precursor and the chosen conditions [34].

Increasing HDS activity with increasing Mo loading is visible when the same precursor is employed (Table 2). It is well-known that the optimal atomic Co/Mo ratio for γ-Al₂O₃ supported HDS catalysts is 0.4 [35]. Consequently, the cobalt loading of one of the present catalysts

Co(2.5)Mo(20)/SBA-15(A) was increased to this ratio to monitor the change of the HDS activity as function of Co content. Increasing the Co concentration by post-impregnation leads apparently to an increase in HDS activity [see Co(4)Mo(20)/SBA-15(C)]. For this Co-rich sample, the absence of reflections of crystalline Co sulfides in the X-ray powder pattern (Fig. 2) indicates that the usage of CoDMTC retards crystallization of such CoS_x crystallites. Interestingly, the HRTEM/EDS investigation of this sample shows that the Co content is not larger than for Co(2.5)Mo(20)/SBA-15(B). The excess CoS_x species are finely dispersed over the large surface area of SBA-15. The result of the HDS test suggests that the amorphous cobalt sulfide may be responsible for the enhanced HDS activity. But at this stage one can only speculate about the effect of the CoS_x particles onto the enhancement of the HDS activity. One possibility is the so-called spill-over effect but one can also imagine that the finely dispersed CoS_x itself acts as an active catalytic material.

The HYD/DDS ratio of Co–MoS₂/SBA-15 catalysts prepared from different S containing starting materials and different synthesis methods scatters around 0.2 [exception: CoMo(ATM), Table 2], and these ratios are in accordance with the results from our previous study [12]. Multilayered WS₂ slabs have been confirmed by Vradman and Landau to facilitate π-complexation of the aromatic ring with respect to single-layered or thin slabs [36], and consequently result in higher HYD activity. Opposite to that, the present catalysts with multilayered MoS₂ slabs shows a strong preference for the DDS pathway which may be correlated mainly to the promoting effect of Co. It has been proposed that the promoting effect of Co is due to an increased mobility of S atoms in the Co–MoS phase where the strength of the Mo–S bond is considered to be weakened. But the pronounced selectivity for the DDS route could be also related to the presence of a large amount of CUS (Lewis acid sites) in our supported catalysts. Furthermore, the results of different studies suggest that hydrogenolysis and HYD reactions occur on separate sites, i.e., on Lewis acid sites (vacancies) and Brønsted acid sites [22].

5 Conclusions

In the present study an all sulfur route for the preparation of Co promoted MoS₂ catalysts supported on SBA-15 are presented. This method avoids the treatment of the materials in a poisonous H₂S atmosphere. The catalysts obtained from ATM exhibit higher catalytic activity compared to a CoMo/γ-Al₂O₃ catalyst despite of the pronounced MoS₂ stacking. An explanation for the observed high HDS activity and selectivity for the DDS pathway is the co-operative or synergistic effect of a Co–

MoS phase as well as large amount of vacancies (CUS). The synergetic effect of Co depends on the nature of the thiosalt precursor material. In the case of catalysts derived from TMatM, large needle-like aggregates of Co–MoS₂ slabs are formed and a pronounced pore blocking effect is observed. These two properties may be the important factors for the lower HDS activities compared to the catalysts obtained from ATM. In addition, our study highlights that the intermediate MoS₃ is not a prerequisite for the generation of catalytic active Co–MoS phases. A more active catalyst was obtained by increasing the Co content through post-impregnation method due to the positive contribution of amorphous cobalt sulfide to the catalytic performance. In further studies the new synthetic approach is tested with different supports to monitor the influence of the support material onto the catalytic activity and selectivity.

Acknowledgments The financial support of the Deutsche Forschungsgemeinschaft (DFG) and of the State of Schleswig-Holstein is greatly acknowledged.

References

- Hagenbach G, Courty P, Delmon B (1973) *J Catal* 31:264
- Candia R, Clausen BS, Topsøe H (1982) *J Catal* 77:564
- Zdrazil M (1988) *Catal Today* 3:269
- Zhao D, Feng J, Huo Q, Melosh N, Fredrickson GH, Chmelka BF, Stucky GD (1998) *Science* 279:548
- Vradman L, Landau MV, Herskowitz M, Ezersky V, Talianker M, Nikitenko S, Koltypin Y, Gedanken A (2003) *J Catal* 213:163
- Dhar GM, Kumaran GM, Kumar M, Rawat KS, Sharma LD, Raju BD, Rao KSR (2005) *Catal Today* 99:309
- Klimova T, Lizama L, Amezcua JC, Roquero P, Terrés E, Navarrete J, Domínguez JM (2004) *Catal Today* 98:141
- Kumaran GM, Garg S, Soni K, Kumar M, Sharma LD, Dhar GM, Rao KSR (2006) *Appl Catal A Gen* 305:123
- Gutiérrez OY, Fuentes GA, Salcedo C, Klimova T (2006) *Catal Today* 116:485
- Gutiérrez OY, Valencia D, Fuentes GA, Klimova T (2007) *J Catal* 249:138
- Breyse M, Afanasiev P, Geantet C, Vrinat M (2003) *Catal Today* 86:5
- Huang Z-D, Bensch W, Kienle L, Fuentes S, Alonso G, Ornelas C (2008) *Catal Lett* 122:57
- Sundaramurthy V, Dalai AK, Adjaye J (2005) *Catal Lett* 102:299
- Coulter L, Kishan G, van Veen JAR, Niemantsverdriet JW (2002) *J Phys Chem B* 106:5897
- Rana MS, Ramírez J, Gutiérrez-Alejandre A, Ancheyta J, Cedeño L, Maity SK (2007) *J Catal* 246:100
- Poisot M, Bensch W, Fuentes S, Alonso G (2006) *Thermochim Acta* 444:35
- Cambi L, Cagnasso A, Tanara A (1931) *Atti Linc* 13:404
- Whitehurst DD, Isoda T, Mochida I (1998) *Adv Catal* 42:345
- Huang Z-D, Bensch W, Sigle W, van Aken PA, Kienle L, Vitova T, Modrow H, Ressler T (2008) *J Mater Sci* 43:244
- Poisot M, Bensch W, Fuentes S, Ornelas C, Alonso G (2007) *Catal Lett* 117:2007
- Landau MV, Vradman L, Herskowitz M, Koltypin Y, Gedanken A (2001) *J Catal* 201:22
- Nava R, Ortega RA, Alonso G, Ornelas C, Pawelec B, Fierro JLG (2007) *Catal Today* 127:70
- Alonso G, Berhault G, Aguilar A, Collins V, Ornelas C, Fuentes S, Chianelli RR (2002) *J Catal* 208:359
- Nava H, Ornelas C, Aguilar A, Berhault G, Fuentes S, Alonso G (2003) *Catal Lett* 86:257
- Topsøe H, Clausen BS (1984) *Catal Rev Sci Eng* 26:395
- Lauritsen JV, Kibsgaard J, Olesen GH, Moses PG, Hinnemann B, Helveg S, Nørskov JK, Clausen BS, Topsøe H, Lægsgaard E, Besenbacher F (2007) *J Catal* 249:218
- Wilkinson K, Merchan MD, Vasudevan PT (1997) *J Catal* 171:325
- Karroua M, Matralis H, Grange P, Delmon B (1993) *J Catal* 139:371
- Eijsbouts S, van den Oetelaar LCA, van Puijenbroek RR (2005) *J Catal* 229:352
- Furimsky E, Massoth FE (1993) *Catal Today* 17:535
- Absihalabi M, Stanislaus A, Trimm DL (1991) *Appl Catal* 72:193
- Brito JL, Severino F, Delgado NN, Laine (1998) *Appl Catal A Gen* 173:193
- Alvarez L, Espino J, Ornelas C, Rico JL, Cortez MT, Berhault G, Alonso G (2004) *J Mol Catal Chem* 210:105
- Lauritsen JV, Bollinger MV, Lægsgaard E, Jacobsen KW, Nørskov JK, Clausen BS, Topsøe H, Besenbacher F (2004) *J Catal* 221:510
- Al-Zeghayer YS, Sunderland P, Al-Masry W, Al-Mubaddel F, Ibrahim AA, Bhartiya BK, Jibril BY (2005) *Appl Catal A Gen* 282:163
- Vradman L, Landau MV (2001) *Catal Lett* 77:47

1
2
3 **SBA-15 as support for Ni-MoS₂ HDS Catalysts derived from Sulfur-**
4
5 **containing Molybdenum and Nickel Complexes in the Reaction of HDS of**
6
7 **DBT: an all Sulfide Route**
8
9

10
11
12
13
14 *Z.-D. Huang, W. Bensch**
15

16 Institut für Anorganische Chemie, University of Kiel, Olshausenstraße 40-60, 24098 Kiel,
17
18 Germany
19

20
21 *L. Kienle*
22

23 Max-Planck-Institut für Festkörperforschung, Heisenbergstr. 1, D-70506 Stuttgart, Germany
24

25
26 *S. Fuentes¹, G. Alonso^{1,2}, C. Ornelas²*
27

28 ¹Universidad Nacional Autónoma de México, Centro de Nanociencias y Nanotecnología
29
30 Ensenada, B. C. C. P.22860 México
31

32
33 ²Centro de Investigación en Materiales Avanzados S. C., Chihuahua, Chih., C.P. 31109
34
35 México
36

37
38
39
40 * To whom correspondence should be addressed. Tel: +49 431 880-2406, Fax: +49 431 880-
41
42 1520, email: wbensch@ac.uni-kiel.de
43
44
45
46
47
48
49
50
51
52
53
54
55
56
57
58
59
60

1
2
3
4
5
6
7
8
9
10
11
12
13
14
15
16
17
18
19
20
21
22
23
24
25
26
27
28
29
30
31
32
33
34
35
36
37
38
39
40
41
42
43
44
45
46
47
48
49
50
51
52
53
54
55
56
57
58
59
60

Abstract

MoS₂ HDS catalysts promoted with Ni supported on SBA-15 were synthesized from sulfur containing Mo (ammonium thiomolybdate, ATM, and tetramethylammonium thiomolybdate, TMATM) and a Ni complex (Nickel diethylthiocarbamate, NiDETC). The catalysts have been characterized by X-ray diffraction (XRD), N₂-physisorption and High-resolution transmission electron microscopy (HRTEM). The catalytic performance in the hydrodesulfurization (HDS) reaction of dibenzothiophene (DBT) was examined at T = 623 K and P_{H₂} = 3.4 Mpa. In comparison with the impregnation mode, the nature of the employed thiomolybdate complex shows a stronger influence on the MoS₂ morphology and consequently on the HDS activity of DBT. A similar high HDS activity to a commercial NiMo/γ-Al₂O₃ catalyst despite the pronounced stacking number is shown for a Ni-MoS₂/SBA-15 catalyst derived from ATM. The catalysts derived from TMATM showed lower HDS activities compared to the catalysts obtained from ATM precursors due to probably the presence of closed shell structures (nanonions) of MoS₂ which offer significantly smaller amount of HDS active sites (edge sites). Moreover, the HYD/DDS ratios are interestingly higher with respect to the HYD/DDS ratio of the commercial NiMo/γ-Al₂O₃ catalyst which could be ascribed to the generation of multilayered MoS₂ active phase.

Keywords: Hydrodesulfurization, (Alkyl)ammonium thiomolybdate, Nickel diethylthiocarbamate, Ni-MoS₂/SBA-15 HDS catalysts, HRTEM, MoS₂ morphology, nanonion, SBA-15 support.

1. Introduction

It is a world-wide tendency that more stringent environmental regulations require the production of higher quality transportation fuels (gasoline, diesel) with lower sulfur concentration. It is a challenge to synthesize more active hydrodesulfurization (HDS) catalysts for the “deep refining” of crude oil to meet the new strict standards. Conventional γ - Al_2O_3 -supported HDS catalysts are prepared using oxygen-containing transition-metal salts of Mo and W and of Co or Ni. The supported metal salt is calcined to produce stable oxidic materials that must be sulfided either prior to (*ex situ*) or during the start-up (*in situ*) of the hydrotreatment process. It is well known that for the conventional preparation of HDS catalysts via oxide routes, both calcination and sulfidation temperatures have a strong influence on the HDS activity. Incomplete sulfidation according to low sulfidation temperature or high calcination temperature leads to the decrease in HDS activity. Thus, alternate preparation procedures applying e.g. thiosalts in which sulfur is already bound to metal ions have been explored in the last several years.

An attractive support material is the silica SBA-15 which has a large specific surface area and is more thermally stable than the related materials such as HMS or MCM-41 [1]. A high thermal stability is very important for applications in hydrotreating processes performed under the severe HDS reaction conditions like high temperatures and high H_2 partial pressures. Indeed, SBA-15 and hetero-atom containing (Al, Ti or Zr) SBA-15 were found to have excellent potential for deep hydrotreatment of petroleum feedstocks [2, 3, 4-7]. Very recently, CoMo sulfide catalysts supported on SBA-15 derived from ammonium thiomolybdate were reported by us [8, 9]. The catalysts activated in a H_2/N_2 (H_2 10%) gas flow showed a higher HDS activity compared to a commercial CoMo/ γ - Al_2O_3 catalyst.

The aim of the present work is to study the catalytic behavior of NiMo catalysts supported on SBA-15 synthesized from pure sulfur precursors, e.g. S containing Mo (ammonium

1
2
3 thiomolybdate, ATM, and tetramethylammonium thiomolybdate, TMATM) and Ni
4
5 complexes (Nickel diethyldithiocarbamate, NiDETC) in the HDS reaction of DBT. In general,
6
7 consecutive impregnation of SBA-15 support with Ni and Mo compounds was performed
8
9 whereas first NiDETC was applied followed by the Mo sources ATM or TMATM. The
10
11 preparation was also carried out with impregnation of SBA-15 material with NiDETC after
12
13 the generation of (Ni)Mo sulfides. The different synthesis approaches should allow studying
14
15 the effects of impregnation order onto the MoS₂ morphology and the HDS activity. The
16
17 activation of the catalysts was carried out under H₂/N₂ (H₂ 10%) gas flow avoiding any
18
19 treatment in H₂S at high temperatures prior to the activity test. The catalysts are characterized
20
21 with X-ray diffractometry (XRD), N₂ physisorption measurements using the Brunauer,
22
23 Emmett and Teller (BET) method and high-resolution transmission electron microscopy
24
25 (HRTEM). The catalytic HDS performance was tested with DBT in a batch reactor at 623 K
26
27
28
29
30
31
32
33
34
35
36
37
38
39
40
41
42
43
44
45
46
47
48
49
50
51
52
53
54
55
56
57
58
59
60

1
2
3
4
5
6
7
8
9
10
11
12
13
14
15
16
17
18
19
20
21
22
23
24
25
26
27
28
29
30
31
32
33
34
35
36
37
38
39
40
41
42
43
44
45
46
47
48
49
50
51
52
53
54
55
56
57
58
59
60

2. Experimental Section

2.1. Sample preparation

2.1.1. Synthesis of pristine mesoporous SBA-15

The support material was prepared following the route published in [8 - 11].

2.1.2. Synthesis of Ni-MoS₂/SBA-15

2 g of SBA-15 (6 nm) was stirred for 4 h in 100 mL of saturated NiDETC chloroform solution at room temperature. NiDETC/SBA-15 was separated from the slurry by filtration and the obtained material was dried under vacuum over night. This material was then stirred in 150 mL of saturated aqueous solutions of ammonium thiomolybdate (ATM, at 298 K) or tetramethyl ammonium thiomolybdate (TMATM, at 328 K). The impregnation/activation cycle was carried out twice to prepare Ni-MoS₂/SBA-15 (6nm) catalysts with higher Ni and Mo loading. After 4 hours stirring the products were filtered without washing and then they were activated at 773 K for 3 h under a H₂/N₂ (H₂, 10%) gas flow at atmospheric pressure. For comparison purposes, two NiMo sulfide catalysts supported on 9 nm SBA-15 material were also prepared applying the same procedure. The catalysts will be designed according to their metal loading, type of synthesis procedure and type of SBA-15 support employed: Ni(X)Mo(Y)/SBA-15(PA) means the catalyst was prepared with ATM with X wt% Ni and Y wt% Mo loading and P is the pore size of SBA-15 in nm. Ni(X)Mo(Y)/SBA-15 (PB) is the abbreviation for the catalysts synthesized with TMATM.

Two additional samples were prepared by post-impregnation with NiDETC. The first one was prepared as follows: 2 g SBA-15 (6nm) was stirred in 150 mL of saturated aqueous solutions of ATM at 298 K. After filtration the reaction product was calcined at 773 K for 3 h (H₂/N₂ (H₂, 10%) gas flow, atmospheric pressure). The calcined MoS₂/SBA-15 was treated with NiDETC chloroform solution, filtered and activated with the above mentioned conditions. The second catalyst was prepared to enhance the Ni concentration of Ni-MoS₂/SBA-15

1
2
3 catalysts. The Ni-MoS₂/SBA-15(6A) which was prepared by the above described synthesis
4 method was treated in 100 mL of saturated NiDETC chloroform solution, and then the
5 product was activated applying the above mentioned conditions. These two catalysts
6 supported on 6 nm SBA-15 are denoted as Ni(X)Mo(Y)/SBA-15(6C) with X wt% Ni and Y
7 wt% Mo loading.
8
9

10
11 The two Mo sources ATM and TMATM were synthesized with the same method reported
12 previously [12] and the preparation of NiDETC has been published by Jorgensen [13].
13
14

2.2. Sample characterization

15
16 X-ray diffraction (XRD) patterns were measured on a Siemens D5000 diffractometer at room
17 temperature using CuK α radiation ($\lambda = 0.154056$ nm). Nitrogen adsorption measurements
18 were carried out at 77 K on a Quantachrom Autosorb-1. Samples were degassed under
19 flowing argon at 473 K for 2 h before N₂ adsorption. The BET surface areas were calculated
20 from $p/p_0 = 0.03 - 0.3$ in the adsorption branch. The chemical composition of the catalysts (in
21 wt%, average of five measurements at different points of the sample) was determined with
22 energy dispersive X-ray spectroscopy (EDS) analysis with a Philips ESEM XL 30
23 microscope.
24
25

26
27 The supported catalysts were analyzed by high resolution transmission electron microscopy
28 (HRTEM) with a Philips CM 30ST microscope (LaB₆ cathode, 300 kV, C_S = 1.15 mm). The
29 samples were grinded and suspended in n-butanol. One drop of each suspension was placed
30 on a perforated carbon-copper net which serves as support of the particles. SAED (selected
31 area electron diffraction) was carried out using a diaphragm which limited the diffraction to a
32 circular area of 2500 Å in diameter. All images were recorded with a Gatan Multiscan CCD
33 camera and evaluated (including Fourier filtering) with the programs Digital Micrograph
34 3.6.1 (Gatan) or Crisp (Calidris). Chemical analyses by EDS were done in the nanoprobe
35 mode or by spectral imaging (scanning mode) with a Si/Li detector (Noran, Vantage System).
36
37
38
39
40
41
42
43
44
45
46
47
48
49
50
51
52
53
54
55
56
57
58
59
60

1
2
3 The device "Spinning Star" (NanoMEGAS) was applied for precession electron diffraction
4 (PED, precession angle: 3°), simulated patterns were obtained via the software Emaps [14].
5
6

7
8 The HDS reaction of DBT was carried out in a Parr model 4522 high-pressure batch reactor.
9
10 1.0 g of the catalyst and 150 mL of the freshly prepared solution of DBT in decaline (5%
11 wt/wt., [DBT]₀ = 0.2388 mol/L) was introduced in the reactor. The reactor was purged and
12 pressurized to 1.1 MPa with hydrogen and then heated up to 623 K at a rate of 10 K/min
13 under continuous stirring of 600 rpm. After reaching the working temperature and pressure
14 (3.4 MPa), the products were collected for chromatographic analysis every half an hour to
15 determine the conversion-time dependence during 5 h. After the reaction, the used catalysts
16 were filtered, washed and stored in inert atmosphere. The reaction products were analyzed
17 using a Perkin-Elmer Auto-system chromatograph with a 9 ft long x 1/8 inch diameter packed
18 column containing chromosorb W-AW 80/100 mesh 3% OV-17 (phenyl methyl silicone 50%
19 phenyl) as a separating phase.
20
21
22
23
24
25
26
27
28
29
30
31
32

33
34 It is well established that the HDS of DBT occurs by two parallel reactions pathways [15]: (I)
35 direct desulfurization (DDS) via C-S bond cleavage and (II) hydrogenation (HYD). The main
36 products of the HDS reaction are biphenyl (BP, via DDS), cyclohexylbenzene (CHB, via
37 HYD) and tetrahydrodibenzothiophene (TH-DBT, via HYD). The ratio between HYD and
38 DDS can be approximated in terms of the experimental selectivity according to the following
39 equation:
40
41
42
43
44
45
46
47

$$\text{HYD} / \text{DDS} = ([\text{PCH}] + [\text{TH-DBT}]) / [\text{BP}]$$

48
49
50 The rate constant was determined from the DBT conversion as function of time assuming that
51 DBT conversion being a pseudo-zero order reaction [16] by using of following equation:
52
53

$$X_{\text{DBT}} = (1 - \eta_{\text{DBT}}) / \eta_{\text{DBT}} = (k/\eta_{\text{DBT},0}) t$$

54
55 where X_{DBT} is the fraction conversion of DBT, η_{DBT} = moles of DBT, k = pseudo zero order
56 rate constant, t = time in seconds and $k/\eta_{\text{DBT},0}$ is the slope. The mean standard deviation for
57 catalytic measurements was ca. 2.5%.
58
59
60

3. Results

3.1. X-ray diffraction

In Fig. 1 the low angle diffraction patterns of parent SBA-15 and Ni-MoS₂/SBA-15 catalysts are displayed. The three characteristic reflections (100), (110), and (200) of hexagonal mesoporous SBA-15 (space group *p6mm*) are observed for all samples giving strong evidence that the primary structure of SBA-15 consisting of well ordered channels is preserved after the incorporation of NiMo sulfides. The decrease of the Bragg reflection intensity after impregnation may be caused by phase cancellation between the pore walls and the guest species, the strong absorption of X-rays by Mo and/or a partial loss of the high order of the mesostructure. This is a well-known phenomenon and was described previously in the literature [6, 8, 10].

Fig. 2 illustrates XRD patterns of the SBA-15 supported catalysts in the 2θ range from 7° to 75° . Characteristic reflections of poorly crystalline 2H-MoS₂ appear at 14.4 , 33 , 40 , and 58° 2θ . The typical partial turbostratic disorder [8, 17] of layered MoS₂ leads to the occurrence of the asymmetric shape on the low angle side of the reflections (Fig. 2). The broad peak at about 22° 2θ is caused by the amorphous SBA-15 silica. The average MoS₂ crystal sizes can be estimated with the Scherrer formula, $d = 0.941\lambda/B \cos\theta_B$, where d is the mean diameter of the particle, λ is the wavelength of Cu K α_1 (0.154056 nm), θ_B is the angle between the incident beam and the reflecting lattice planes, and B is the width of the diffraction peak (full width at half maximum, FWHM), respectively [8]. From the comparison of the estimated average particle sizes of MoS₂ summarized in Table 1, it is obvious: 1) the sizes of MoS₂ nanoparticles increase with increasing Mo loading; 2) the MoS₂ particle sizes depend on the nature of the precursor used, e.g., the catalyst with the smallest mean MoS₂ crystal size was prepared with TMATM with a Mo loading of 18 wt% (Table 1); 3) larger MoS₂ particles can be observed for the catalysts supported on 9 nm SBA-15 compared to the equivalent samples

1
2
3 supported on 6 nm SBA-15; 4) post impregnation with the Ni complex leads to enlarged
4
5 MoS₂ particle sizes as well as the generation of Ni₃S₂ (Fig. 2G). We want to note that for the
6
7 Co-MoS₂/SBA-15 catalysts prepared by the same methods [9], no crystalline Co sulfide
8
9 phases could be detected. The presence of Ni₂S₃ particles probably related to the fact that
10
11 Ni₃S₂ aggregates more rapidly under the synthesis conditions than Co₉S₈ because of its lower
12
13 Tamman temperature (532 K for Ni₃S₂ versus 686 K for Co₉S₈) [18, 19]. The average MoS₂
14
15 particle size is found to be around 4 nm (Table 1) (corresponds to five to six stacking layers
16
17 along the c-axis), which is a typical MoS₂ size observed for the catalysts supported on SBA-
18
19 15 prepared with ATM [8, 9]. Comparing the size of MoS₂ nanocrystals with the pore
20
21 diameters of the SBA-15 material suggests that the MoS₂ crystallites might be located inside
22
23 the channels of SBA-15.
24
25
26
27
28
29
30
31
32
33
34
35
36
37
38
39
40
41
42
43
44
45
46
47
48
49
50
51
52
53
54
55
56
57
58
59
60

3.2. Nitrogen physisorption

The N₂ adsorption-desorption isotherms (at 77 K) of the catalysts are displayed in Fig. 3. All materials show a type IV isotherm which is a typical feature for mesoporous materials. This observation is another evidence that the incorporation of Ni and Mo species does not destroy the mesoporous structure of SBA-15. Table 1 summarizes the (normalized) BET surface areas of the different materials. The specific surface areas show a strong diminution after formation of Ni-Mo sulfides on SBA-15. This phenomenon can be assigned both to the dilution of the support by the Mo and Ni compounds and the pore blocking effect generated by NiMo sulfides.

Taking the dilution effect into account the so-called normalized surface areas per weight of silica were calculated according to the procedure given in [20]. Higher normalized surface areas are observed for the Ni-MoS₂/SBA-15 (6 nm) catalysts prepared with ATM compared to the catalysts supported on 6 nm SBA-15 using TMATM as precursor. The two NiMo catalysts supported on 9 nm SBA-15 show similar high normalized surface areas independent of the precursor applied for the preparation (see Table 1). A significant influence on the normalized surface area changes according to the impregnation order can be ruled out (Ni(1.5)Mo(10)/SBA-15(6A) versus Ni(1.5)Mo(10)/SBA-15(6C), Table 1). Furthermore, an increase in the concentration of Ni from 2.0 wt% to 4 wt% yields no changes of the normalized surface areas (see Table 1).

3.3. Transmission Electron Microscopy

The different synthesis methods for the catalysts do not affect the medium-range ordering of the mesoporous SBA-15 host which is fully maintained. For all samples, EDS analyses performed on slabs indicate a Mo : S-ratio close to 0.5 and the presence of Ni inside the slabs, however, the length and stacking number of MoS₂ slabs vary strongly. Samples derived from ATM, e. g. Ni(1.5)Mo(10)/SBA-15(6A), Ni(2.0)Mo(18)/SBA-15(6A), Ni(1.5)Mo(10)/SBA-15(6C) and Ni(4.0)Mo(18)/SBA-15(6C), contain a mixture of short and long MoS₂ slabs with low and high aspect ratios, respectively. Depending on their morphology, the slabs are arranged characteristically on the support particles.

Short slabs with an average stacking number of 4-8 are randomly arranged on the SBA-15 support; see Fig. 4a for a SBA-15 particle close to zone axis [001]. The slabs are imaged with high contrast if located on top of a channel of the SBA-15 support (see arrows). Fourier transforms of high resolution micrographs as well as the corresponding electron diffraction patterns contain diffuse and homogeneously distributed intensity on concentric rings around 000. The diameters of the rings correlate well those calculated for MoS₂ [21]. e.g. 1: $d(002) = 6.2 \text{ \AA}$ (calc.: 6.16), 2: $d(100) = 2.7 \text{ \AA}$ (calc. 2.74 \AA), 3: $d(103) = 2.3 \text{ \AA}$ (calc. 2.28 \AA) and 4: $d(110) = 1.6 \text{ \AA}$ (calc. 1.58 \AA), cf. Fig. 4b. Thick slabs with an aspect ratio larger than 8 are bent and aggregate preferably at the edges of the SBA-15 particles (see Fig. 4b). When transmitting such areas, the SAED patterns (inset in Fig. 4b), show concentrations of the diffuse intensity inside the concentric rings due to the increase of the thickness and aspect ratios of the slabs.

The Ni content of thin and thick slabs varies not significantly and is restricted to traces; hence, the actual impregnation techniques do not increase the Ni content inside the slabs. This finding could stem from a preferred formation of Ni-rich byproducts which were actually observed in the form of amorphous and crystalline Ni sulfides. Their composition can not reliably be quantified by EDS due to an intergrowth and superposition of the byproducts with

1
2
3 MoS₂ slabs. The section of an amorphous particle in Fig. 5a shows parallel stripes at the
4 border area. The repeat unit of consecutive stripes as deduced from Fourier transforms and
5 contrast line profiles are consistent with a repeat unit of consecutive MoS₂ slabs according to
6
7
8
9
10
11
12
13
14
15
16
17
18
19
20
21
22
23
24
25
26
27
28
29
30
31
32
33
34
35
36
37
38
39
40
41
42
43
44
45
46
47
48
49
50
51
52
53
54
55
56
57
58
59
60

MoS₂ slabs. The section of an amorphous particle in Fig. 5a shows parallel stripes at the border area. The repeat unit of consecutive stripes as deduced from Fourier transforms and contrast line profiles are consistent with a repeat unit of consecutive MoS₂ slabs according to $d(002) \sim 6.2 \text{ \AA}$. EDS scans at the border areas substantiate an enhancement of Mo-K-, (Mo-L, S-K)-peaks and electron diffraction display the characteristic circles of intensity expected for MoS₂ slabs. Consequently one can conclude that the particles are enveloped by MoS₂ slabs.

Moreover, large faceted and fully crystalline Ni sulfides were observed. Like the amorphous particles, the crystallites are enveloped by MoS₂ slabs, cf. stripes in the bright-field image of Fig. 5c. For the identification of the crystalline Ni-S phase, the quasi kinematical intensity inside precession electron diffraction patterns [22-26] was analyzed. The experimental pattern of Fig. 5b (left) is well approximated by the simulation (Fig. 5b, right) when assuming the structure of Ni₃S₂ (Heazlewoodite, [27]), zone axis [122] for the calculation. In particular, the aberration from fourfold intensity distribution and slight, but characteristic deviations from rectangularity of the metrics are well reproduced ($\angle([01-1]^*, [-111]^* = 88.8^\circ)$). The experimental pattern also shows the concentric rings of diffuse intensity concentrations originating from the MoS₂ slabs surrounding the crystal (see the arrow highlighting the circle with diameter $d(002) \sim 6.2 \text{ \AA}$). Inhomogeneous nanostructures based on a core and MoS₂ shells were frequently observed in the past, even for NiS-MoS₂ core-shell particles [28, 29]. Recently, Ni sulfide segregation decorated with MoS₂ layers were also observed in Type 1/2 Ni-Mo catalysts by TEM [19]. Furthermore, composites with suboxide (MoO_{3-x}) core represent intermediates in the formation of hollow MoS₂ nano-onions [30], however, the latter were never observed in the samples under consideration.

Sample Ni(2.0)Mo(18)/SBA-15(6B) obtained from TMATM exhibits considerable differences in the morphology of the NiMo components. A minor fraction of NiMo slabs was restricted to the thick species with a high aspect ratio. In contrast to all other investigated samples, NiMo nano-onions [30-32] located outside the SBA-15 pore system were identified

1
2
3 as the main component, which are seen in the bright-field image in Fig. 6a and high-resolution
4
5 micrograph of Fig. 7 (left). The EDS mapping in Fig. 6c clearly shows the presence of Mo
6
7 and S inside the nano-onions, and EDS performed in the nanoprobe mode point to an atomic
8
9 ratio Mo : S close to 0.5 and evidence traces of Ni. Hence, the nano-onions are composed of
10
11 bent (Mo,Ni)S₂ layers. Their initial crystalline perfection is low and dominated by defects
12
13 which were described as intrinsic feature particularly of nano-onions with the thickness
14
15 exceeding a critical value [33].
16
17

18
19 The SAED pattern of Fig. 7 (right) was recorded on a single nano-onion. Again, the circles
20
21 correlate with the metrics of MoS₂ slabs, but due to the low crystallinity, the width of the
22
23 circles appears broad compared to the one of crystalline MoS₂ slabs. Accordingly, the bright
24
25 field image of Fig. 7 (left) shows no clear stripes corresponding with MoS₂ slabs at the walls
26
27 of the nano-onions. However, extended times of electron beam irradiation with the dose
28
29 usually applied for HRTEM significantly increase the crystalline quality and the faceting of
30
31 the initially round onions. Such effect could be based on the local heating of the nano-onions
32
33 and the corresponding increase of defect healing. The structural and morphological changes
34
35 depend on the dose. When removing the condenser aperture the dose can be enhanced by a
36
37 factor of 40 with respect to the setting of HRTEM. In that case, EDX analyses evidence that
38
39 the MoNi-nano-onions are at least partially reduced to MoS_{2-x}, and finally the metals (Mo and
40
41 Ni) are formed after long-term irradiation.
42
43
44
45
46
47

48 Like the corresponding dichalcogenide nanotubes, MoS₂ nano-onions exhibit a high potential
49
50 for a plethora of applications [34, 35] For the catalytic activity examined in this work the
51
52 closed shell structures appear unfavorable as one can expect a low edge versus basal surface
53
54 activity.
55
56
57
58
59
60

3.4. Catalytic activity and selectivity

The molar concentration of DBT as a function of reaction time for the catalysts is depicted in Fig. 8. From the approximate linear relationship between conversion of DBT and time (pseudo-zero order kinetics) the initial rate constants were determined. The obtained rate constants and the selectivities calculated at the DBT conversion of ca. 20% are summarized in Table 2. An increasing Mo loading yields an enhanced rate constant, for example, by increasing the Mo content from 10 wt% to 18 wt%, the rate constant increases from 8.1 to 12.3×10^{-7} mol/g s. This observation is similar to the results achieved for Co-MoS₂/SBA-15 catalysts [8, 9]. Comparison of the rate constants determined for Ni(1.5)Mo(10)/SBA-15(6A) (8.1×10^{-7} mol/g.s) and Ni(1.5)Mo(10)/SBA-15(6C) (9.8×10^{-7} mol/g.s) shows that the impregnation order has nearly no influence on the activity. Interestingly, the increase of Ni concentration by post-impregnation results in a decrease in the HDS activity.

For the same metal loading, Ni-MoS₂/SBA-15(9 nm) catalysts have a significantly lower HDS activity compared with Ni-MoS₂/SBA-15(6 nm). Catalysts prepared with TMATM have a lower rate constant than those synthesized with ATM when the SBA-15 support with same pore size is employed, which suggests the great influence of the thiomolybdate complex on the HDS catalytic activity. We note that the catalyst Ni(1.5)Mo(18)/SBA-15(6A) has a similar activity like a commercial catalysts (NiMo/ γ -Al₂O₃) which was characterized under the actual experimental conditions ($k = 12 \times 10^{-7}$ mol/g.s, HYD/DDS = 0.53) [17]. In addition, the HYD/DDS ratios for the present catalysts display a higher selectivity for HYD compared to NiMo/ γ -Al₂O₃.

4. Discussion

The synthesis method using only thiosalts as starting materials yields supported catalysts with an average MoS₂ stacking of 4-8 layers (see XRD and HRTEM). Despite the presence of pronounced MoS₂ stacking the Ni-MoS₂/SBA-15 catalyst (Ni(2.0)Mo(18)/SBA-15(A), $k = 12.3 \cdot 10^{-7}$ mol/g.s) reveals a comparable activity with a commercial NiMo/ γ -Al₂O₃ catalyst. In line with the previous studies [8, 9] [19] [36] the type of the precursor and the actual synthesis conditions seem to be more important for the generation of catalytic active materials. According to the results published by Eijsbouts et al., the MoS₂ stacking is not a prerequisite for a good HDS performance and also not a sign of deactivation or lower HDS activity [19]. One should note that the rigorous study of Eijsbouts et al. was done on unsupported liquid-phase-sulfided Type 2 commercial ULSD catalysts [19]. A large amount of coordinatively unsaturated sites (CUS) which preferably generated in the reductive atmosphere during the thermal decomposition of ammonium thiomolybdate [8] or ammonium thiotungstate [37] might be responsible for the observed similar high activity compared to the optimized commercial NiMo/ γ -Al₂O₃ catalyst.

The Co-MoS₂/SBA-15 catalysts with similar Mo loading prepared with the same synthesis route exhibit apparently higher HDS activity [9] ($k = 15.2 \cdot 10^{-7}$ mol/g.s). This different HDS performance could be due to the different behavior of promotion with Ni or Co. In the case of NiMo sulfide catalysts, it is generally agreed that the promoting effect of Ni is due to an increased mobility of sulfur in the so-called "Ni-Mo-S" phase, in which Ni is present in a square-pyramidal-like structure [38]. Because a S atom in the Ni-S-Mo linkage is less strongly bonded than a S atom between two Mo atoms, it can be removed easily to create catalytic active sites like vacancies or CUS. The amorphous and crystalline Ni sulfides enveloped by MoS₂ slabs can be easily detected in the present Ni-MoS₂/SBA-15 catalysts (see Fig. 5), whereas Co-rich particles in the Co-MoS₂/SBA-15 catalysts [9] could not be detected. This

1
2
3 observation is similar to a previous study where the Co sulfides were amorphous but Ni
4 sulfides appear crystalline [19]. According to the “Remote Control” model segregated
5 crystalline Ni₃S₂ may positively contribute to the catalytic performance [39]. Furthermore,
6
7 increasing the Ni concentration by post-impregnation with NiDETC leads to a significant
8 generation of large faceted Ni₃S₂ crystals (XRD and TEM). The less active Ni₃S₂ might cover
9 the surface of the Ni-Mo-S active phase resulting in a decrease of the HDS activity of DBT
10 (Ni(4)Mo(18)/SBA-15(6C) versus Ni(2)Mo(18)/SBA-15(6C), see Table 2).

11
12
13
14
15
16
17
18
19
20 The catalyst obtained from TMATM (Ni(2)Mo(18)/SBA-15(6B)) shows the lowest activity of
21 all catalysts supported on 6 nm SBA-15. It seems that the more pronounced pore blocking is
22 responsible for the low HDS activity. A partial blocking of the pore entrance may lead to a
23 decrease in accessibility of the reactants to the active sites [40, 41]. However, the catalysts
24 supported on 9 nm SBA-15 prepared with ATM present obviously higher HDS activity than
25 the catalyst obtained with TMATM despite the similar pore blocking for both samples (Table
26 2). To explain this result one should also consider the different behaviour of the two
27 precursors during the thermal decomposition reaction. The lower activities for Ni-
28 MoS₂/SBA(9 nm) compared to that of Ni-MoS₂/SBA-15(6 nm) catalysts with the same metal
29 loading can be related to the poor dispersion of the MoS₂ phase (Table 1). SBA-15 with
30 higher specific surface area and smaller pore size seem to be more beneficial for the
31 generation of highly dispersed MoS₂ particles.

32
33
34
35
36
37
38
39
40
41
42
43
44
45
46
47
48
49
50
51
52
53
54
55
56
57
58
59
60
The decomposition paths of the different complexes could also be one of the causes for the
low HDS activity of the TMATM based catalysts. TMATM decomposes directly to MoS₂
[12], whereas decomposition of ATM proceeds via intermediate formed MoS₃ to MoS₂. It was
suggested that amorphous MoS₃ plays an important role in the formation of the active phase
in activated carbon-supported systems [42]. In the case of Ni-MoS₂/SBA-15(A), NiDETC is
decomposed simultaneously during the generation of MoS₂ from ATM (MoS₃ to MoS₂) and
Ni-MoS₂/SBA-15(C) was prepared by post impregnation of (Ni)MoS₂/SBA-15 with NiDETC.

1
2
3 It should be noted that both synthesis methods have similar effects on the surface areas of the
4 SBA-15 support (Table 1). At the same Mo and Ni loading, the Ni(1.5)Mo(10)/SBA-15(6C)
5 catalyst shows a slightly higher activity than Ni(1.5)Mo(10)/SBA-15(6A) indicating that the
6 intermediate MoS₃ is not a prerequisite for the generation of HDS active phases under the
7 actual synthesis conditions. This result confirms the previous observation achieved for Co-
8 MoS₂/SBA-15 catalysts [9].
9

10
11
12
13
14
15
16
17 Very recently the atomic-scale structures of Co or Ni promoted MoS₂ nanocluster was studied
18 with STM and density functional theory [43]. According to this study Co promoted MoS₂
19 particles have a hexagonal shape and Co atoms prefer ($\bar{1}010$) edges with a 50% S coverage.
20 For Ni promoted MoS₂ a size dependence of the morphologies and the Ni sites was observed.
21 Larger particles are very similar to the Co promoted particles, but smaller clusters adopt
22 dodecagonal shapes with three different edges. All edges contain Ni atoms which fully or
23 partially substitute the Mo atoms. Interestingly, in the present work a strong influence of the
24 precursor type onto the MoS₂ morphology is observed in HRTEM micrographs. Whereas
25 mainly MoS₂ slabs are formed for the catalysts derived from ATM, the catalysts prepared
26 with TMATM appear as nano-onions composed of bent MoS₂ layers with low initial
27 crystalline perfection located outside the pores of the SBA-15 support (compare Figures 4 and
28 6). In the literature it was proposed that the MoS₂ dispersion and particularly the dispersion of
29 edge and corner Mo atoms plays an important role for the catalytic activity [44], whereas the
30 basal plane of MoS₂ is catalytically not active [45]. A decrease of the average MoS₂ slab
31 length causes an increase in MoS₂ edge and corner atom dispersion, resulting consequently in
32 an increase of the catalyst activity for HDN of heavy gas oil derived from Athabasca bitumen
33 [46]. The closed shell structure of MoS₂ nano-onions offers a low amount of the HDS active
34 edge sites. One can conclude that the MoS₂ morphologies observed in the HRTEM pictures
35 for the catalysts prepared with TMATM are mainly responsible for the low HDS activity.
36
37
38
39
40
41
42
43
44
45
46
47
48
49
50
51
52
53
54
55
56
57
58
59
60

1
2
3 The detailed analysis of the reaction product distributions at the same total DBT conversion
4 (20%, Table 2) demonstrates that for all NiMo catalysts with exception of Ni(2)Mo(18)/SBA-
5 15(A) the DDS pathway is slightly preferred, which is a typical promoting effect of Ni. The
6 higher HYD activity compared to the Co-MoS₂/SBA-15 catalysts prepared applying the same
7 method (HYD/DDS = ca. 0.2 [9]) suggests that the active site for HYD is distinct from that
8 for DDS, which is in good agreement with the previous studies [47, 48]. Moreover, the Ni-
9 MoS₂/SBA-15 catalysts prepared from ATM exhibit larger HYD/DDS ratios (0.79 - 1.01)
10 compared to the ratio for the above-mentioned commercial NiMo/ γ -Al₂O₃ catalyst (0.53). We
11 note that similar HYD/DDS ratios were also observed by Alonso et al. for NiMo sulfide
12 catalysts [49]. Unfortunately, no HRTEM images were published so that a comparison with
13 the morphology of the MoS₂ phase in the present work is not possible. HRTEM
14 characterization was performed by Klimova et al. [50] for NiMo sulfide catalysts supported
15 on MCM-41 and on P modified MCM-41. On the pure silica MCM-41 MoS₂ crystallites
16 exhibit lengths between 30 and 60 Å and two to four stacked layers. With a low amount of P
17 the length of the MoS₂ particles decreases and two to three MoS₂ layers were observed. The
18 increased preference for HYD route products after the incorporation of P atoms was attributed
19 to the changes of the morphology of the active phase. For the present catalysts it can be
20 assumed that the higher HYD activity is also related to the morphology of the Ni promoted
21 MoS₂ crystallites. Thicker MoS₂ slabs provide a larger number of vacancies or CUS
22 compared with single-layered or thin slabs. The π -complexation of the aromatic ring on such
23 thick MoS₂ slabs is then easier compared to single-layered or thin slabs [50] and consequently
24 results in higher HYD activity.
25
26
27
28
29
30
31
32
33
34
35
36
37
38
39
40
41
42
43
44
45
46
47
48
49
50
51
52
53
54
55
56
57

58 5. Conclusions

59
60

1
2
3 In this study, Ni promoted MoS₂ catalysts dispersed on SBA-15 as support were prepared
4
5 from sulfur-containing Mo and Ni complexes. The results achieved from XRD, N₂
6
7 physisorption, HRTEM and the HDS catalytic activity of DBT lead to the following
8
9 conclusions:
10
11

- 12 1. One catalyst obtained with ATM as precursor shows a similar high catalytic activity
13 like a NiMo/γ-Al₂O₃ catalyst despite the presence of large stacking number of MoS₂
14
15 layers. This observation may be explained by the presence of a large amount of
16
17 vacancies (CUS) created during the thermal decomposition of ATM in a H₂/N₂
18
19 atmosphere.
20
21
- 22 2. The formation of crystalline Ni sulfides enveloped by MoS₂ slabs is apparently
23
24 observed in the Ni-MoS₂/SBA-15 catalysts. The enhancement of the Ni content by
25
26 post-impregnation leads to the formation of segregated Ni₃S₂ particles, which can
27
28 cover the surface of the Ni-Mo-S phase resulting in a decrease of the HDS activity.
29
30
- 31 3. The precursor type has a stronger influence onto the MoS₂ morphology than the
32
33 impregnation method. The generation of nano-onions composed of bent MoS₂ layers
34
35 with a low crystalline perfection derived from TMATM could be the main factor for
36
37 the low observed HDS activity.
38
39
- 40 4. The multilayered nature of the Ni-MoS₂ phase may be responsible for the higher
41
42 HYD/DDS ratios (0.79 - 1.01) for the Ni-MoS₂/SBA-15 catalysts prepared from ATM
43
44 compared to the ratio for the commercial NiMo/γ-Al₂O₃ catalyst (HYD/DDS = 0.53).
45
46
47
48
49
50
51
52
53
54
55
56
57
58
59
60

1
2
3
4
5
6
7
8
9
10
11
12
13
14
15
16
17
18
19
20
21
22
23
24
25
26
27
28
29
30
31
32
33
34
35
36
37
38
39
40
41
42
43
44
45
46
47
48
49
50
51
52
53
54
55
56
57
58
59
60

Acknowledgements

The authors thank V. Duppel for practical TEM work, Prof. A. Simon for enabling the TEM experiments. Financial support by the Deutsche Forschungsgemeinschaft (DFG, grant BE 1653/22-1)

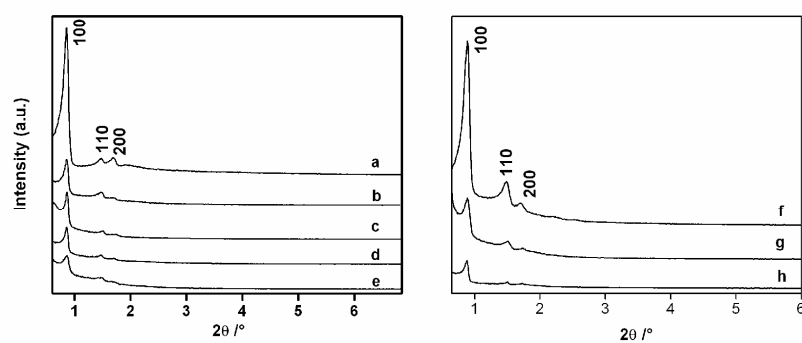
For Peer Review

References

- [1] D. Zhao, J. Feng, Q. Huo, N. Melosh, G.H. Fredrickson, B.F. Chmelka and G.D. Stucky, *Science*, 279 (1998) 548.
- [2] L. Vradman, M.V. Landau, M. Herskowitz, V. Ezersky, M. Talianker, S. Nikitenko, Y. Koltypin and A. Gedanken, *J. Catal.*, 213 (2003) 163.
- [3] G.M. Dhar, G.M. Kumaran, M. Kumar, K.S. Rawat, L.D. Sharma, B.D. Raju and K.S.R. Rao, *Catal. Today*, 99 (2005) 309.
- [4] T. Klimova, L. Lizama, J.C. Amezcua, P. Roquero, E. Terrés, J. Navarrete and J.M. Domínguez, *Catal. Today*, 98 (2004) 141.
- [5] G. M. Kumaran, S. Garg, K. Soni, M. Kumar, L.D. Sharma, G.M. Dhar and K.S.R. Rao, *Appl. Catal. A: Gen.*, 305 (2006) 123.
- [6] O.Y. Gutiérrez, G.A. Fuentes, C. Salcedo and T. Klimova, *Catal. Today*, 116 (2006) 485.
- [7] O.Y. Gutiérrez, D. Valencia, G.A. Fuentes and T. Klimova, *J. Catal.*, 249 (2007) 138.
- [8] Z.-D. Huang, W. Bensch, L. Kienle, S. Fuentes, G. Alonso and C. Ornelas, *Cat. Lett.*, 122 (2008) 57.
- [9] Z.-D. Huang, W. Bensch, L. Kienle, S. Fuentes, G. Alonso and C. Ornelas, *Cat. Lett.*, submitted (2008).
- [10] Z.-D. Huang, W. Bensch, W. Sigle, P.A. van Aken, L. Kienle, T. Vitova, H. Modrow and T. Ressler, *J. Mater. Sci.*, 43 (2008) 244.
- [11] F.J. Brieler, P. Grundmann, M. Fröba, L.M. Chen, P.J. Klar, W. Heimbrodt, H.A.K. von Nidda, T. Kurz and A. Loidl, *J. Am. Chem. Soc.*, 126 (2004) 797.
- [12] M. Poisot, W. Bensch, S. Fuentes and G. Alonso, *Thermochim. Acta*, 444 (2006) 35.
- [13] C.K. Jorgensen, *J. Inorg. Nucl. Chem.*, 24 (1962) 1571.
- [14] E. I.O, *AnaliTEX*, Stockholm, Sweden 2002-2007.
- [15] D.D. Whitehurst, T. Isoda and I. Mochida, *Adv. Catal.*, 42 (1998) 345.
- [16] R. Candia, B.S. Clausen and H. Topsøe, *J. Catal.*, 77 (1982) 564.
- [17] M. Poisot, W. Bensch, S. Fuentes, C. Ornelas and G. Alonso, *Cat. Lett.*, 117 (2007) 43.
- [18] X. J. Zhao and J. Wei, *J. Catal.*, 147 (1994) 429.
- [19] S. Eijsbouts, L.C.A. van den Oetelaar and R.R. van Puijenbroek, *J. Catal.*, 229 (2005) 352.
- [20] M.V. Landau, L. Vradman, M. Herskowitz, Y. Koltypin and A. Gedanken, *J. Catal.*, 201 (2001) 22.
- [21] V. Petkov, S.J.L. Billinge, P. Larson, S.D. Mahanti, T. Vogt, K.K. Rangan and M.G. Kanatzidis, *Phy. Rev. B*, 65 (2002) 092105.
- [22] R. Vincent and P.A. Midgley, *Ultramicroscopy*, 53 (1994) 271.
- [23] J. Gjonnes, V. Hansen and A. Kreneland, *Microsc. Microanal.* 10 (2004) 16.
- [24] T.E. Weirich, J. Portillo, G. Cox, H. Hibst and S. Nicolopoulos, *Ultramicroscopy*, 106 (2006) 164.
- [25] M. Gemmi, X. Zou, S. Hovmoller, A. Migliori, M. Vennstrom and Y. Andersson, *Acta Cryst.*, A59 (2003) 117.
- [26] C. Own, Northwestern University Evanston Illinois, 2005.
- [27] H. Fjellvag and A. Andersen, *Acta. Chem. Scand.*, 48 (1994) 290.
- [28] J.V. Sanders, *Ultramicroscopy*, 20 (1986) 33.
- [29] J.V. Sanders, *J. Electr. Micr. Techn.*, 3 (1986) 67.
- [30] R. Tenne, L. Margulis, M. Genut and G. Hodes, *Nature*, 360 (1992) 444.
- [31] L. Margulis, G. Salitra, M. Talianker and R. Tenne, *Nature*, 365 (1993) 113
- [32] Y. Feldman, E. Wasserman, D.J. Srolovitz and R. Tenne, *Science* 267 (1995) 222.

- 1
2
3 [33] D.J. Srolovitz, S.A. Safran, M. Homyonfer and R. Tenne, *Phys. Rev. Lett.*, 74 (1995)
4 1779.
5
6 [34] M. Bar-Sadan, I. Kaplan-Ashiri, R. Tenne, *Eur. Phys. J. Special Topics* 149 (2007)
7 71.
8
9 [35] G. A. Camacho-Bragado, J. L. Elechiguerra, A. Olivas, S. Fuentes, D. Galvan, M. J.
10 Yacaman, *J. Catal.* 234 (2005) 182.
11 [36] J.V. Lauritsen, M.V. Bollinger, E. Lægsgaard, K.W. Jacobsen, J.K. Nørskov, B.S.
12 Clausen, H. Topsøe and F. Besenbacher, *J. Catal.*, 221 (2004) 510.
13 [37] K. Wilkinson, M.D. Merchan and P.T. Vasudevan, *J. Catal.*, 171 (1997) 325.
14 [38] W.H. Qian, Y. Hachiya, D.H. Wang, K. Hirabayashi, A. Ishihara, T. Kabe, H. Okazaki
15 and M. Adachi, *Appl. Catal. A: Gen.*, 227 (2002) 19.
16 [39] M. Karroua, H. Matralis, P. Grange and B. Delmon, *J. Catal.*, 139 (1993) 371.
17 [40] E. Furimsky and F.E. Massoth, *Catal. Today*, 17 (1993) 535.
18 [41] M. Absihalabi, A. Stanislaus and D.L. Trimm, *Appl. Catal.*, 72 (1991) 193.
19 [42] J.L. Brito, F. Severino, N.N. Delgado and J. Laine, *Appl. Catal. A: Gen.*, 173 (1998)
20 193.
21 [43] J.V. Lauritsen, J. Kibsgaard, G.H. Olesen, P.G. Moses, B. Hinnemann, S. Helveg, J.K.
22 Nørskov, B.S. Clausen, H. Topsøe, E. Lægsgaard and F. Besenbacher, *J. Catal.*, 249 (2007)
23 218.
24 [44] E.J.M. Hensen, P.J. Kooyman, Y. van der Meer, A.M. van der Kraan, V.H.J. de Beer,
25 J.A.R. van Veen and R.A. van Santen, *J. Catal.*, 199 (2001) 224.
26 [45] S. Kasztelan, *Langmuir*, 6 (1990) 590.
27 [46] D. Ferdous, A.K. Dalai, J. Adjaye and L. Kotlyar, *Appl. Catal. A: Gen.*, 294 (2005)
28 80.
29 [47] S. Cristol, J.F. Paul, E. Payen, D. Bougeard, F. Hutschka and S. Clémendot, *J. Catal.*,
30 224 (2004) 138.
31 [48] M. Egorova and R. Prins, *J. Catal.*, 241 (2006) 162.
32 [49] G. Alonso, R.R. Chianelli, S. Fuentes and B. Torres, U.S Patent 2007.
33 [50] J.M. Herrera, J. Reyes, P. Roquero and T. Klimova, *Micropor. Mesopor. Mater.*, 83
34 (2005) 283.
35 [51] L. Vradman and M.V. Landau, *Cat. Lett.*, 77 (2001) 47.
36
37
38
39
40
41
42
43
44
45
46
47
48
49
50
51
52
53
54
55
56
57
58
59
60

1
2
3 Figure 1: XRD patterns of (a) parent SBA-15 (6 nm), (b) Ni(1.5)Mo(10)/SBA-15(6A), (c)
4 Ni(2.0)Mo(18)/SBA-15(6B), (d) Ni(1.5)Mo(10)/SBA-15(6C), (e)
5 Ni(4.0)Mo(18)/SBA-15(6C), (f) parent SBA-15 (9 nm), (g) Ni(1.5)Mo(10)/SBA-
6 15(9A), (h), Ni(1.5)Mo(10)/SBA-15(9B)
7
8
9
10
11
12
13
14
15
16
17
18
19
20
21
22
23
24
25
26
27
28
29
30
31
32
33
34
35
36
37
38
39
40
41
42
43
44
45
46
47
48
49
50
51
52
53
54
55
56
57
58
59
60



1
2
3 Figure 2: Wide-angle XRD patterns of A) Ni(1.5)Mo(10)/SBA-15(9B), B)
4 Ni(1.5)Mo(10)/SBA-15(9A), C) Ni(1.5)Mo(10)/SBA-15(6C), D)
5 Ni(2.0)Mo(18)/SBA-15(6B), (E) Ni(1.5)Mo(10)/SBA-15(6A), (F) Ni(2)Mo(18)/SBA-
6 15(6A), (G) Ni(4.0)Mo(18)/SBA-15(6C)

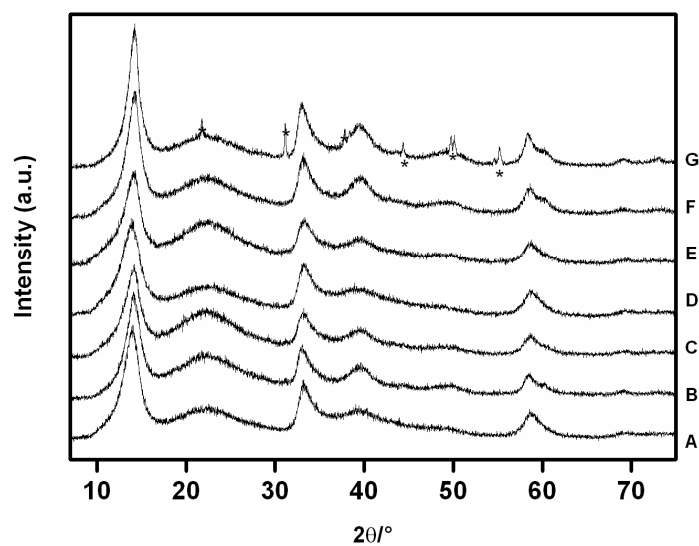
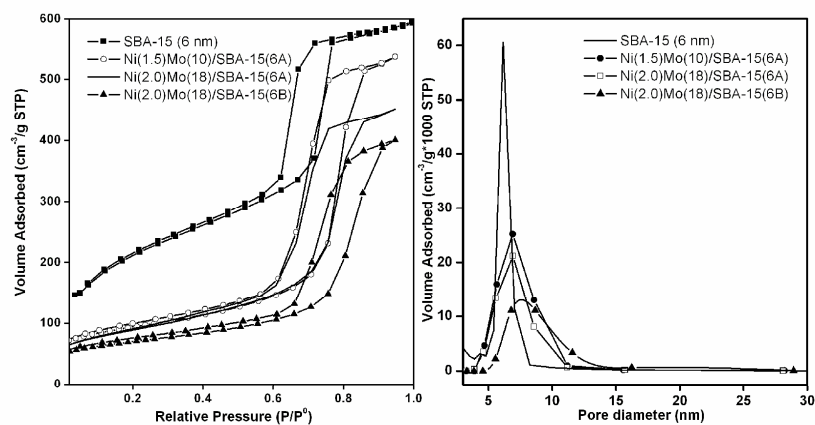
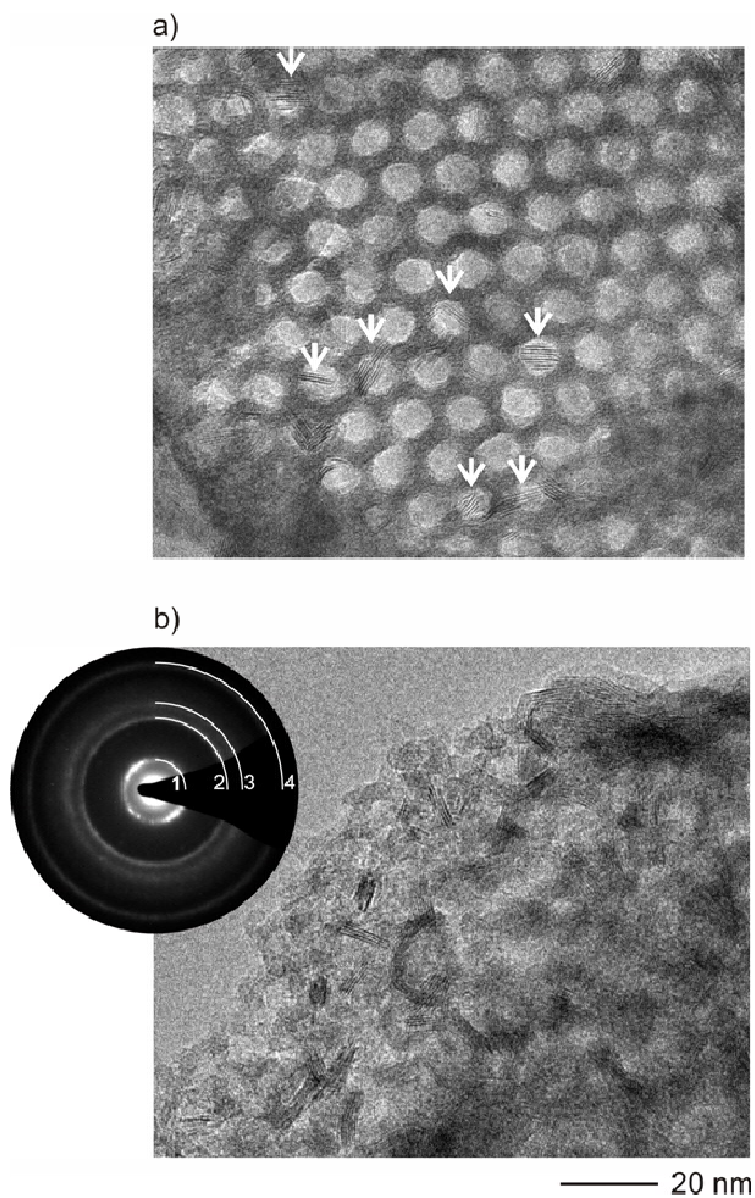


Figure 3: Nitrogen adsorption/desorption isotherms of Ni-MoS₂/SBA-15 catalysts.

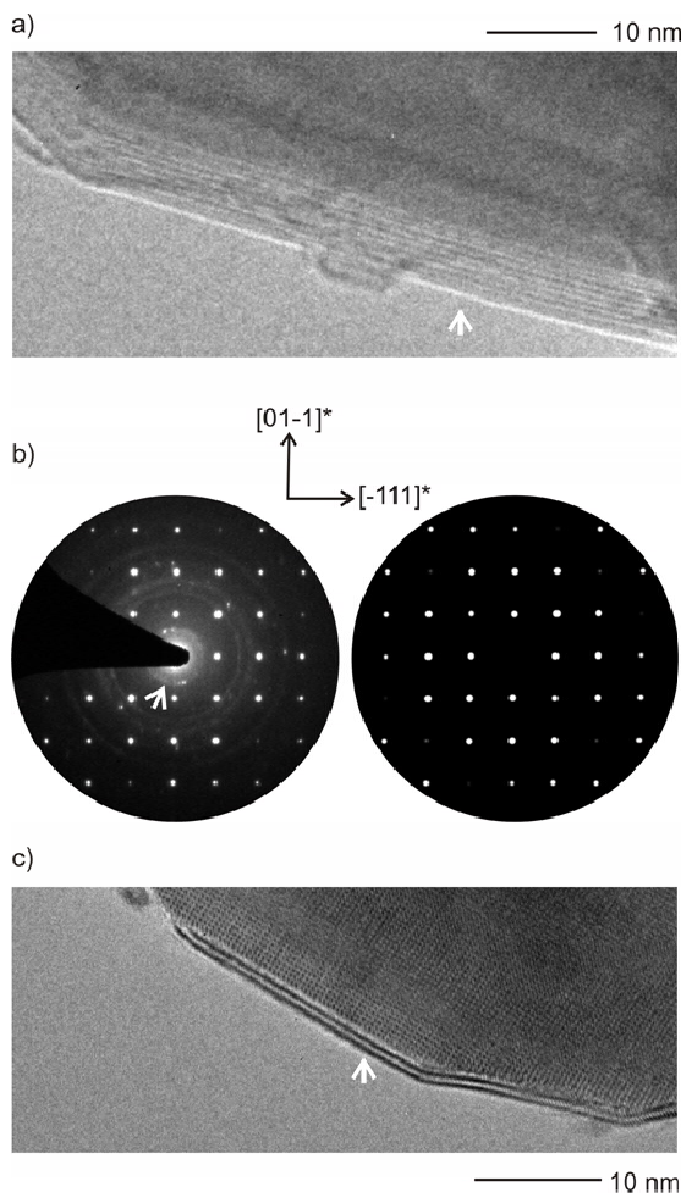
Peer Review

Figure 4: a) NiMo-slabs with small aspect ratios (sample Ni(2.0)Mo(18)/SBA-15(6A)) dispersed on a SBA particle, b) aggregation of long slabs at the edge of SBA particles with inserted SAED pattern.

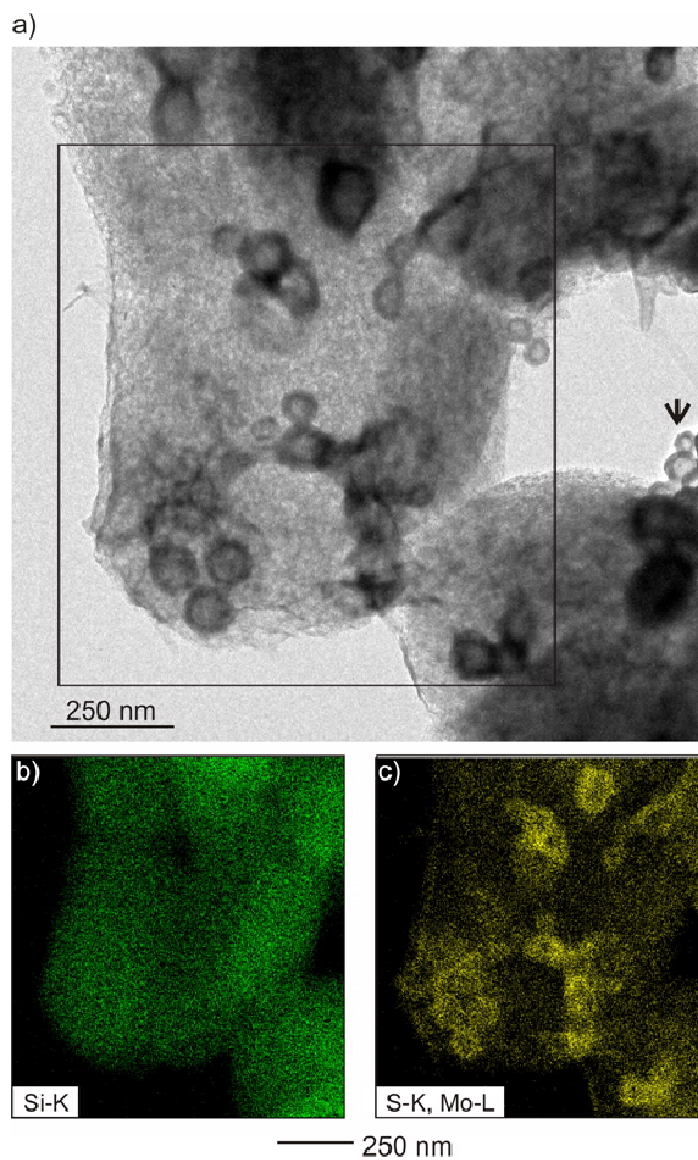


1
2
3
4
5
6
7
8
9
10
11
12
13
14
15
16
17
18
19
20
21
22
23
24
25
26
27
28
29
30
31
32
33
34
35
36
37
38
39
40
41
42
43
44
45
46
47
48
49
50
51
52
53
54
55
56
57
58
59
60

Figure 5: a) Border area of an amorphous Ni-sulfide with thick coating by MoS₂ slabs, see arrow. b) Experimental PED pattern (left) and simulation (right, based on Ni₃S₂, zone axis [211]). c) Crystallite of Ni₃S₂ with thin coating by MoS₂ slabs, see arrow.



1
2
3 Figure 6: a) Bright-field image recorded on a SBA particle of sample Ni(2.0)Mo(18)/SBA-
4
5 15(6B). EDS mapping based on the peaks of Si-K (b) and S-K, Mo-L (c).
6
7
8
9



1
2
3
4
5
6
7
8
9
10
11
12
13
14
15
16
17
18
19
20
21
22
23
24
25
26
27
28
29
30
31
32
33
34
35
36
37
38
39
40
41
42
43
44
45
46
47
48
49
50
51
52
53
54
55
56
57
58
59
60

Figure 7: High-resolution micrograph of MoS₂ onions (cp. arrow in Fig. 6) with intergrowth and attached SAED pattern, Nano-onions before (left) and after (right) extended times or irradiation.

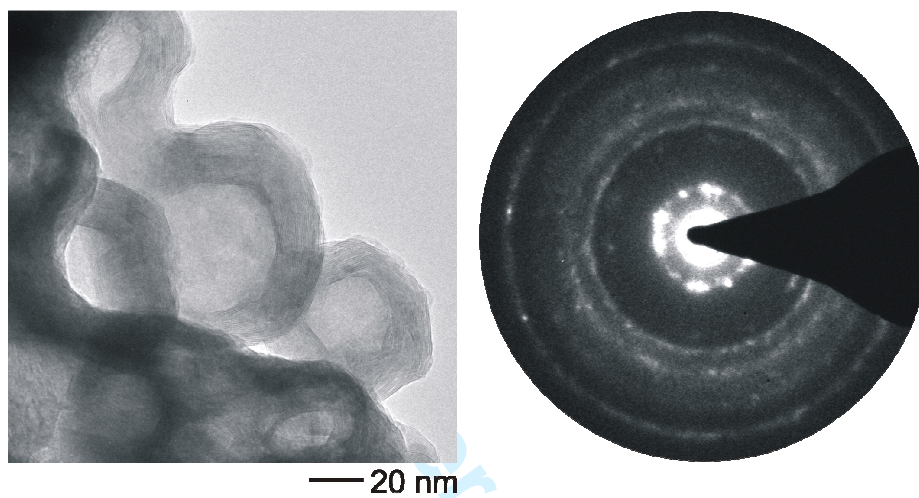


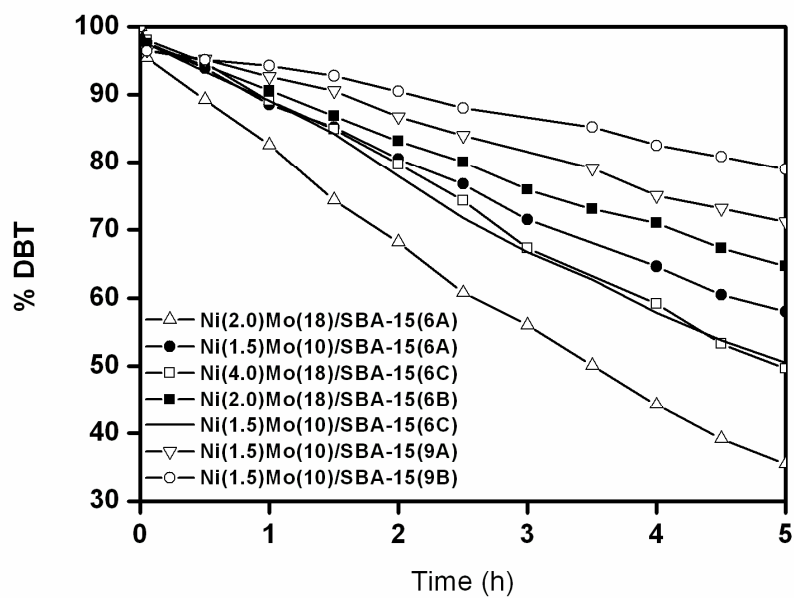
Figure 8: DBT conversion as function of reaction time for the Ni-MoS₂/SBA-15 catalysts.

Table 1: Specific surface area, normalized surface area of SBA-15 support and NiMo sulfide catalysts supported on SBA-15 and the mean MoS₂ crystal size. Normalized(S) = S_{NiMo} / ((1-wf) S_{SBA-15}), where S is specific surface area, wf is the weight fraction of NiMo sulfides.

Catalysts	Mo wt. %	Ni wt. %	BET surface area (m ² g ⁻¹)	Normalized	
					MoS ₂ Mean Crystal size (nm)
SBA-15 (6 nm)	0	0	742.2	1	-
Ni(1.5)Mo(10)/SBA-15(6A)	10	1.5	314.7	0.55	3.8
Ni(2.0)Mo(18)/SBA-15(6A)	18	2.0	298.9	0.59	4.3
Ni(2.0)Mo(18)/SBA-15(6B)	18	2.0	232.2	0.48	3.6
Ni(1.5)Mo(10)/SBA-15(6C)	10	1.5	315.9	0.54	3.9
Ni(4.0)Mo(18)/SBA-15(6C)	18	4.0	285.3	0.59	4.8
SBA-15 (9 nm)	0	0	457	1	-
Ni(1.5)Mo(10)/SBA-15(9A)	10	1.5	324.3	0.88	4.3
Ni(1.5)Mo(10)/SBA-15(9B)	10	1.5	312.6	0.85	3.8

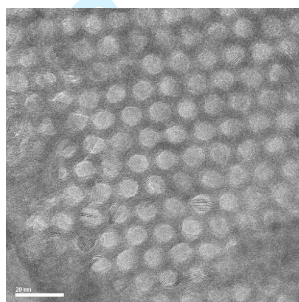
Table 2: Initial rate constants (k) and selectivity HYD/DDS (achieved at a DBT conversion of ca. 20 %) of the Ni-MoS₂/SBA-15 catalysts and a commercial NiMo/ γ -Al₂O₃ during the HDS reaction of DBT (T = 623 K, P_{H2} = 3.4 MPa).

Catalysts	k (specific)(1 *10 ⁻⁷ mol/g s)	HYD/DDS ratio
Ni(1.5)Mo(10)/SBA-15(6A)	8.1	0.79
Ni(2.0)Mo(18)/SBA-15(6A)	12.3	1.01
Ni(2.0)Mo(18)/SBA-15(6B)	6.6	0.56
Ni(1.5)Mo(10)/SBA-15(6C)	9.8	0.89
Ni(4.0)Mo(18)/SBA-15(6C)	10.0	0.83
Ni(1.5)Mo(10)/SBA-15(9A)	5.4	0.79
Ni(1.5)Mo(10)/SBA-15(9B)	3.6	0.62
NiMo/ γ -Al ₂ O ₃	12.0	0.53

1
2
3
4
5
6
7
8
9
10
11
12
13
14
15
16
17
18
19
20
21
22
23
24
25
26
27
28
29
30
31
32
33
34
35
36
37
38
39
40
41
42
43
44
45
46
47
48
49
50
51
52
53
54
55
56
57
58
59
60

Graphical abstract

Nickel promoted molybdenum sulfide catalysts supported on mesoporous SBA-15 were prepared by an all sulfide route using Mo and Ni thiosalts. Similar high catalytic activity to a NiMo/ γ -Al₂O₃ catalyst at high Mo loading is observed for Ni-MoS₂/SBA-15 catalysts derived from ammonium thiomolybdate despite a pronounced stacking of MoS₂ slabs. The catalysts prepared with tetramethylammonium thiomolybdate show lower HDS activities probably due to the generation of nano-onions composed of bent MoS₂ with a low crystalline perfection. The enhancement of the Ni content by post-impregnation leads to the formation of segregated Ni₃S₂ particles, which can cover the surface of the Ni-Mo-S phase resulting in a decrease of the HDS activity. The multilayered nature of the Ni-MoS₂ phase may be responsible for the higher HYD/DDS ratios (0.79 - 1.01)



4.1.3 (Ni)CoMo/SBA-15 and CoW/SBA-15 catalysts prepared by the solvent evaporation route

The above presented HDS catalysts were prepared by a two-step synthesis which is characterized by impregnation/filtration and calcination. This preparation method yields an excellent dispersion of the catalysts on the surface of the support. However, the metal-support interaction is an important prerequisite for the metal loading on the support materials. For example, low W-loading (ca. 2 wt.%) was obtained using ammonium thiotungstate (ATT) as precursor. Another disadvantage is that the final loading of active species is rarely known and requires subsequent elemental analysis. Therefore, CoMo/SBA-15 and CoW/SBA-15 catalysts were prepared according to Brito *et al.* [69]: 2 g of SBA-15(6 and 9 nm) was stirred in a chloroform of nickel diethyldithiocarbamate or cobalt dimethyldithiocarbamate for 2 h and the solvent was removed by evaporation at room temperature. The obtained (Ni)Co/SBA-15 materials were then impregnated with an aqueous solution containing appropriate concentrations of ATM or ATT. After 2 h contact with the solution, the water was removed using a rotary evaporator at 333 K and the products were activated at 773 K for 3 h under a H₂/N₂ (H₂, 10%) gas flow at atmospheric pressure. The (Ni)Co/Mo(W) ratio was kept constant at 0.4.

Both low angle XRD patterns and N₂ isotherms (type IV isotherm) evidence that the characteristic mesoporous structure of SBA-15 is maintained after the impregnation and calcination process (Fig. 18 and Fig. 19). The decrease of the reflection intensity is a general phenomenon due to the strong absorption of X-rays by Mo(W) and/or a partial loss of the high order of the mesostructure. Moreover, a small sub-step in the isotherms at a relative pressure of about 0.45 can be clearly observed for (Ni)CoMo/SBA-15(6 nm) and CoW/SBA-15(6 nm) but not for the (Ni)CoMo/SBA-15(9 nm) and CoW/SBA-15(9 nm) catalysts which possess high normalized surface areas indicative for a low pore blocking. The two-step desorption branch for the catalysts supported on 6 nm SBA-15 is a typical feature for the in-bottle type pore system indicating the presence of strong pore blocking [70]. Moreover, the appearance of some large crystals of Mo(W)S₂ outside the pore system of SBA-15(6 and 9 nm) suggests a poor dispersion of Mo(W)S₂ which may be responsible for the low HDS activity of the actual catalysts prepared by solvent evaporation ($k = 1.5 - 6.2 \times 10^{-7} \text{ mol s}^{-1} \text{ g}^{-1}$ vs. $k = 12.0 \times 10^{-7} \text{ mol s}^{-1} \text{ g}^{-1}$ for a

commercial catalyst supported on γ -Al₂O₃, Table 4). The selectivity expressed as the ratio HYD/DDS observed for the present catalysts (Table 4) is in good agreement with catalysts supported on SBA-15 (CoMo/SBA-15 \approx 0.2, NiMo/SBA-15 \approx 0.5, CoW/SBA-15 \approx 0.3) indicating the generation of the so-called active phases. However, the solvent evaporation method seems to be not suitable for the preparation of HDS catalysts supported on SBA-15 with a high catalytic activity.

Table 4: Surface areas, normalized surface areas, initial rate constants (k) and selectivity HYD/DDS of the HDS catalysts (Co(Ni)/Mo(W) = 0.4) prepared by the evaporation method.

Catalysts	Mo/W wt. %	surface area m ² g ⁻¹	normalized surface area	initial rate constants $\times 10^{-7}$ mol s ⁻¹ g ⁻¹	HYD/DDS
SBA-15(6 nm)	-	842	1	-	-
NiMo(12)/SBA-15(6 nm)	12	548	0.76	3.5	0.46
NiMo(16)/SBA-15(6 nm)	16	434	0.74	6.2	0.30
NiMo(20)/SBA-15(6 nm)	20	409	0.67	4.6	0.43
CoMo(12)/SBA-15(6 nm)	12	497	0.77	3.2	0.22
CoMo(16)/SBA-15(6 nm)	16	428	0.74	4.2	0.19
CoMo(20)/SBA-15(6 nm)	20	369	0.76	4.7	0.27
CoW(12)/SBA-15(6 nm)	12	570	0.73	1.5	0.47
CoW(16)/SBA-15(6 nm)	16	486	0.67	2.6	0.40
CoW(20)/SBA-15(6 nm)	20	444	0.70	2.7	0.36
SBA-15(9 nm)	-	467	1	-	-
NiMo(16)/SBA-15(9 nm)	16	327	0.91	5.1	0.55
NiMo(20)/SBA-15(9 nm)	20	253	0.99	4.2	0.69
CoMo(16)/SBA-15(9 nm)	16	295	0.98	5.1	0.23
CoMo(20)/SBA-15(9 nm)	20	276	0.99	5.2	0.25
CoW(16)/SBA-15(9 nm)	16	375	1.00	4.6	0.25
CoW(20)/SBA-15(9 nm)	20	324	1.00	5.7	0.25
NiMo/ γ -Al ₂ O ₃	8	-	-	12.0	0.53

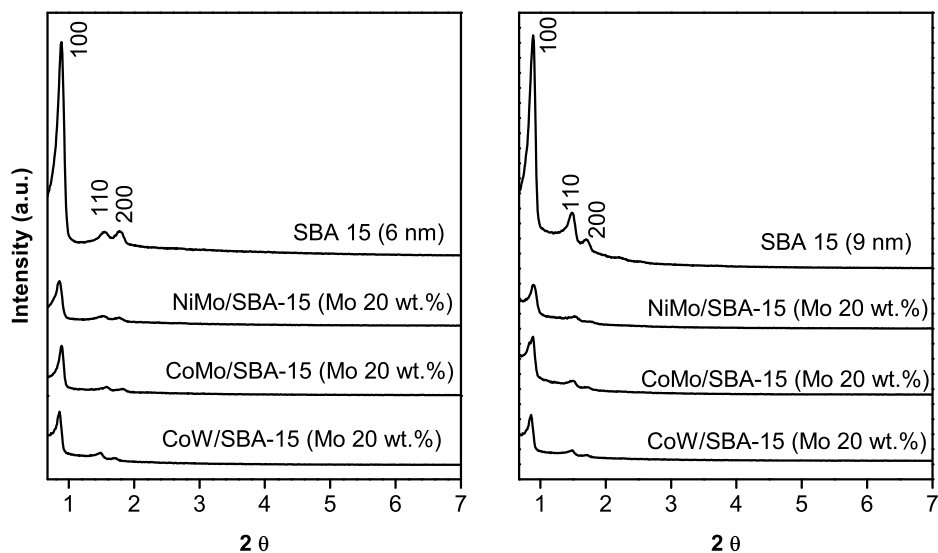


Fig. 18: Low angle XRD patterns of HDS catalysts prepared by the solvent evaporation method.

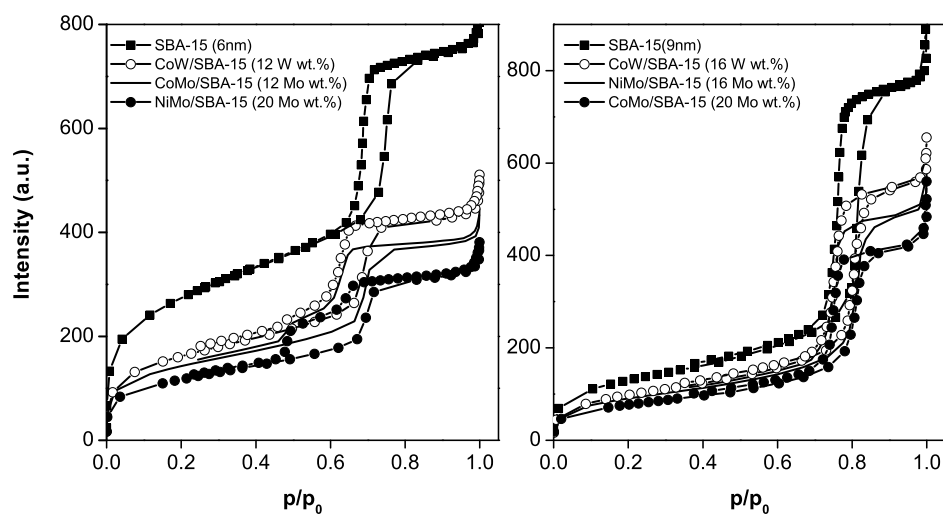


Fig. 19: Nitrogen adsorption/desorption isotherms of HDS catalysts prepared by the solvent evaporation method.

4.1.4 Ti modified SBA-15 as support for HDS catalysts

It has been reported in the literature that heteroatoms like Al, Ti or Zr incorporated in the SBA-15 support provides a better dispersion of Ni(Co) and Mo species leading consequently to higher HDS performances compared to their heteroatom-free counterparts [35–37]. As has been demonstrated in the above section, (Ni)CoMo sulfide catalysts supported on SBA-15 prepared by sulfur containing molybdenum and nickel(cobalt) compounds exhibit high HDS activity of DBT despite the presence of a pronounced large MoS₂ stacking. The effect of the Ti modification of SBA-15 onto the HDS properties is therefore of high interest.

i) Preparation of Ni(Co)Mo/SBA-15 catalysts

Ti-SBA-15 was synthesized according to [35] and the Ti concentration was kept at 13 wt.%. Typically, 2 g of Ti-SBA-15 was stirred for 4 h in 100 mL of saturated nickel diethyldithiocarbamate (NiDETC) or cobalt dimethyldithiocarbamate(CoDMTC) chloroform solutions. Afterwards, the solid was removed by filtration and the obtained products NiDETC/SBA-15 or CoDMTC/SBA-15 were dried under vacuum over night. The dried products were then stirred in 150 mL of saturated aqueous solutions of ATM at 298 K. After 4 h stirring the products were filtered without washing and then activated under a H₂/N₂ (H₂ = 10 %) gas flow at 773 K. The obtained catalysts are designed according to the metal loading, e.g. Ni(Co)(X)Mo(Y)/Ti-SBA-15 means the catalyst with X wt.% Ni(Co) loading and Y wt.% Mo loading.

ii) Results and Discussion

Fig. 20 depicts XRD patterns at low diffraction angles in the 2θ range from 0.65 to 6°. Typical diffraction lines of mesoporous SBA-15 with $p6mm$ hexagonal symmetry are observed for all samples. The incorporation of the metal sulfides results in a significant decrease of the reflection intensities. Particularly for CoMo/Ti-SBA-15, only the intense (100) reflection can be seen and the two weak diffraction peaks (110) and (200) are disappeared. This result confirms the findings of the N₂ physisorption measurements (not shown): the mesoporous structure is prevented after the impregnation of Ti-SBA-15 with Ni(Co) and Mo sulfide. The intensity loss of the diffraction peaks indicates some loss

in the long-range periodicity order of the Ti-SBA-15 sample. The crystal size of MoS_2 determined for CoMo/Ti-SBA ($d = 3.3$ nm) is apparently smaller than the average MoS_2 size of CoMo sulfided catalysts supported on pure SBA-15 materials ($d = 4.4$ nm) (see Fig. 21). In contrast, no improved MoS_2 dispersion can be found for NiMo/Ti-SBA-15 ($d = 4.3$ nm) compared to the NiMo/SBA-15 catalyst ($d = 4.3$ nm). The change of the MoS_2 morphology and the related HDS activity of DBT will be investigated in a further study.

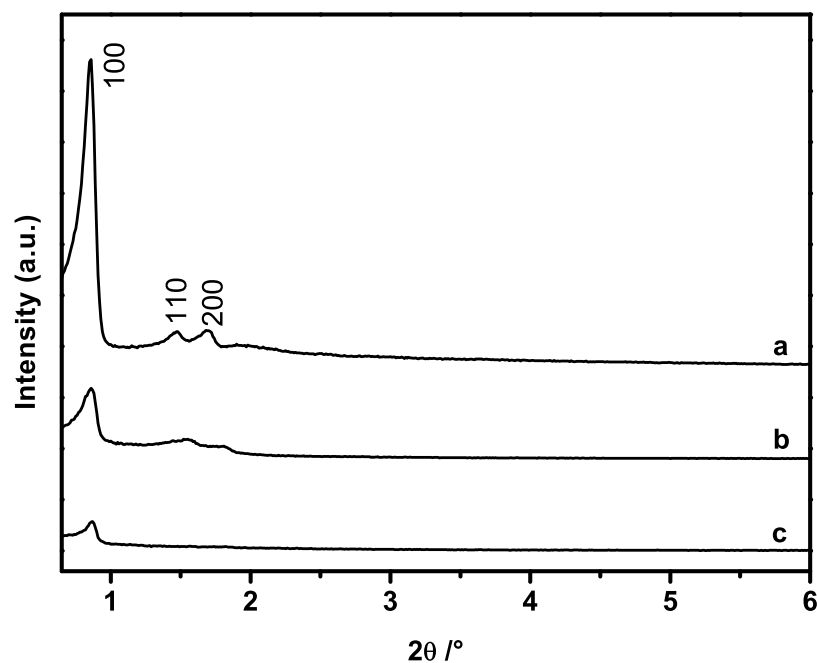


Fig. 20: XRD patterns of a: Ti-SBA-15, b: Ni(1.5)Mo(15)/Ti-SBA-15 and c: Co(4.0)Mo(20)/Ti-SBA-15

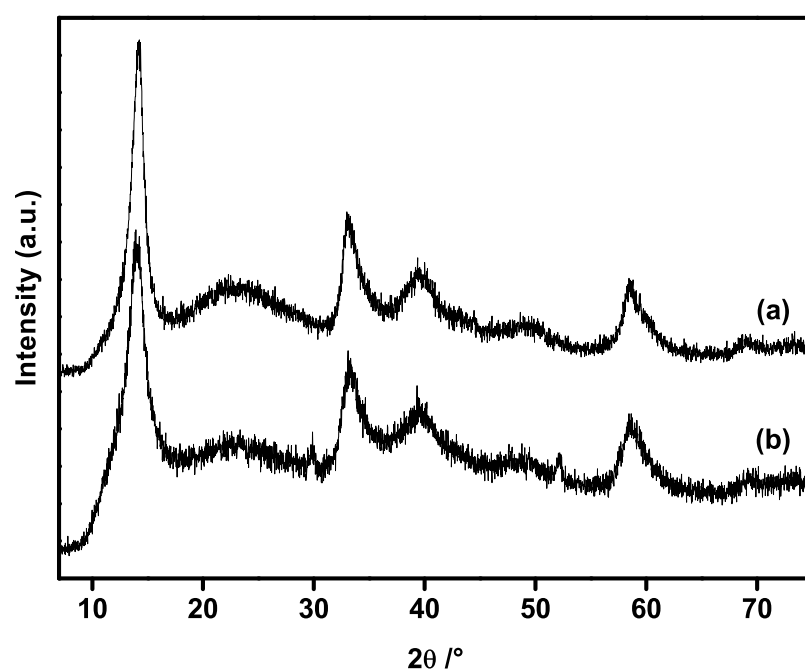


Fig. 21: Wide angle XRD patterns of (a) Ni(1.5)Mo(15)/Ti-SBA-15 with $d = \text{ca. } 4.3 \text{ nm}$ and (b) Co(4.0)Mo(20)/Ti-SBA-15 with $d = \text{ca. } 3.3 \text{ nm}$.

4.2 SBA-15 as support for MoO₃ catalysts

MoO₃ was successfully dispersed inside the pore system of SBA-15 (HAADF) using ammonium heptamolybdate (AHM) as source. The N₂ physisorption measurements evidence that the pore blocking is low for Mo loadings up to 13 wt.% Mo. The nano-sized MoO₃ particles reveal a remarkable size dependent intensity loss in the Raman spectra. A broad resonance at about 950 cm⁻¹ gives evidence for the interaction of MoO₃ particles with the silica support. Below 13 wt.% Mo loading no reflections of MoO₃ occur in the X-ray powder patterns. Interestingly, even for high MoO₃ contents the intensities of the reflections are much lower than expected for fully crystalline material. The reflection intensities of a sample containing 17 wt.% Mo are much less intense than those of a physical mixture of SBA-15 and 7 wt.% Mo. The detailed XAFS analysis performed on a sample with 8 wt.% Mo reveals that the metastable hexagonal modification of MoO₃ is formed despite the high calcination temperature of 773 K. It is highly interesting that the metastable hexagonal MoO₃ phase can even be stabilized on SBA-15 (*in-situ* EXAFS) in the temperature range from 293 to 773 K. Bulk AHM is first decomposed to an amorphous intermediate followed by the formation of ammonium tetramolybdate at about 500 K. A further increase of the temperature yields first a mixture of α - and hexagonal MoO₃ followed by a quantitative transformation to the stable orthorhombic modification at about 633 K. It is highly likely that the interaction between MoO₃ and the support is responsible for the stability of the metastable MoO₃ modification. The hex-MoO₃-SBA-15 material shows a high activity and selectivity for the propene oxidation reaction in contrast to the stable α -MoO₃ modification. More interestingly, the formation of acrylic acid was observed for the first time using hex-MoO₃-SBA-15 as catalyst without additional metal atoms like V or Nb. The stabilized structure of hexagonal MoO₃ supported on SBA-15 possesses an open channel structure similar to that of the highly active Mo₅O₁₄ or MoVNbTe catalysts. Hence, a structural complexity of molybdenum oxides is sufficient to improve functional molybdenum sites for the activation of oxygen and alkenes followed by selective oxidation of the alkenes. More detailed information can be found in the following two publications.

J Mater Sci (2008) 43:244–253
DOI 10.1007/s10853-007-2173-x

The modification of MoO₃ nanoparticles supported on mesoporous SBA-15: characterization using X-ray scattering, N₂ physisorption, transmission electron microscopy, high-angle annular darkfield technique, Raman and XAFS spectroscopy

Zhida Huang · Wolfgang Bensch · Wilfried Sigle · Peter A. van Aken · Lorenz Kienle · Tonya Vitoya · Hartwig Modrow · Thorsten Ressler

Received: 15 March 2007 / Accepted: 17 September 2007 / Published online: 17 October 2007
© Springer Science+Business Media, LLC 2007

Abstract MoO₃ was dispersed onto mesoporous SBA-15 by using ammonium heptamolybdate as MoO₃ source. The formation of MoO₃ was carried out by heating the loaded material to 500 °C for 3 h in air. Below 13 wt% Mo loading, no reflections of MoO₃ occur in the X-ray powder patterns and even for high MoO₃ contents, the intensities of the reflections are much lower than expected for fully crystalline material. A detailed XAFS analysis reveals that at low Mo contents, the metastable hexagonal modification of MoO₃ is formed despite the high calcination temperature of 500 °C. It is highly likely that the nanosize of the particles and the interaction between MoO₃ and SBA-15 stabilize the metastable modification of the material. Nitrogen physisorption experiments show the typical type-IV isotherms indicating that the mesoporosity of the materials is preserved despite the large amount of MoO₃.

Transmission electron micrographs demonstrate the presence of MoO₃ inside the SBA-15 support. The Raman spectra display a remarkable size-dependent intensity loss and several features give evidences for a bond formation between nano-sized MoO₃ particles and the silica support. Moreover, the spectroscopic details suggest the formation of (MoO₃)_n oligomers.

Introduction

In the past few years, periodic silica-based mesoporous materials such as MCM-41 and SBA-15 were used as templates for the syntheses of shape-selective new materials. The mesoporous materials are synthesized via the polymerization of silica around periodic cationic amphiphiles (MCM-41) and neutral block copolymer (SBA-15). SBA-15 possesses well-ordered hexagonal arrays of mesopores with pore diameters between 3 and 30 nm [1, 2] and SBA-15 possesses thicker walls (31–64 Å) compared to MCM-41. Therefore, SBA-15 exhibits a higher thermal stability, being claimed to be stable for at least 48 h in boiling water [1]. Using SBA-15 with the narrow pore diameter distribution as a template for the synthesis of nanoparticles, products are obtained reflecting the diameters of the pores and maximal particle lengths in accordance with the channel lengths of the template material. Such incorporated nanoparticles may have interesting optical, magnetic, and catalytic properties. In addition to the studies of the formation of metal nanoparticles and nanowires, such as Pt [3–5], Pd [6–9], Au [3–5, 10, 11], Ag [3], and Ti [12], the formation of binary nanomaterials such as PbS [13], CdS [14], TiN [15], and GaN [16] within the nanoscale channels of these

Z. Huang · W. Bensch (✉)
Institut für Anorganische Chemie, University of Kiel,
Olshausenstraße 40-60, Kiel 24098, Germany
e-mail: wbensch@ac.uni-kiel.de

W. Sigle · P. A. van Aken
Max-Planck-Institut für Metallforschung, Heisenbergstr. 3,
70506 Stuttgart, Germany

L. Kienle
Max-Planck-Institut für Festkörperforschung, Heisenbergstr. 1,
70506 Stuttgart, Germany

T. Vitoya · H. Modrow
Physikalisches Institut der Universität Bonn, Nussallee 12,
53115 Bonn, Germany

T. Ressler
Institut für Chemie, Fachgruppe Anorganische und Analytische
Chemie, TU Berlin, Straße des 17. Juni 135, 10623 Berlin,
Germany

mesoporous materials have been explored. More recently, highly ordered quantum wires of $Zn_{1-x}Mn_xS$ [17] and $Cd_{1-x}Mn_xS$ [18] have been successfully synthesized within the mesopores of SBA-15.

Molybdenum-based catalysts have been investigated intensively [19–24] because of their importance in the technical processes, such as propene metathesis [25, 26], propene oxidation [27, 28], methanol oxidation [29], ethanol oxidative photochemical reaction, and most importantly in hydrodesulfurization (HDS) processes, which represent one of the largest groups of catalytic steps in petroleum and petrochemical reactions. Recently, SBA-15-supported MoO_3 materials were used as an intermediate for the preparation of MoS_2 catalysts. Different synthesis strategies were applied like thermal treatment of SBA-15 impregnated with ammonium heptamolybdate (AHM) [30], thermal spreading of MoO_3 [31], or sonochemical decomposition of $Mo(CO)_6$ in organic solvents [32]. The main aim of these investigations was the preparation of active HDS catalysts. The formation of MoO_3 and especially the structures of the supported oxide were not investigated. The MoO_3 species are formed within a confined space and the highly interesting question arises whether a metastable modification of the oxide is formed depending on particle sizes as observed for other oxides like TiO_2 . The thermal decomposition of bulk AHM in different gas atmospheres was recently investigated by in-situ X-ray absorption spectroscopy (XAFS) and in-situ X-ray diffraction [33]. Under static condition AHM is decomposed first to an amorphous phase followed by the formation of ammonium tetramolybdate (ATM) at about 230 °C. With increasing temperature, first a mixture of α - and hexagonal MoO_3 is formed and finally pure orthorhombic α - MoO_3 is observed at about 360 °C. In the present study, AHM was decomposed to prepare MoO_3 species within the pores of SBA-15. Several samples containing different amounts of MoO_3 are analyzed and characterized applying various analytical methods including Raman spectroscopy, N_2 physisorption, transmission electron microscopy (TEM), high-angle annular darkfield (HAADF) technique combined with energy-dispersive X-ray analysis (EDXS), X-ray scattering experiments, and XAFS. From the results of these studies, a complete picture of the structures of $MoO_3/SBA-15$ composite materials is obtained.

Experimental section

Sample preparation

Synthesis of pristine mesoporous SBA-15

About 8 g of poly(ethylene glycol)-block-poly(propylene glycol)-block-poly(ethylene glycol) triblock copolymer

(Aldrich, pluronic, P-123) was dissolved in 240 g of water and 28.6 g of concentrated HCl at 30 °C on a water bath. After dropwise addition of 16 g of tetraethyl orthosilicate (TEOS), the reaction mixture was stirred for 24 h at 30 °C. The resulting gel was transferred into a Teflon bottle and heated to 80 °C for 24 h to obtain SBA-15 with 6 nm pores. The resulting white powder was filtered and washed with deionized water, and the surfactant was removed by Soxhlet extraction at 78 °C with a mixture of 970 mL of ethanol and 30 mL of concentrated hydrochloric acid. After washing with ethanol, the white powder was dried at RT for about 1 week.

Synthesis of $MoO_3/SBA-15$

Typically, 1 g of SBA-15 was stirred in aqueous solutions of ammonium heptamolybdate $(NH_4)_6Mo_7O_{24} \cdot 4H_2O$ (AHM) with different concentrations at pH 7–8. After stirring at room temperature for 18 h, the products were filtered without washing. The impregnated SBA-15 was calcined at 500 °C for 3 h in air to obtain MoO_3 . This calcination temperature is much higher than the usual thermal decomposition temperature of AHM (ca. 350 °C) [34], at which MoO_3 is formed in air. At lower temperatures, AHM is found not completely to be decomposed to MoO_3 , which indicates that AHM is located in the pores and not on the outer surface of the material. The silica walls and small pore diameters can impede the removal of the decomposition products of AHM, such as NH_3 and H_2O , and consequently a higher formation temperature is required. Materials containing different Mo concentrations were prepared using appropriate concentrations of AHM, i.e., 0.03, 0.06, and 0.09 M solutions. The synthesized products are abbreviated as Mo/SBA-15(A), Mo/SBA-15(B), and Mo/SBA-15(C) with Mo loadings of 8, 13, and 17 wt%, respectively, and were stored in dried air.

Sample characterization

Powder X-ray diffraction (XRD) patterns were obtained on a Bruker D8 Advance diffractometer at room temperature using Cu K α radiation generated at 40 kV and 30 mA. Fourier transform (FT) Raman spectra were recorded with a Bruker FT-106 Raman module, equipped with a Ge detector cooled by liquid nitrogen, and connected to a Bruker FT-IR 66 interferometer and a continuous wave diode-pumped Nd:YAG Laser with a radiation wavelength of 1,064 nm (9398.5 cm^{-1}). The laser power was set to 300 mW and the spectral resolution was 2 cm^{-1} . Nitrogen adsorption measurements were carried out at 77 K on a Sorptomatic 1990 adsorption analyzer. Before the

measurements, the samples were outgassed for at least 24 h at 120 °C. The BET surface areas were calculated from $p/p_0 = 0.03$ – 0.3 in the adsorption branch; the BJH pore size distributions were calculated from the desorption branch.

For TEM, dried SBA-15 and MoO₃/SBA-15 powders were sonicated in dichloromethane for several seconds, dropped on the TEM grids, and dried on carbon-film-coated copper grids (Ted Pella) in air. Transmission electron microscopy microphotographs were obtained on a JEOL JEM-2000 FX electron microscope operating at 200 kV. HAADF images were obtained in a VG HB501UX dedicated scanning transmission electron microscope. In this imaging mode, the brightness is proportional to Z^n , where Z denotes the atomic number and $n \approx 1.7$. This allows distinguishing Mo from the SBA-15 support. The Mo-content was determined by EDXS with a spatial resolution of about 1 nm.

The XAS experiment was performed at the INE beamline at the ANKA 2.5 GeV synchrotron radiation facility. For details about the instrumentation at this beamline see Ref. [35]. For energy monochromatization, a Lemonnier-type [36] double-crystal monochromator equipped with Ge(422) crystals was employed, leading to a minimum energy step width of 0.2 eV. For calibration, photon energy of 20 keV was assigned to the first inflection point of the K-edge spectrum of a molybdenum foil. The absorption spectra of the powder samples: MoO₃/SBA-15 with 8 wt% molybdenum loading and MoO₃ reference were recorded at the Mo–K edge (20 keV) in transmission mode between 19.799 keV and 20.853 keV with energy steps of 0.5 eV and 2 s integration time per step.

X-ray absorption fine structure (XAFS) analysis was performed using the software WinXAS v3.1 [37]. Background subtraction and normalization were carried out by fitting linear polynomials to the pre-edge and the post-edge region of the absorption spectra, respectively. The extended X-ray absorption fine structure (EXAFS) $\chi(k)$ was extracted by using cubic splines to obtain a smooth atomic background, $m_0(k)$, where k denotes a reciprocal space vector. The pseudo-radial distribution function $\text{FT}(\chi(k)*k^3)$ was calculated by Fourier transforming the k^3 -weighted experimental $\chi(k)$ function, multiplied by a Bessel window, into reciprocal space. EXAFS data analysis was performed using theoretical backscattering phases and amplitudes calculated with the ab-initio multiple-scattering code FEFF7 [38]. Single scattering and multiple scattering paths in the α -MoO₃ model structure were calculated up to 5.0 Å with a lower limit of 2.0% in amplitude with respect to the strongest backscattering path. EXAFS refinements were performed in reciprocal space simultaneously to magnitude and imaginary part of a Fourier-transformed k^3 -weighted and k^1 -weighted experimental $\chi(k)$ using the standard EXAFS formula [39]. Structural parameters that are

determined by a least-squares EXAFS refinement of a MoO₃ model structure to the experimental spectra are (i) an overall shift of E_0 , (ii) Debye-Waller factors for single-scattering paths, and (iii) distances of single-scattering paths. Coordination numbers (CN) and S_0^2 were kept invariant in the refinement.

Results and discussion

Powder X-ray diffraction

Figure 1 shows the X-ray powder diffraction patterns of MoO₃/SBA-15 displaying the three characteristic reflections (100), (110), and (200) of hexagonal mesoporous SBA-15 with space group $P6mm$. The powder diffraction patterns indicate that the primary structure of SBA-15 consists of well-ordered channels, which are maintained after the formation of MoO₃ nanoparticles inside the channels. In addition, the phase cancellation between the pore walls and the guest species MoO₃ leads to a decrease of the intensity of Bragg reflections, which is more pronounced for higher MoO₃ contents. This phenomenon is well known [17, 40] and was also observed in [30].

In Fig. 2, wide-angle XRD patterns of the MoO₃/SBA-15 samples along with a diffraction pattern of a physical mixture of MoO₃ and SBA-15 are displayed. Below 13 wt% Mo, no reflections of crystalline MoO₃ occur in the patterns and only a broad feature caused by SBA-15 is observed, indicating that the crystallite size of the MoO₃ particles is below the coherence length of X-ray scattering of roughly 5 nm (see Fig. 2, trace (a) with 8 wt% Mo as an example). Some weak reflections of α -MoO₃ are visible at a loading of 13 wt% Mo, and the reflection positions agree

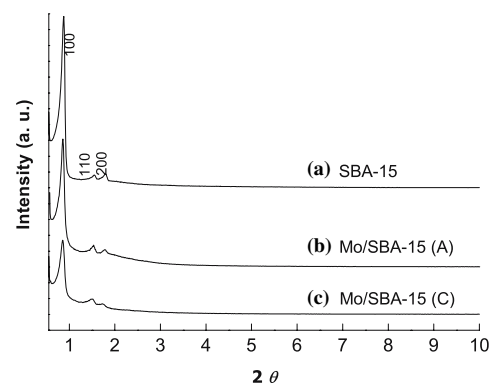


Fig. 1 XRD patterns of (a) SBA-15, (b) Mo/SBA-15(A), and (c) Mo/SBA-15(C) with Mo loadings of 8 wt% and 17 wt% respectively

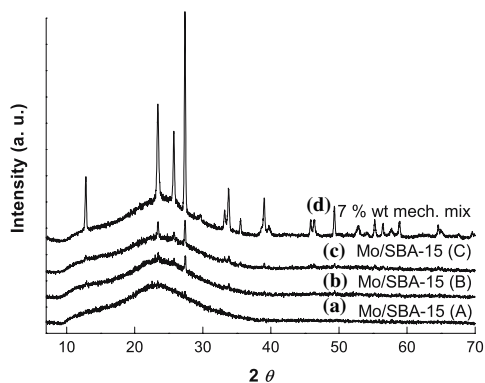


Fig. 2 XRD patterns of (a) Mo/SBA-15(A) (8 wt% Mo), (b) Mo/SBA-15(B) (13 wt% Mo), (c) Mo/SBA-15(C) (17 wt% Mo), and (d) of a physical mixture (7 wt% Mo)

well with those of bulk MoO_3 . For higher loading than 13 wt% Mo, the reflections of $\alpha\text{-MoO}_3$ become more intense. But even for 17 wt% Mo in the SBA-15 pores, the reflection intensity is much lower compared to the data of the mechanical mixture which has only 7 wt% Mo. The average particle size of MoO_3 can be estimated from the peak width using the Scherrer formula. The average crystallite size estimated from the reflection at $2\theta = 23.4^\circ$ is about 30 nm for high Mo loading of 17 wt%. Comparing the size of MoO_3 with the pore diameters of the SBA-15 material suggests that the MoO_3 crystallites are located partly outside the channels of SBA-15. The amount of crystalline dispersed MoO_3 can be estimated from the intensity of the XRD reflection located at $2\theta = 23.4^\circ$. Since the intensity of Mo/SBA-15(C) with 17 wt% Mo is nearly identical with that of a mechanical mixture of 2.5 wt% Mo (not shown), one may estimate that the amount of nano-crystalline MoO_3 for this sample is close to 14.5 wt% Mo. Indeed, the maximal loading achieved can be evaluated to $1.9 \mu\text{mol m}^{-2}$ (surface area of SBA-15 is about $850 \text{ m}^2 \text{ g}^{-1}$) for a fully-dispersed MoO_3 , which is in good agreement

with the value determined by Blanchard et al. ($2 \mu\text{mol m}^{-2}$) for SBA-15 support [31]. The results of the XRD investigations clearly indicate that the MoO_3 species are finely dispersed and a similar observation was made by Dhar et al. [30].

Nitrogen physisorption

Figure 3 displays the N_2 adsorption–desorption isotherms (at 77 K), the pore-size distribution of SBA-15 and the MoO_3 -impregnated SBA-15 materials with different Mo concentrations. The numerical data are listed in Table 1. For all materials, a type-IV isotherm is observed, which is the typical hysteresis loop of mesoporous materials [41], indicating that the incorporation of Mo species does not destroy the structure of mesoporous SBA-15. The pore sizes were calculated from the desorption branch of the isotherm using the Barrett-Joyner-Halenda (BJH) model, which is an appropriate method for determining changes in the pore-size distribution [17, 18, 42] and the Barrett-Emmett-Teller (BET) equation was applied for calculation of specific surface areas. The isotherms have the following characteristic features: (1) the capillary condensation step, which is caused by the decrease of the pore sizes, typically at the relative pressure $p/p_0 = 0.6\text{--}0.7$ for pristine SBA-15, shifts to lower relative pressure $p/p_0 = 0.4\text{--}0.6$ after introduction of MoO_3 particles into the pores (Fig. 3a); (2) the amount of adsorbed nitrogen decreased significantly, which is associated with the smaller specific surface area; (3) the pore volumes decrease with increasing amount of impregnated Mo in SBA-15 (Table 1) and the mean pore diameter (Fig. 3b) decreases as evidenced by the slight shift of the main peak in pore-size distribution curves to smaller values; (4) adsorption of intra-wall micropores at low relative pressures decreases with the increasing loading of MoO_3 ; (5) a small sub-step at the relative pressure at about 0.45 can be observed.

From the isotherms, it can be concluded that the mesoporosity of the support is still preserved after the

Fig. 3 Nitrogen absorption/desorption isotherms of Mo/SBA-15(A) (8 wt% Mo), Mo/SBA-15(C) (17 wt% Mo) (a), and BJH pore-size distribution (b)

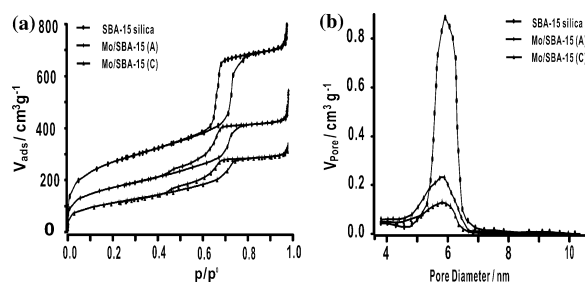


Table 1 BET surface area, mean pore diameter D , and wall thickness t (calculated from $t = a - D$ [18], a = cell parameter), for the pristine SBA-15 silica and the MoO₃/SBA-15 host–guest compounds

Sample	Mo loading wt%	Mesopore/micropore volume (cm ³ g ⁻¹)		BET surface area (m ² g ⁻¹)		Mean pore diameter D (nm)	Wall thickness t (nm)
		Normalized		Normalized			
SBA-15	0	1.08/0.17	1	920	1	5.96	4.31
Mo/SBA-15(A)	8	0.65/0.13	0.68/0.86	597	0.74	5.34	4.93
Mo/SBA-15(B)	13	0.55/0.11	0.63/0.80	505	0.68	5.11	5.16
Mo/SBA-15(C)	17	0.45/0.08	0.56/0.61	397	0.58	5.02	5.25

Normalized(X) = $X_{\text{MoO}_3} / ((1 - y)X_{\text{SBA-15}})$, where X is specific surface area or pore volume and y is weight fraction of MoO₃

incorporation of MoO₃ particles into the SBA-15 materials. The important decrease in pore volume (mesopores and micropores) and the reduced mean pore sizes (see Table 1) indicates the filling of both the mesopores and the micropores by MoO₃ particles. The two-step desorption branch [43] and the decrease in pore volume might be attributed to the presence of a pore-blocking effect by MoO₃, because the formation of MoO₃ particles inside the pores of SBA-15 would not significantly affect the pore volume due to the high density of MoO₃ (4,700 kg cm⁻³). This blocking effect becomes more pronounced with increasing Mo loadings.

Transmission electron microscopy

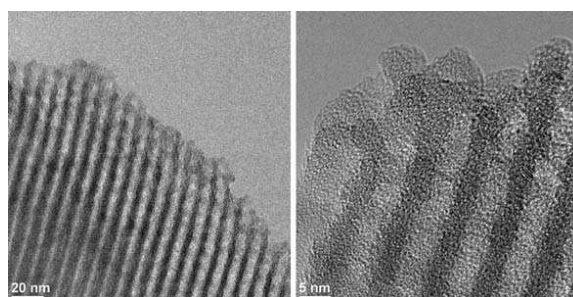
Transmission electron microscopy was performed to analyze the microstructure of the samples. For all samples with different Mo loadings, the hexagonally ordered pore structure of the SBA-15 host was maintained after inclusion of MoO₃ and calcination. This is exemplified by the bright-field images of Fig. 4 (loading: 17 wt% Mo, two distinct magnifications), which were recorded perpendicular to the channel axes. The presence of MoO₃ inside the pores can be demonstrated by a combined approach of HAADF and EDXS. The HAADF images of Fig. 5 (17 wt% Mo) were recorded in two distinct orientations of

the channels. For the image recorded perpendicular to the channel axes (Fig. 5a), randomly distributed bright spots are preferably aligned along the channel axes. In case of images along the channels axis (i.e., [001]) (Fig. 5b), bright spots fill the space of the open SBA-15 pores. Figure 6 shows EDXS spectra acquired from the bright spots (a) and from darker areas (b). It is obvious that the intensity of the Mo-L peak is significantly higher at the position of the bright spots. Occasionally, the locations of the bright spots do not fit with the periodicity of the host. The most probable interpretation here is to assume the presence of MoO₃-nanoparticles on the surface of the host. But it appears that most MoO₃-nanoparticles are located inside the SBA-15 pores.

Raman spectroscopy

Raman spectroscopy is one of the effective methods to probe crystalline and amorphous nanoscale oxides [23, 24]. Raman spectra of the impregnated samples before calcination are displayed in Fig. 7, and the characteristic bands of the [Mo₇O₂₄]⁶⁻ anion are clearly visible for the sample with 8 wt% Mo. The strong band at 943 cm⁻¹ is due to the symmetric stretching of the short Mo–O terminal bonds of [Mo₇O₂₄]⁶⁻ along with a weak and medium band at 898 cm⁻¹ [22]. The bending vibration at 362 cm⁻¹ and

Fig. 4 TEM images with different magnifications recorded for the sample with 17 wt% Mo



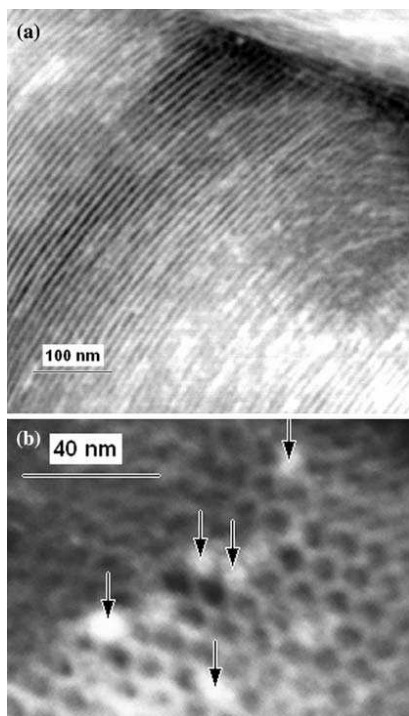


Fig. 5 HAADF images of Mo/SBA-15 (17 wt% Mo) in an orientation (a) perpendicular to and (b) along the channel axes. MoO₃-nanoparticles show bright contrast as indicated by the arrows in (b)

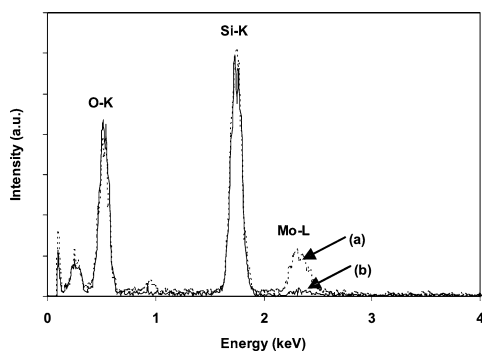


Fig. 6 Energy-dispersive X-ray spectra of (a) MoO₃ particle and (b) SBA-15

deformation band at 320 cm⁻¹ of the terminal Mo=O groups are also observed. The intensity of these bands increases with the amount of incorporated AHM.

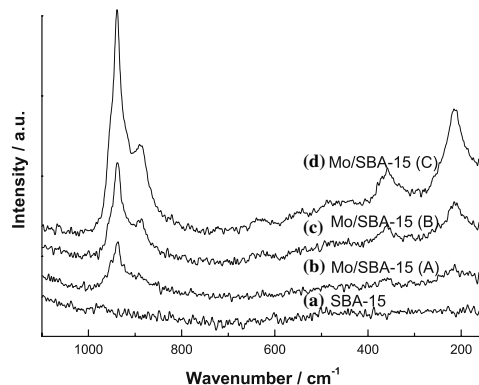


Fig. 7 Raman spectra of (a) SBA-15, (b) Mo/SBA-15(A) (8 wt% Mo), (c) Mo/SBA-15(B) (13 wt% Mo), and (d) Mo/SBA-15(C) (17 wt% Mo) before calcination at 500 °C

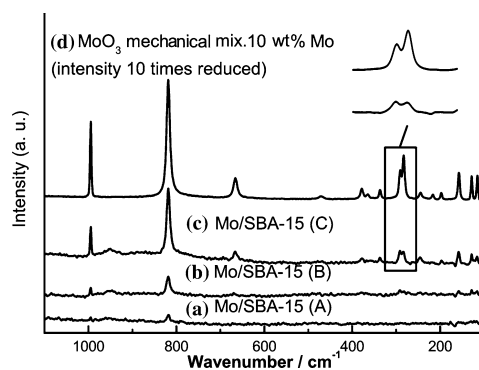


Fig. 8 Raman spectra of (a) Mo/SBA-15(A) (8 wt% Mo), (b) Mo/SBA-15(B) (13 wt% Mo), (c) Mo/SBA-15(C) (17 wt% Mo) after calcination, and (d) of a mechanical mixture (10 wt% Mo)

In the Raman spectra of calcined Mo/SBA-15 along with a spectrum of the mechanical mixture (Fig. 8), the characteristic features of bulk MoO₃ are seen. Considering only Mo–O bonds up to 2 Å, MoO₃ chains are directed along the crystallographic *c* axis by corner sharing of MoO₄ tetrahedra [44]. The Raman spectrum of MoO₃ between 82 and 995 cm⁻¹ was investigated by Py and Maschke [45], who carried out a study on single crystals and performed valence force-field calculations. The band at 994 cm⁻¹ was assigned to the symmetric stretching mode of the terminal Mo=O groups and the signals at 819 and 665 cm⁻¹ to the vibrations of the Mo–O–Mo bridge. The doublet at 290–280 cm⁻¹ corresponds to the two wagging modes of the terminal Mo=O groups.

In the spectrum of Mo/SBA-15(A) with 8 wt% Mo, only two bands are visible at 819 and 994 cm^{-1} as weak signals. For low loadings, the predominant silica-supported molybdenum species were observed to be isolated molybdate tetrahedra [21]. However, no bands at 988 and 620 cm^{-1} characteristic of MoO_4^{2-} were detected in our sample, indicating that MoO_3 should be formed as the majority species under our experimental conditions. At high loadings, the observed wave numbers for $\text{MoO}_3/\text{SBA-15}$ materials are similar to that found for the physical mixture. However, some features in the Raman spectra should be highlighted. The Raman spectra of $\text{MoO}_3/\text{SBA-15}$ materials exhibit a significant intensity loss compared to the physical mixture with the same Mo content. The intensity reduction may be explained by a reduced effective scattering volume of dispersed MoO_3 particles. Such a size-dependent intensity change was also reported by Mestl et al. [20]. Furthermore, the spectra show a change of the relative intensity of the MoO_3 characteristic modes at 819 and 994 cm^{-1} , which may be associated with the weak interaction between the highly distorted small MoO_3 particles and the SBA-15 support. The typical intensity ratio I_{994}/I_{819} for Mo/SBA-15(B) and Mo/SBA-15(C) is 0.45, which is smaller than that of the mechanical mixture of 0.64. An identical feature was observed by Braun et al. [19] and Jeziorowski et al. [46], who prepared the silica supported MoO_3 by thermal spreading ($I_{994}/I_{819} = 0.49$) and the impregnation method ($I_{994}/I_{819} = 0.46$), respectively. In addition, an interesting phenomenon in the Raman spectra is the change in relative intensity of the two wagging modes at 290 (B_{2g}) and 280 cm^{-1} (B_{3g}). In the single crystal and the physical mixture spectra, the B_{3g} wagging mode has only 2/3 of the intensity of the B_{2g} mode. For all the $\text{MoO}_3/\text{SBA-15}$ samples, the B_{3g} wagging mode is as intense as the B_{2g} signal and the two modes are hardly resolved. This observation is consistent with a phenomenon, which has been discussed by Braun et al. [19] in the spectra of $\text{Mo}/\text{Al}_2\text{O}_3$ and Mo/SiO_2 sample. The two wagging modes of the terminal $\text{Mo}=\text{O}$ groups are parallelly polarized to the direction of the chain of the tetrahedral MoO_4 units, i.e., directed along the c -axis. Therefore, the change in the intensity ratio for this doublet may be attributed to the distortions along the MoO_4 chains. Finally, a weak shoulder appears at about 953 cm^{-1} corresponding to the $\text{Mo}=\text{O}$ vibration of a polymeric molybdate species interacting with the support [24].

XAFS

The XRD patterns confirm the formation of $\alpha\text{-MoO}_3$ at high Mo-loadings, and Raman data indicate the interaction of size-reduced MoO_3 with the silica support. However, the

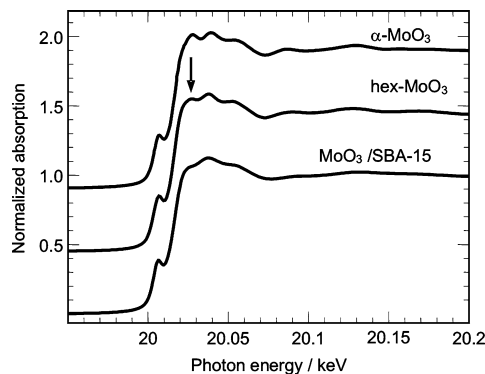


Fig. 9 Mo-K edge XANES spectra of $\text{MoO}_3/\text{SBA-15}$ (8 wt% Mo), $\alpha\text{-MoO}_3$, and hex- MoO_3

modification of $\text{MoO}_3/\text{SBA-15}$ at low concentration of Mo stayed unknown and was furthermore examined by XAFS. The Mo-K edge XANES spectra of $\text{MoO}_3/\text{SBA-15(A)}$ (8 wt% Mo), $\alpha\text{-MoO}_3$, and hex- MoO_3 are depicted in Fig. 9. The similarity of the local structure around the Mo atoms in $\alpha\text{-MoO}_3$ and hex- MoO_3 (Table 2) is readily visible in a very similar near-edge structure. However, in particular the feature at ~ 20.03 keV (arrow in Fig. 9) appears to be more reduced in the spectrum of hex- MoO_3 than in that of $\alpha\text{-MoO}_3$. Compared to the references, the XANES spectrum of $\text{MoO}_3/\text{SBA-15}$ exhibits a similar overall shape. While the number of peaks in the XANES spectrum of $\text{MoO}_3/\text{SBA-15}$ is the same as in those of $\alpha\text{-MoO}_3$ and hex- MoO_3 , the amplitude of the peaks is significantly reduced. This holds particularly for the peak at ~ 20.03 keV. In total, the Mo-K edge spectra of $\text{MoO}_3/\text{SBA-15}$ seem to correspond to a local structure similar to that of $\alpha\text{-MoO}_3$ and/or hex- MoO_3 . The reduced amplitude of XANES can be attributed to a considerably reduced ordering of small particles.

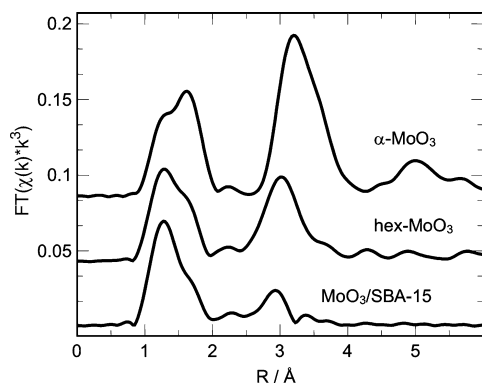
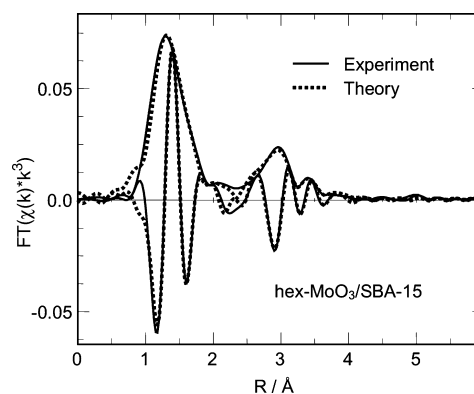
The Fourier-transformed XAFS $\chi(k)*k^3$ of $\text{MoO}_3/\text{SBA-15(A)}$ (8 wt% Mo), $\alpha\text{-MoO}_3$, and hex- MoO_3 are shown in Fig. 10. Compared to the XANES spectrum, more distinct differences can be seen in the FT($\chi(k)*k^3$) of $\alpha\text{-MoO}_3$ and hex- MoO_3 . Particularly the shape of the peaks between 1.0 Å and 2.0 Å (not phase-shift corrected) that correspond to Mo-O distances and the position of the peak at ~ 3 Å that corresponds to Mo-Mo distances differ significantly. Compared to the references, the overall shape of the FT($\chi(k)*k^3$) of $\text{MoO}_3/\text{SBA-15}$ appears to resemble more closely to that of hex- MoO_3 than to that of $\alpha\text{-MoO}_3$.

For a more detailed analysis of the XAFS data, the theoretical FT($\chi(k)*k^3$) calculated for an $\alpha\text{-MoO}_3$ model structure was refined using the experimental spectra of

Table 2 Type and number (N) of atoms at distance R from the Mo atoms in α -MoO₃ and hex-MoO₃ model systems compared to experimental distances and EXAFS Debye-Waller factors

Type	N	Model α -MoO ₃	Model hex-MoO ₃	hex-MoO ₃		MoO ₃ -SBA-15	
		R (Å)	R (Å)	R (Å)	σ^2 (Å ²)	R (Å)	σ^2 (Å ²)
Mo–O	1	1.67	1.68	1.68	0.0010	1.68	0.0010
Mo–O	1	1.73	1.73	1.75	0.0035	1.75	0.0030
Mo–O	2	1.95	1.97	1.97	0.0035	1.99	0.0065
Mo–O	1	2.25	2.20	2.21	0.0012	2.23	0.0030
Mo–O	1	2.33	2.39	2.38	0.0026	2.39	0.0021
Mo–Mo	2	3.44	3.31	3.33	0.0050	3.30	0.0080
Mo–Mo	2	3.70	3.73	3.70	0.0026	3.79	0.0083
Mo–Mo	2	3.96	4.03	3.95	0.0031	4.00	0.0101

Experimental parameters were obtained from a refinement of a α -MoO₃ model structure to the experimental Mo–K edge XAFS $\chi(k)$ of hex-MoO₃ and MoO₃/SBA-15 (8 wt% Mo) (k -range from 3.1 Å⁻¹ to 14.3 Å⁻¹, R range from 0.9 Å to 4.0 Å, E_0 (MoO₃/SBA-15) = -1.5 eV, E_0 (hex-MoO₃) = -1.8 eV, residual = 6.9, $N_{\text{ind}} = 24$, $N_{\text{free}} = 15$). The uncertainty in the distances amounts to about 0.03 Å

**Fig. 10** Fourier transformed Mo-K edge XAFS $\chi(k)*k^3$ (not corrected for phase-shifts) of MoO₃-SBA-15 (8 wt% Mo), α -MoO₃, and hex-MoO₃**Fig. 11** Experimental and theoretical Fourier transformed Mo-K edge XAFS $\chi(k)*k^3$ (not corrected for phase-shifts) of MoO₃-SBA-15 (8 wt% Mo)

MoO₃-SBA-15 and hex-MoO₃ (Fig. 11). Therefore, the most prominent Mo–O and Mo–Mo single scattering paths were included. The refinement of the model structure to the spectrum of MoO₃/SBA-15 results in a very good agreement between the experimental and theoretical spectrum (Fig. 11). The structural parameters obtained are given in Table 2. Besides small differences in the local structure around the Mo atoms in α -MoO₃ and hex-MoO₃, a significantly shortened Mo–Mo distance of 3.3 Å exists in hex-MoO₃ compared to 3.4 Å in α -MoO₃. This short Mo–Mo distances account for the shift in peaks at higher distances as visible in the FT($\chi(k)*k^3$) of the two references. Similar to hex-MoO₃, MoO₃/SBA-15 exhibits a short Mo–Mo distance at \sim 3.3 Å and a slightly

prolonged Mo–O distance at \sim 2.4 Å. The good agreement between the structural parameters of MoO₃/SBA-15 and hex-MoO₃ indeed indicates the presence of hex-MoO₃ inside the pore structure of SBA-15. The strongly reduced amplitude in the FT($\chi(k)*k^3$) at higher distances may be caused by very small particles or a predominantly two-dimensional structure of the hexagonal MoO₃ modification in SBA-15. Treating AHM in air at 500 °C results in the formation of α -MoO₃, as previously reported [33], and hex-MoO₃ is formed as an intermediate phase at \sim 350 °C. However, hex-MoO₃ transforms upon further heating into the more stable α -MoO₃ modification. For the materials with low Mo-loading studied here, the metastable hexagonal modification of MoO₃ appears to be

stabilized by the interaction with the SBA-15 support material.

Conclusions

AHM dissolved in water is a useful Mo precursor, which can be readily introduced into the channels of SBA-15 without destroying the structure of mesoporous SBA-15 materials (XRD, TEM, and N_2 physisorption). The formation of the $[Mo_7O_{24}]^{6-}$ anion is observed in Raman spectra prior to calcination. After conversion of AHM to MoO_3 by a heat treatment, the Raman spectra show strong effects of the reduced dimensions of MoO_3 nanosized particles onto the vibrational properties. The appearance of a weak shoulder at about 953 cm^{-1} indicates that MoO_3 particles on the pore surface of SBA-15 form $(MoO_3)_n$ oligomers. The intensity of the reflections in the XRD patterns with increasing Mo content, the reduction of the pore volumes and of the surface areas obtained from the N_2 physisorption experiments reveal that MoO_3 particles are introduced into the channels of SBA-15. This is also confirmed by the application of HAADF technique combined with EDXS. In the wide-angle XRD patterns, reflections of α - MoO_3 appear only at high loadings of more than 13 wt% Mo, i.e., for lower MoO_3 contents the particle size is far below the coherence length of X-rays. This is further evidenced by comparing the powder pattern of a physical MoO_3 /SBA-15 mixture (7 wt% Mo) with that of SBA-15 materials with MoO_3 in the pores. The reflections of the mixture are much more intense than that of the material containing 17 wt% Mo. For higher Mo loading than 13 wt%, the reflections of α - MoO_3 become more intense with increasing MoO_3 content. However, at low Mo loading, the metastable hexagonal modification of MoO_3 appears to be stabilized by the interaction with the SBA-15 support material, which is clearly confirmed by the results of the EXAFS data analysis. Further experiments are under way to test the new materials in different catalytic reactions and as sensor materials.

Acknowledgements The financial support of the Deutsche Forschungsgemeinschaft (DFG), the Fonds der chemischen Industrie (FCI), and the State Schleswig-Holstein is gratefully acknowledged.

References

- Zhao DY, Huo QS, Feng JL, Chmelka BF, Stucky GD (1998) *J Am Chem Soc* 120:6024
- Zhao D, Feng J, Huo Q, Melosh N, Fredrickson GH, Chmelka BF, Stucky GD (1998) *Science* 279:548
- Han YJ, Kim JM, Stucky GD (2000) *Chem Mater* 12:2068
- Yang C, Liu P, Ho Y, Chiu C, Chao K (2003) *Chem Mater* 15:275
- Fukuoka A, Araki H, Sakamoto Y, Sugimoto N, Tsukada H, Kumai Y, Akimoto Y, Ichikawa M (2002) *Nano Lett* 2:793
- Wang D, Zhou WL, McCaughy BF, Hampsey JE, Ji X, Jiang Y-B, Xu H, Tang J, Schmehl RH, O'Connor C, Brinker CJ, Lu Y (2003) *Adv Mater* 15:130
- Lee K-B, Lee S-M, Cheon J (2001) *Adv Mater* 13:517
- Li L, Shi J-L, Zhang L-X, Xiong L-M, Yan J-N (2004) *Adv Mater* 16:1079
- Yuranov I, Kiwi-Minsker L, Buffat P, Renken A (2004) *Chem Mater* 16:760
- Konya Z, Puentes VF, Kiricsi I, Zhu J, Ager JW, Ko MK, Frei H, Alivisatos P, Somorjai GA (2003) *Chem Mater* 15:1242
- Yan WF, Chen B, Mahurin SM, Haganan EW, Dai S, Overbury SH (2004) *J Phys Chem B* 108:2793
- Luan ZH, Maes EM, van der Heide PAW, Zhao DY, Czernuszewicz RS, Kevan L (1999) *Chem Mater* 11:3680
- Gao F, Lu QY, Liu XY, Yan YS, Zhao DY (2001) *Nano Lett* 1:743
- Xu W, Liao YT, Akins DL (2002) *J Phys Chem B* 106:11127
- Hsueh HS, Yang CT, Zink JL, Huang MH (2005) *J Phys Chem B* 109:4404
- Yang CT, Huang MH (2005) *J Phys Chem B* 109:17842
- Brieler FJ, Grundmann P, Fröba M, Chen LM, Klar PJ, Heimbrodt W, von Nidda HAK, Kurz T, Loidl A (2004) *J Am Chem Soc* 126:797
- Brieler FJ, Fröba M, Chen LM, Klar PJ, Heimbrodt W, von Nidda HAK, Loidl A (2002) *Chem-Eur J* 8:185
- Braun S, Appel LG, Camorim VL, Schmal M (2000) *J Phys Chem B* 104:6584
- Mestl G, Srinivasan TKK, Knözinger H (1995) *Langmuir* 11:3795
- Kakuta N, Tohji K, Udagawa Y (1988) *J Phys Chem* 92:2583
- Desikan AN, Huang L, Oyama ST (1991) *J Phys Chem* 95:10050
- Li W, Meitzner GD, Borry R III, Iglesia E (2000) *J Catal* 191:373
- Stampfel SR, Chen Y, Dumesic JA, Niu C, Hill CG (1987) *J Catal* 105:445
- Ono T, Anpo M, Kubokawa Y (1986) *J Phys Chem* 90:4780
- Liu T-C, Forissier M, Coudurier G, Védrine JC (1989) *J Chem Soc Faraday Trans* 85:1607
- Giordano N, Meazza M, Castellani A, Bart JCI, Ragaini V (1977) *J Catal* 50:342
- Ressler T, Wienold J, Jentoft RE, Girsig F (2003) *Eur J Inorg Chem* 2:301
- Louis C, Tatibouet J-M, Che M (1988) *J Catal* 109:354
- Dhar GM, Kumaran GM, Kumar M, Rawat KS, Sharma LD, Raju BD, Rao KSR (2005) *Catal Today* 99:309
- Sampieri A, Pronier S, Blanchard J, Breyse M, Brunet S, Fajersberg K, Louis C, Perot G (2005) *Catal Today* 107–108:537
- Vradman L, Landau MV, Herskowitz M, Ezersky V, Talianker M, Nikitenko S, Koltypin Y, Gedanken A (2003) *Stud Surf Sci Catal* 146:721
- Wienold J, Jentoft RE, Ressler T (2003) *Eur J Inorg Chem* 6:1058
- Murugan R, Chang H (2001) *J Chem Soc Dalton* 3125
- Grunwaldt J-D, Hannemann S, Goettlicher J, Mangold S, Denecke MA, Baiker A (2005) *Phys Scr T* 115:769
- Lemonnier M, Collet O, Depautes C, Esteva J-M, Raoux D (1978) *Nuclear Instrum Methods* 152:109
- Ressler T (1998) *J Synchrotron Radiat* 5:118
- Rehr JJ, Booth CH, Bridges F, Zabinsky SI (1994) *Phys Rev B* 49:12347
- Ressler T, Brock SL, Wong J, Suib SL (1999) *J Phys Chem B* 103:6407
- Fröba M, Kohn R, Bouffaud G, Richard O, van Tendeloo G (1999) *Chem Mater* 11:2858
- A. IUPAC Manual of Symbols and Terminology, Part 1, *Pure Appl. Chem.* 31 (1972)

J Mater Sci (2008) 43:244–253

253

42. Lastoskie C, Gubbins KE, Quirke N (1993) *J Phys Chem* 97:4786
43. Van Der Voort P, Ravikovitch PI, De Jong KP, Benjelloun M, Van Bavel E, Janssen AH, Neimark AV, Weckhuysen BM, Vansant EF (2002) *J Phys Chem B* 106:5873
44. Kihlborg L (1963) *Ark Kemi* 21:357
45. Py MA, Maschke K (1981) *Physica B+C* 105:370
46. Jeziorowski H, Knoezinger H, Grange P, Gajardo P (1980) *J Phys Chem* 84:1825



ELSEVIER

Available online at www.sciencedirect.com

Journal of Catalysis 254 (2008) 170–179

JOURNAL OF
CATALYSISwww.elsevier.com/locate/jcat

Structure and properties of a supported MoO₃–SBA-15 catalyst for selective oxidation of propene

T. Ressler^{a,*}, A. Walter^a, Z.-D. Huang^b, W. Bensch^b^a Institut für Chemie, Technische Universität Berlin, Strasse des 17 Juni 135, D-10623 Berlin, Germany
^b Institut für Anorganische Chemie, University of Kiel, Olshausenstraße 40-60, D-24098 Kiel, Germany

Received 26 July 2007; revised 9 October 2007; accepted 13 December 2007

Available online 5 February 2008

Abstract

Local structure and catalytic properties of molybdenum oxide supported on nanostructured SiO₂ (SBA-15) were studied under reaction conditions by combined X-ray absorption spectroscopy (XAFS) and mass spectrometry. MoO₃ supported on SBA-15 exhibits stability and catalytic properties different from those of binary bulk oxides. The interaction between support and molybdenum oxide stabilizes particular hexagonal MoO₃ structure that is highly active and selective. The hex-MoO₃–SBA-15 is stable under reducing (propene) and oxidizing reaction conditions in the temperature range from 20 to 500 °C. In contrast to bulk hex-MoO₃, the onset of activity at about 250 °C is not accompanied by a transformation to α -MoO₃. Moreover, in contrast to α -MoO₃, hex-MoO₃–SBA-15 is capable of directly oxidizing propene to acrylic acid without additional metal sites.

© 2007 Elsevier Inc. All rights reserved.

Keywords: In situ; Heterogeneous catalysis; Structure–activity relationships; EXAFS spectroscopy; X-ray absorption; Molybdenum; Oxides; Hexagonal MoO₃; SBA-15; Support; SiO₂; Solid-state kinetics

1. Introduction

Molybdenum oxides constitute active heterogeneous catalysts for the selective oxidation of light alkenes and alkanes with gas phase oxygen. α -MoO₃ is the thermodynamic stable binary molybdenum oxide in the temperature range from 20 to 600 °C. However, pure α -MoO₃ exhibits only moderate catalytic activity, for instance, in the oxidation of propene to acrolein. Moreover, α -MoO₃ is a rather unselective oxidation catalyst oxidizing propene mostly to CO₂ and water. Addition of V or W during preparation of molybdenum oxides results in the formation of mixed oxides (e.g. (MoVW)₅O₁₄). The additional metal centers lead to the formation of a variety of characteristic structures. Many of these structures possess open channels such as hexagonal MoO₃ (Fig. 1) [1] or pentagonal columns like in Mo₅O₁₄ [2] and MoVNbTe oxides [3–5]. The latter exhibits a much higher selectivity compared to

α -MoO₃ [6,7]. Moreover, mixed Mo oxide catalysts are capable of oxidizing propene to acrylic acid which is not observed for α -MoO₃.

Similar to mixed molybdenum based oxides, binary Mo oxides form a variety of structures different from that of α -MoO₃ with average Mo valences in the range from 4 to 6. Many of these oxide structures can be readily prepared from a stoichiometric mixture of MoO₃ and MoO₂ at elevated temperatures (e.g. by chemical vapor transport). However, similar to α -MoO₃, the onset of reactivity of these various oxides coincides with the onset of bulk oxygen mobility [8,9]. Hence, under reaction conditions in oxygen and alkene at temperatures above 350 °C, most of these oxides rapidly form the more stable α -MoO₃.

With respect to structure–activity relationships it remains an open question whether additional metal centers in molybdenum oxides (chemical complexity) are inevitable for good activity and high selectivity. Alternatively, a particular structural motif rather than a particular chemical composition may be the prerequisite for high catalytic performance (structural complexity). Answering this question will permit understanding the func-

* Corresponding author. Fax: +49 30 314 21106.

E-mail address: thorsten.ressler@tu-berlin.de (T. Ressler).

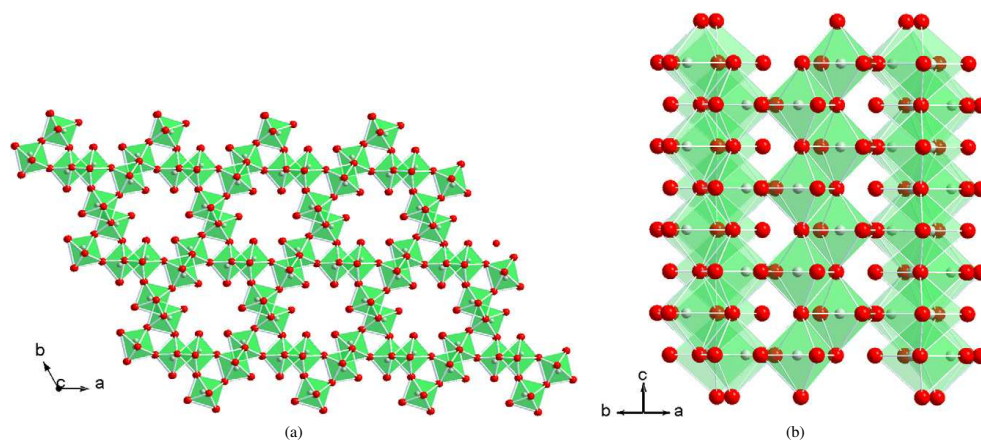


Fig. 1. Schematic representation of the structure of hexagonal MoO_3 [ICSD 75417] in the a - b plane (a) and in c direction (b).

tionality of molybdenum based catalysts and developing new and improved catalysts. In order to investigate molybdenum oxides other than α - MoO_3 under relevant reaction conditions, we have chosen supported molybdenum oxides. Supported oxides offer two advantages for investigating structure–activity relationships. First, interaction with the support may stabilize particular structures which would otherwise decompose into the more stable bulk α - MoO_3 . Second, suitable interaction of the Mo oxide with the support may result in a high dispersion and an improved surface to bulk ratio. Therefore, structural data that relate a particular structure of a catalyst under reaction conditions to its catalytic performance will be more reliable when determined for a catalytic material that possesses a high surface area.

Suitable support materials, in particular for catalyst model systems, should possess a large surface area and a homogeneous internal structure with reasonably large pores. In addition, the support should enable moderate interaction with the oxide catalyst but should be inactive in the oxidation of alkenes. Nanostructured SiO_2 materials such as SBA-15 [10,11] constitute suitable support systems for oxide catalysts [12–15]. Vanadium oxide supported on SBA-15, for instance, has been suggested to exhibit isolated VO_4 species or low dimensional oxides. However, the detailed local structure of the supported oxide under reaction conditions is still being debated. Furthermore, little has been reported on improved catalytic properties of the supported oxides compared to conventional bulk catalysts. Here, we present investigations of the structure and the catalytic performance of molybdenum oxide supported on nanostructured SiO_2 for the selective oxidation of propene.

2. Experimental

2.1. Preparation of hex- MoO_3 supported on SBA-15

8 g of poly(ethylene glycol)-block-poly(propylene glycol)-block-poly(ethylene glycol) triblock copolymer (Aldrich, plu-

ronic, P-123) was dissolved in 240 g of water and 28.6 g of concentrated hydrochloric acid at 30 °C on a water bath. After drop wise addition of 16 g of tetraethyl orthosilicate (TEOS), the reaction mixture was stirred for 24 h at 30 °C. The resulting gel was transferred into a Teflon bottle and heated to 80 °C for 24 h to obtain SBA-15 with 6 nm pores. The resulting white powder was filtered and washed with deionized water, and the surfactant was removed by Soxhlet extraction at 78 °C with a mixture of 970 mL of ethanol and 30 mL of concentrated hydrochloric acid. After washing with ethanol, the white powder was dried at RT for about one week.

Typically, 1 g of SBA-15 was stirred in aqueous solutions containing ammonium heptamolybdate $(\text{NH}_4)_6\text{Mo}_7\text{O}_{24}\cdot 4\text{H}_2\text{O}$ (AHM, 0.09 mol/L) at pH 7–8. After stirring at room temperature for 18 h, the products were filtered without washing. The impregnated SBA-15 was calcined at 500 °C for 3 h in air to obtain MoO_3 . The Mo loading of the catalysts was 13 wt% and the synthesized products were stored in dried air. Further details on the preparation procedure and structural characterization of the material obtained are provided in Ref. [16]. Commercial α - MoO_3 (Aldrich) was employed as-is. Hexagonal MoO_3 was prepared by precipitation from an aqueous solution of AHM (0.7 mol/L (Mo)) by addition of HNO_3 (1 mol/L). The precipitation was conducted at 50 °C and a pH of 1. Subsequently, the sample was aged for 1 h at 35 °C, filtered, and dried in a desiccator [17]. Phase purity and structure of the reference oxides (hex- MoO_3 , ICSD 75417) were confirmed by X-ray powder diffraction. The three samples investigated here are denoted as follows: bulk orthorhombic MoO_3 (α - MoO_3), bulk hexagonal MoO_3 (hex- MoO_3), and hexagonal MoO_3 supported on SBA-15 (hex- MoO_3 -SBA-15). Upon activation under reducing or reaction conditions hex- MoO_3 -SBA-15 exhibits characteristic structural changes. To distinguish between the as-prepared hex- MoO_3 -SBA-15 and the material under reaction conditions, the activated sample is denoted as MoO_x -SBA-15.

2.2. X-ray absorption spectroscopy (XAS)

In situ transmission XAS experiments were performed at the Mo K-edge (19.999 keV) at beamline X1 at the *Hamburg Synchrotron Radiation Laboratory*, HASYLAB, using a Si(311) double crystal monochromator (measuring time ~ 4 min/scan). The storage ring operated at 4.4 GeV with injection currents of 150 mA. The in situ experiments were conducted in a flow-reactor at atmospheric pressure in flowing reactants (1 vol% propene in He, 5 vol% oxygen in He, total flow ~ 30 mL/min, temperature range from 25 to 500 °C, heating rate 4 K/min). The gas phase composition at the cell outlet was continuously monitored using a non-calibrated mass spectrometer in a multiple ion detection mode (QMS200 from *Pfeiffer*). The mass spectrometer was used for its suitable time resolution. Because Faraday cup and channeltron were employed as detectors, reliable calibration and quantification were not feasible. Hex-MoO₃-SBA-15 is introduced as model system. A quantitative comparison to more active or industrial catalysts was not intended. Conversion of propene was estimated from the propene ion current (m/e 42) before and during reaction to be about 10% at 450 °C. Hexagonal MoO₃ and α -MoO₃ were mixed with boron nitride (~ 7 mg MoO₃, 30 mg BN) and pressed with a force of 1 ton into a 5 mm in diameter pellet resulting in an edge jump at the Mo K-edge of $\Delta\mu_x \sim 1$. Hex-MoO₃-SBA-15 was employed as-is. X-ray absorption fine structure (XAFS) analysis was performed using the software package WinXAS v3.1 [18]. Background subtraction and normalization were carried out by fitting linear polynomials to the pre-edge and the post-edge region of an absorption spectrum, respectively. The extended X-ray absorption fine structure (EXAFS) $\chi(k)$ was extracted by using cubic splines to obtain a smooth atomic background, $\mu_0(k)$. The radial distribution function $FT(\chi(k))$ was calculated by Fourier transforming the k^3 -weighted experimental $\chi(k)$ function, multiplied by a Bessel window, into the R space. EXAFS data analysis was performed using theoretical backscattering phases and amplitudes calculated with the ab initio multiple-scattering code FEFF7 [19]. Single scattering and multiple scattering paths in the hex-MoO₃ model structure (ICSD 75417 [1]) were calculated up to 6.0 Å with a lower limit of 4.0% in amplitude with respect to the strongest backscattering path. EXAFS refinements were performed in R space simultaneously to magnitude and imaginary part of a Fourier transformed k^3 -weighted and k^1 -weighted experimental $\chi(k)$ using the standard EXAFS formula (k range from 3.4 to 15.1 Å⁻¹, R range 0.7 to 4.1 Å) [20]. Structural parameters determined are (i) one E_0 shift, (ii) Debye–Waller factors for single-scattering paths, and (iii) distances of single-scattering paths. Coordination numbers (CN) and S_0^2 were kept invariant in the refinement.

3. Results and discussion

MoO₃ supported on SBA-15 was prepared by impregnation of SBA-15 with ammonium heptamolybdate solution followed by calcination in air at 500 °C. Structure and properties of the resulting molybdenum oxide on SBA-15 under reaction condi-

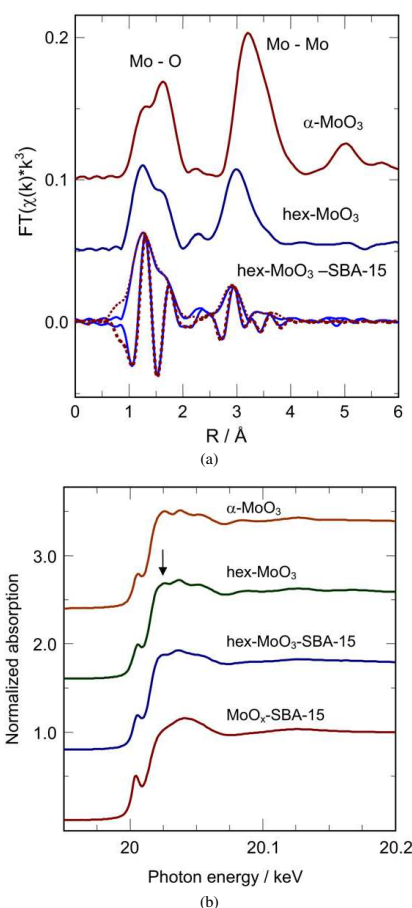


Fig. 2. Experimental Mo K-edge Fourier transformed $\chi(k)$ of hexagonal MoO₃, α -MoO₃, and hex-MoO₃-SBA-15 (13 wt% MoO₃) together with a theoretical XAFS function (a) and Mo K-edge XANES spectra of α -MoO₃, hexagonal MoO₃, hex-MoO₃-SBA-15, and activated MoO_x-SBA-15 under reaction conditions (propene + oxygen) (arrow indicates distinct differences in spectra of hex-MoO₃ and α -MoO₃) (b).

tions was studied by combined X-ray absorption spectroscopy (XAFS) and mass spectrometry. The Mo K near-edge spectra (XANES) and the Fourier transformed XAFS $\chi(k)$ function of hex-MoO₃-SBA-15 are compared to those of α -MoO₃ and bulk hex-MoO₃ in Fig. 2. The relative amplitudes of the features in the XANES spectrum of hex-MoO₃-SBA-15 resemble more closely that of hex-MoO₃ than that of α -MoO₃ (arrow in Fig. 2). Analysis of the Mo K-edge position yields an average valence of 6. The Fourier transformed XAFS $\chi(k) \cdot k^3$ are not phase shift corrected. Thus, the distances in the $FT(\chi(k) \cdot k^3)$ are shifted by ~ 0.4 Å to lower values compared to the crystallographic distances. In the range of Mo–O distances, the $FT(\chi(k) \cdot k^3)$ of hex-MoO₃-SBA-15 strongly resembles that

Table 1

Type and number (N) of atoms at distance R from the Mo atoms in a hex-MoO₃ model system compared to experimental distances and XAFS Debye–Waller factors (σ^2). Experimental parameters were obtained from a refinement of a hex-MoO₃ model structure (ICSD 75417) to the experimental Mo K-edge XAFS $\chi(k)$ of hex-MoO₃, hex-MoO₃–SBA-15 (Fig. 2), and MoO_x–SBA-15 under reaction conditions (Fig. 12) (k range from 3 to 14 Å⁻¹, R range from 0.9 to 4.1 Å, E_0 (hex-MoO₃) = -6.5 eV, E_0 (hex-MoO₃–SBA-15) = -6.6 eV, E_0 (MoO_x–SBA-15) = -5.9 eV, residual = 6.7, $N_{\text{ind}} = 25$, $N_{\text{free}} = 17$). The uncertainty in the distances and the Debye–Waller factors amounts to about 0.03 Å and 0.0002 Å², respectively

Type	N	Model hex-MoO ₃			hex-MoO ₃		hex-MoO ₃ –SBA-15		Activated MoO _x –SBA-15	
		R (Å)	R (Å)	σ^2 (Å ²)	R (Å)	σ^2 (Å ²)	R (Å)	σ^2 (Å ²)	R (Å)	σ^2 (Å ²)
Mo–O	1	1.68	1.68	0.0010	1.69	0.0058	1.67	0.0020		
Mo–O	1	1.73	1.75	0.0031	1.73	0.0019	1.69	0.0010		
Mo–O	2	1.97	1.97	0.0051	1.98	0.0035	1.90	0.0022		
Mo–O	1	2.20	2.25	0.0020	2.28	0.0033	2.32	0.0075		
Mo–O	1	2.39	2.40	0.0017	2.42	0.0078	2.36	0.0135		
Mo–Mo	2	3.31	3.33	0.0042	3.31	0.0075	3.23	0.0142		
Mo–Mo	2	3.73	3.73	0.0035	3.79	0.0072	3.74	0.0327		
Mo–Mo	2	4.03	3.93	0.0185	3.91	0.0221	3.94	0.0191		

of hex-MoO₃. Structural parameters obtained from a XAFS refinement are given in Table 1. Also in the range of Mo–Mo distances, the $FT(\chi(k) \cdot k^3)$ of hex-MoO₃–SBA-15 can be very well described by a hexagonal MoO₃ model structure. Apparently, no isolated MoO_x species on SiO₂ were detected. The Mo–Mo distance of 3.7 Å in the structure of hexagonal MoO₃ corresponds to the distance between corner-sharing MoO₆ units (Fig. 1). A particularly increased Debye–Waller factor of this scattering path is obtained for hex-MoO₃–SBA-15 compared to bulk hex-MoO₃. Hence, the reduced amplitude in the range of the Mo–Mo distances is ascribed to a predominantly two-dimensional hexagonal MoO₃ structure supported on SBA-15. Apparently, the two-dimensional hexagonal MoO₃ supported on SBA-15 is stabilized by suitable interactions with the support. The lattice parameter c of the hexagonal MoO₃ modification is oriented perpendicular to the surface of the SiO₂ support (Fig. 1). The increased Debye–Waller factors of the Mo–Mo distance in the a – b plane of hex-MoO₃–SBA-15 corresponds to an increased static disorder in the MoO_x layer supported on SiO₂ compared to bulk hex-MoO₃. After thermal treatment a further increase of the Debye–Waller factor indicates a more pronounced two-dimensional hexagonal MoO₃ layer structure on SBA-15 under reaction conditions.

3.1. Treatment of bulk hex-MoO₃ and hex-MoO₃–SBA-15 under reducing conditions

Hex-MoO₃–SBA-15 exhibited a surprising stability compared to bulk hex-MoO₃. Calcination of ammonium heptamolybdate in air results in a temporary formation of hex-MoO₃ which rapidly transforms to α -MoO₃ upon further heating [21]. Conversely, hex-MoO₃–SBA-15 is stable at 500 °C in air. Similarly, the reduction behavior of hex-MoO₃–SBA-15 differs from that of bulk hex-MoO₃. Fig. 3 shows the evolution of Mo K-edge XANES spectra of bulk hex-MoO₃ during temperature-programmed reduction (TPR) in propene (20–500 °C, 4 K/min, 1% propene in He). The characteristic XANES spectrum of the resulting oxide at 500 °C indicates that hex-MoO₃ is fully reduced to MoO₂. The corresponding evolution of the ion current of H₂O (m/e 18), acrolein (m/e 56), and CO₂ (m/e 44) during TPR of hex-MoO₃ in propene is depicted in Fig. 4. The on-

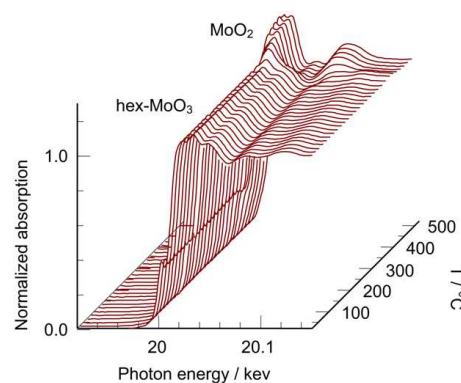


Fig. 3. Evolution of Mo K-edge XANES spectra of hex-MoO₃ during temperature-programmed reduction in propene (20–500 °C, 4 K/min, 1% propene in He).

set of reduction is at about 350 °C. A detailed discussion of the reduction mechanism and the different profiles of the ion current traces of the oxidation products is beyond the scope of this manuscript and may be presented elsewhere. The clearly separated peaks in the TPR profile are indicative of a multiple step reduction process and the formation of at least two intermediate phases.

The evolution of the Mo K-edge XAFS $FT(\chi(k) \cdot k^3)$ of hex-MoO₃ during TPR in propene is displayed in Fig. 5. Both the XANES spectra shown in Fig. 3 and the $FT(\chi(k) \cdot k^3)$ shown in Fig. 5 exhibit the formation of intermediates in the temperature range from 350 to 400 °C. The $FT(\chi(k) \cdot k^3)$ of the oxide formed above 400 °C is similar to that of MoO₂. The distinct changes in amplitude of the $FT(\chi(k) \cdot k^3)$ in the range from 350 to 400 °C indicates the formation of more than one intermediate during reduction of hex-MoO₃. Also, a factor analysis of the XANES spectra shown in Fig. 3 yielded four components required to simulate the experimental spectra.

In contrast to the behavior of bulk hex-MoO₃ during TPR in propene, hex-MoO₃–SBA-15 is not fully reduced to MoO₂ during treatment in propene at 500 °C. The evolution of Mo K-edge

174

T. Ressler et al. / Journal of Catalysis 254 (2008) 170–179

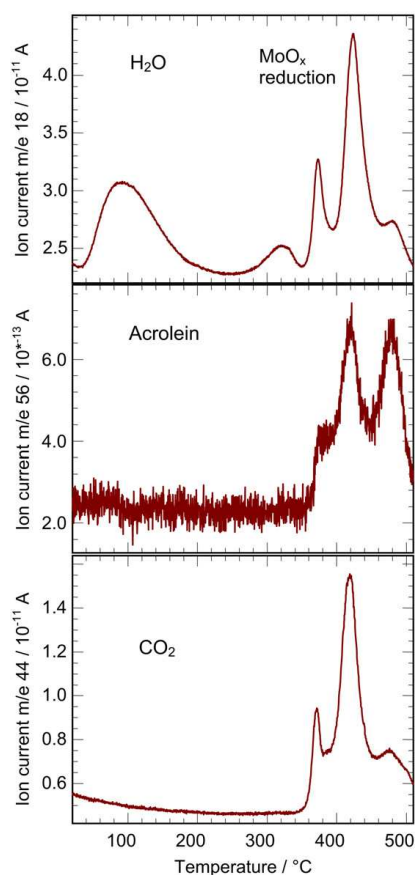


Fig. 4. Evolution of ion current of H₂O (*m/e* 18), acrolein (*m/e* 56), and CO₂ (*m/e* 44) during temperature-programmed reduction of hex-MoO₃ in propene (20–500 °C, 4 K/min, 1% propene in He).

XANES spectra of hex-MoO₃-SBA-15 during temperature-programmed reduction in propene (20–500 °C, 4 K/min, 1% propene in He) is depicted in Fig. 6a. The Mo K-edge XANES of the resulting partially reduced oxide resembles that of MoO_x-SBA-15 as depicted in Fig. 2. A slightly increased pre-edge peak and less distinct XANES features are visible in the spectrum of the MoO_x-SBA-15 at 400 °C. Both correspond to an increased distortion of the local Mo–O coordination and a disordered two-dimensional hex-MoO₃ structure as will be discussed below. Upon heating to 500 °C the pre-edge peak slightly decreased and became less pronounced. Fig. 6b shows the corresponding evolution of the ion currents of H₂O (*m/e* 18). Compared to the evolution of water during reduction of bulk hex-MoO₃ at 400 °C (Fig. 3), very little water evolves during thermal treatment of hex-MoO₃-SBA-15. This indicates a lower reducibility and an increased structural stability. The strong interaction between the hexagonal MoO₃ and SBA-15

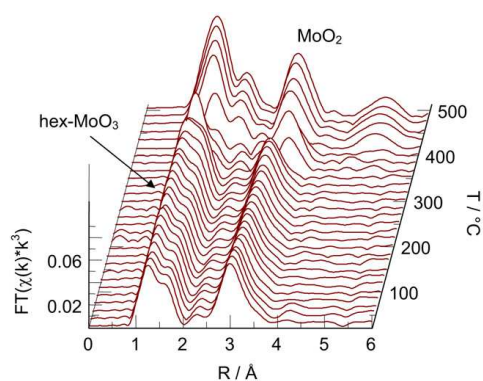


Fig. 5. Evolution of Mo K-edge XAFS $FT(\chi(k) \cdot k^3)$ of hex-MoO₃ during temperature-programmed reduction in propene (20–500 °C, 4 K/min, 1% propene in He).

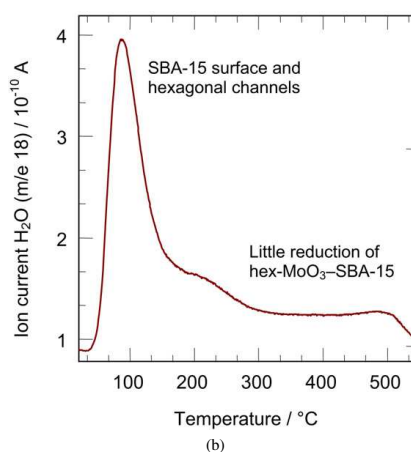
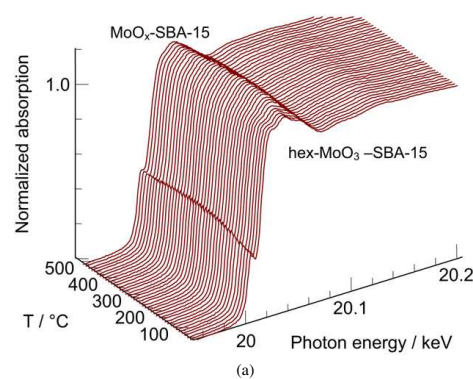


Fig. 6. Evolution of Mo K-edge XANES spectra (a) of hex-MoO₃-SBA-15 during temperature-programmed treatment in propene (20–500 °C, 4 K/min, 1% propene in He) together with (b) the evolution of ion current of H₂O (*m/e* 18).

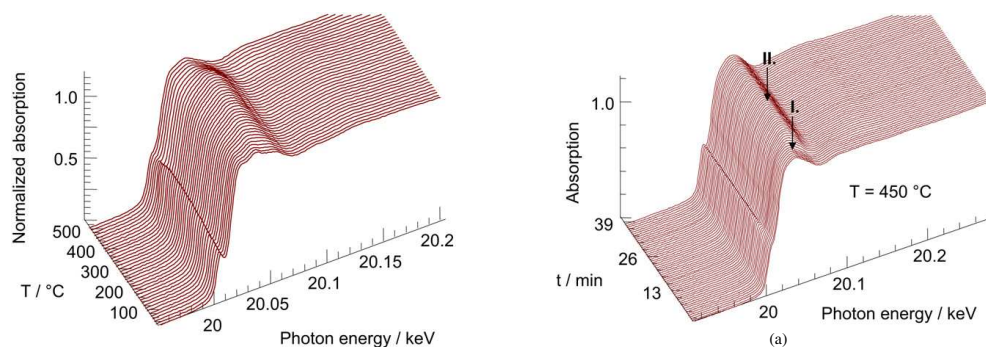


Fig. 7. Evolution of Mo K-edge XANES spectra of hex-MoO₃-SBA-15 during temperature-programmed treatment in hydrogen (20–500 °C, 4 K/min, 5% H₂ in He).

support that inhibits the formation of α -MoO₃ under oxidative conditions also prevents the reduction to MoO₂ in propene.

In addition to treatment of hex-MoO₃-SBA-15 in propene, treatment in 5% hydrogen in helium was studied. The corresponding evolution of Mo K-edge XANES spectra of hex-MoO₃-SBA-15 during treatment in hydrogen in the temperature range from 30 to 500 °C is depicted in (Fig. 7). Similar to the treatment in propene, the Mo K-edge spectrum of hex-MoO₃-SBA-15 exhibited an increase in pre-edge peak followed by a decrease at temperatures above 450 °C. The resulting phase resembled that obtained after treatment of hex-MoO₃-SBA-15 in propene. In contrast to bulk hex-MoO₃, hex-MoO₃-SBA-15 was stable at 500 °C in hydrogen and did not exhibit further decomposition or reduction to MoO₂. Hence, the results of the treatment in hydrogen exclude the formation of carbonaceous deposits being the origin of the low reducibility of hex-MoO₃-SBA-15. The low reducibility in hydrogen further corroborates the effect of the interaction between the hexagonal MoO₃ and the SBA-15 support on the stability of hex-MoO₃-SBA-15.

Apparently, the lattice oxygen of hexagonal MoO₃ supported on SBA-15 is not readily available to gaseous reactants. The very low reducibility and the formation of an activated species during treatment in propene is similar to the behavior of polyoxomolybdates (e.g. H₄[PVMo₁₁O₄₀]) under reaction conditions [22,23]. Despite this low reducibility, the hex-MoO₃-SBA-15 constitutes a better oxidation catalyst than bulk hex-MoO₃ and α -MoO₃. The onset of reduction and oxygen mobility in molybdenum oxides correlates with the onset of catalytic activity. However, the low reducibility of hex-MoO₃ on SBA-15 indicates that pronounced oxygen mobility in the bulk may not necessarily be required for good catalytic performance.

In order to further elucidate the stability and catalytic properties of hex-MoO₃-SBA-15 under changing reaction conditions, oxygen was added temporarily to the propene feed at 450 °C. Prior to the addition of oxygen, hex-MoO₃-SBA-15 was treated in propene at 500 °C for 15 min. This resulted in a slight reduction of the Mo oxide phase as can be seen from the decreased Mo K pre-edge peak (Fig. 8). Subsequently, oxygen was added

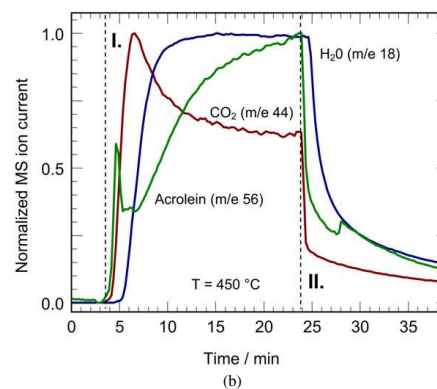


Fig. 8. (a) Evolution of Mo K-edge XANES spectra during isothermal ($T = 450$ °C) addition of oxygen (5% oxygen in He) during treatment of hex-MoO₃-SBA-15 in propene (1% propene in He) (I.—oxygen on; II.—oxygen off). (b) Evolution of normalized ion currents of H₂O (m/e 18), acrolein (m/e 56), and CO₂ (m/e 44) obtained by mass spectrometric analysis of the gas phase composition during isothermal addition of oxygen (a). Dashed lines indicate oxygen on (~ 3.5 min, I.) or oxygen off (~ 24 min, II.).

to the propene feed at 450 °C and switched off again after 20 min. During the isothermal re-oxidation phase (propene + O₂ on) and the re-reduction phase (only propene on) Mo K-edge XANES spectra were collected with a time-resolution of 30 s. After the oxidation and reduction treatment, the EXAFS spectrum of the resulting Mo oxide phase supported on SBA-15 was measured. The spectrum and, thus, the local structure of the molybdenum oxide corresponded to that of MoO₃-SBA-15 as depicted and discussed in Fig. 12. Hence, the structure of the molybdenum oxide phase supported on SBA-15 after reduction and re-oxidation treatment still corresponded to that of hexagonal MoO₃.

The evolution of the XANES spectra and of the MS ion traces of CO₂, H₂O, and acrolein measured during addition of oxygen to the propene feed at 450 °C are depicted in Fig. 8 (the jump in the m/e 56 signal at ~ 5 min was probably caused by a slight change in pressure and sensitivity of the MS). While the concentration of CO₂ in the gas phase exhibited a spiked increase, the concentration of acrolein increased more slowly.

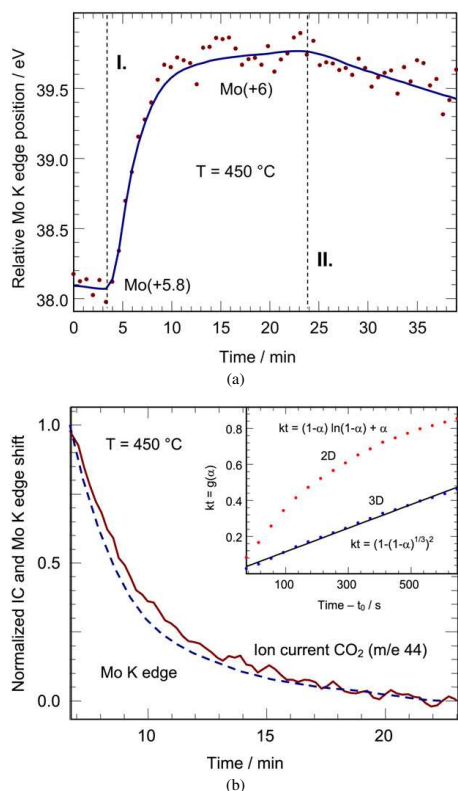


Fig. 9. (a) Evolution of relative Mo K-edge position during isothermal ($T = 450\text{ }^{\circ}\text{C}$) addition of oxygen (5% oxygen in He) during treatment of hex-MoO₃-SBA-15 in propene (1% propene in He) (Fig. 8). The average Mo valence in the reduced state (~ 2 min) and the re-oxidized state (~ 20 min) is indicated. Dashed lines correspond to addition (~ 3.5 min, I) or removal (~ 24 min, II) of oxygen. (b) Normalized ion current (IC) of CO₂ (m/e 44) together with normalized Mo K-edge position during addition of oxygen (phase I, in Figs. 8 and 9a). The inset shows the integrated function $g(\alpha)$ of the extent of reduction α for a two-dimensional (2D) and three-dimensional (3D) diffusion solid-state kinetic model.

The similar time constants of the increasing acrolein concentration and the decreasing CO₂ concentration may correspond to an increasing selectivity during the re-oxidation phase. The evolution of the Mo K-edge position during the oxidation and reduction treatment at $450\text{ }^{\circ}\text{C}$ is depicted in Fig. 9a. The edge position was determined as specified in Ref. [8]. Upon adding oxygen to the propene feed at $450\text{ }^{\circ}\text{C}$, the Mo K-edge shifted to higher energies indicative of an increased average Mo valence. According to our previously reported calibration curve [8], the molybdenum K-edge positions measured correspond to an average Mo valence of 5.8 after treatment in propene at $500\text{ }^{\circ}\text{C}$ and of ~ 6.0 after re-oxidation in propene and oxygen (~ 20 min in Fig. 9a). After switching off the oxygen (II. in Fig. 9a), the Mo K-edge of hex-MoO₃-SBA-15 in propene at $450\text{ }^{\circ}\text{C}$ exhibited

a slow shift towards lower photon energies. This slow reduction confirms the stability of the hexagonal MoO₃ supported on SBA-15. Fig. 9b correlates the re-oxidation rate of the Mo oxide phase in propene and oxygen with the decreasing CO₂ concentration in the gas phase (Fig. 8). For comparison, the Mo K-edge shift was inverted and the amplitudes of the two traces were normalized to one. Apparently, the increase in Mo average valence and the decrease in CO₂ formation proceed at about the same rate. The inset in Fig. 9b shows the integrated function $g(\alpha)$ of the extent of oxidation α calculated for two solid-state kinetics models (i.e. two-dimensional diffusion or three-dimensional diffusion as rate-limiting step). The inverted and normalized Mo K-edge shift depicted in Fig. 9a was taken as extent of oxidation α . The function $g(\alpha)$ is linear with time if the corresponding model is suitable to simulate the experimental data. Solid-state kinetic models tested include one-, two-, or three-dimensional diffusion, various power laws, and Avrami-Erofeev equations [24]. During the first three minutes after adding oxygen to the propene feed the rate of re-oxidation of the Mo is mainly determined by transport of oxygen into the in situ cell. Here, surface or near-surface Mo centers may be rapidly re-oxidized. After three minutes a solid-state kinetic model that assumes three-dimensional diffusion in the Mo oxide bulk to be the rate-limiting step was suited best to simulate the experimental α trace (i.e. Mo K-edge shift) (Fig. 9b). Moreover, Fig. 9b indicates a correlation between the time-dependent change of the average Mo valence and the selectivity of the MoO_x-SBA-15 phase under selective oxidation reaction conditions. A similar behavior including rate-limiting three-dimensional diffusion has been reported for activated polyoxomolybdates (i.e. H₅[PV₂Mo₁₀O₄₀]) during alternating treatment in propene and propene and oxygen [23]. While a more reduced MoO_x-SBA-15 exhibits a decreased selectivity, the selectivity increases with an increasing average Mo valence during re-oxidation of MoO_x-SBA-15 in propene and oxygen.

3.2. Treatment of bulk hex-MoO₃ and hex-MoO₃-SBA-15 under catalytic conditions

The evolution of the Mo K-edge XAFS $FT(\chi(k) \cdot k^3)$ of bulk hex-MoO₃ during thermal treatment under catalytic reaction conditions (1% propene and 5% oxygen in He) is depicted in Fig. 10. The transformation of hex-MoO₃ to α -MoO₃ at about $350\text{ }^{\circ}\text{C}$ is easily detectable. In agreement with the good reducibility of bulk hex-MoO₃ in propene, hex-MoO₃ readily underwent structural changes under reaction conditions in propene and oxygen. Interestingly, an increase in FT amplitude can be seen prior to the transformation to α -MoO₃. This behavior was similar to the increase in amplitude at about $350\text{ }^{\circ}\text{C}$ that can be seen in the evolution of the $FT(\chi(k) \cdot k^3)$ of bulk hex-MoO₃ during treatment in propene prior to reduction to MoO₂. Apparently, an intermediate phase was also formed during treatment under catalytic reaction conditions. The evolution of the MS ion currents of H₂O (m/e 18), acrolein (m/e 56), and CO₂ (m/e 44) measured during treatment of hex-MoO₃ in propene and oxygen is depicted in Fig. 11. The rapid increase in activity at about $350\text{ }^{\circ}\text{C}$ coincided with the formation of the

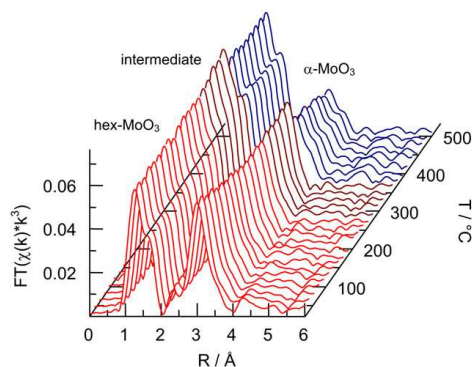


Fig. 10. Evolution of Mo K-edge XAFS $FT(\chi(k) \cdot k^3)$ during thermal treatment of hex-MoO₃ in propene and oxygen (20–500 °C, 4 K/min, 1% propene and 5% oxygen in He). The different phases (i.e. hex-MoO₃, α -MoO₃, and an intermediate) are indicated.

intermediate phase. Upon further heating the activity declined corresponding to the transition to α -MoO₃. No formation of acrylic acid was detected during treatment of hex-MoO₃ under catalytic reaction conditions. Hence, the in situ data shown in Figs. 10 and 11 reveal the formation of an intermediate phase with interesting catalytic properties. However, the low stability of this intermediate under reaction conditions did not permit detailed structural characterization and catalytic testing.

While, bulk hex-MoO₃ decomposed to α -MoO₃ at temperatures above 350 °C in propene and oxygen (Fig. 10), hex-MoO₃-SBA-15 remained stable up to 500 °C (Fig. 12). During thermal treatment under catalytic conditions the as-prepared hex-MoO₃-SBA-15 exhibited only moderate structural changes below 200 °C. After removal of water from the channel structure between 100 and 200 °C (Fig. 6), the $FT(\chi(k) \cdot k^3)$ of the oxide formed remained unchanged up to 500 °C. The corresponding XANES spectrum of activated hex-MoO₃-SBA-15 under reaction conditions is shown in Fig. 2 (denoted as MoO_x-SBA-15). The increased pre-edge peak is indicative of an increased distortion of the local Mo–O coordination compared to bulk hex-MoO₃ and α -MoO₃. The result of a XAFS refinement of the hexagonal MoO₃ model structure (Fig. 1) to the experimental spectrum of MoO_x-SBA-15 under reaction conditions is depicted in Fig. 12b. Similar to the spectrum of the as-prepared hex-MoO₃-SBA-15, a good agreement between theoretical and experimental spectrum was obtained. The corresponding structural parameters are given in Table 1. Hence, the local structure of MoO_x-SBA-15 is also very similar to that of hexagonal MoO₃. Again, a majority of isolated MoO₄ units on the SiO₂ support can be excluded. An increased splitting of the FT peak at about 1.2 Å that corresponds to the first Mo–O coordination sphere can be seen in Fig. 12b. This corroborates the XANES analysis of an increased local distortion of the MoO₆ units in activated MoO_x-SBA-15. Moreover, the significantly increased Debye–Waller factor of the Mo–Mo scattering path with a distance of 3.7 Å also constitutes a pronounced difference compared to XAFS refinement results of

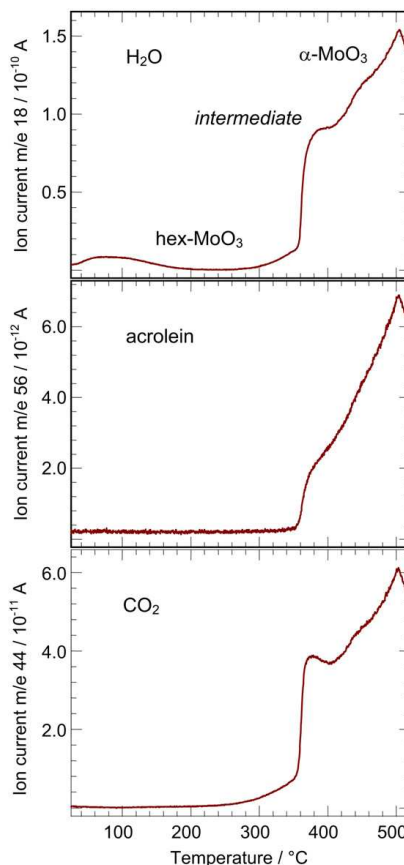


Fig. 11. Evolution of ion currents of H₂O (m/e 18), acrolein (m/e 56), and CO₂ (m/e 44) obtained by mass spectrometric analysis of the gas phase composition during thermal treatment of hex-MoO₃ in propene and oxygen (Fig. 10) (20–500 °C, 4 K/min, 1% propene and 5% oxygen in He). The different phases (i.e. hex-MoO₃, α -MoO₃, and an intermediate) are indicated.

the as-prepared hex-MoO₃-SBA-15. This distance corresponds to the extensions of the channels of hexagonal MoO₃ (Fig. 1). The strong decrease of the detectable contribution of this distance to the overall $FT(\chi(k) \cdot k^3)$ indicates a reduced length of the channels and emphasizes a two-dimensional layer structure of hexagonal MoO₃ supported on SBA-15.

Apparently, the local structure of the as-prepared hex-MoO₃-SBA-15 resembles more closely that of bulk hex-MoO₃ than the activated MoO_x-SBA-15 (Fig. 2b). The reactivity of the as-prepared hex-MoO₃-SBA-15 is strongly modified by interaction with the SiO₂ support. This results in the high stability and low reducibility observed (Fig. 6). However, the local structure is dominated by the water still intercalated in the channel structure of the hexagonal modification of MoO₃. Upon removal of water (i.e. dehydration) the local structure slightly

178

T. Ressler et al. / Journal of Catalysis 254 (2008) 170–179

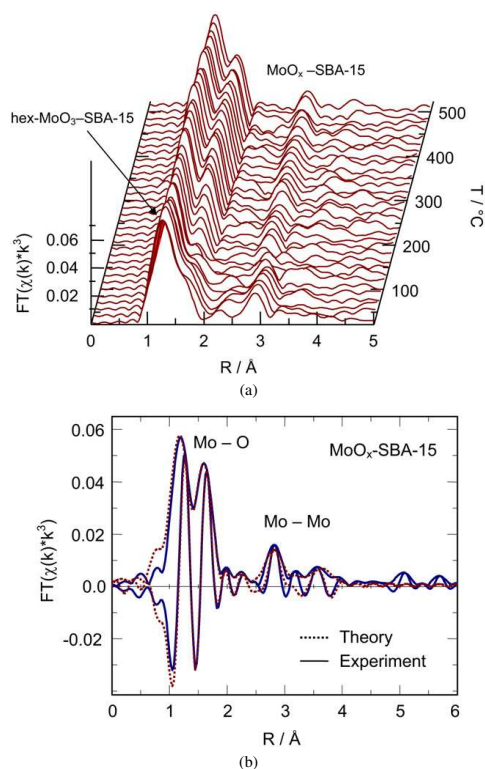


Fig. 12. Evolution of Mo K-edge XAFS $FT(\chi(k) \cdot k^3)$ measured during thermal treatment of hex- $\text{MoO}_3\text{-SBA-15}$ in propene and oxygen (20–500 °C, 4 K/min, 1% propene and 5% oxygen in He) (a). Experimental and theoretical XAFS function of $\text{MoO}_x\text{-SBA-15}$ activated in propene and oxygen (b).

rearranges. This may maximize the interaction with the SiO_2 support of the characteristic layer structure of the activated $\text{MoO}_x\text{-SBA-15}$ phase under reaction conditions.

3.3. Catalytic performance of hex- $\text{MoO}_3\text{-SBA-15}$

The MS ion currents of CO_2 (m/e 44), acrolein (m/e 56), and acrylic acid (m/e 72) measured during thermal treatment of hex- $\text{MoO}_3\text{-SBA-15}$ and $\alpha\text{-MoO}_3$ in propene (1% in He) and oxygen (5% in He) in the temperature range from 20 to 500 °C are depicted in Fig. 13. Apparently, the activated hex- $\text{MoO}_3\text{-SBA-15}$ catalyst was more active and more selective compared to bulk $\alpha\text{-MoO}_3$. The onset temperature of activity of $\text{MoO}_x\text{-SBA-15}$ was shifted to lower temperatures (~ 250 °C). The ratio of the Mo K-edge jump of hex- $\text{MoO}_3\text{-SBA-15}$ and $\alpha\text{-MoO}_3$ amounted to (1:1.6). Normalized to the amount of Mo in the samples, hex- $\text{MoO}_3\text{-SBA-15}$ was both more active and more selective than $\alpha\text{-MoO}_3$ (Fig. 13).

Most interestingly, though, hex- MoO_3 on SBA-15 was capable of selectively oxidizing propene to acrylic acid (Fig. 13).

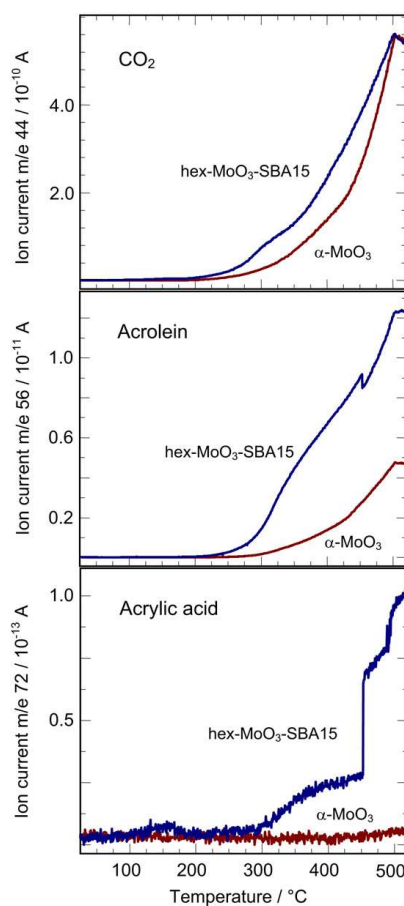


Fig. 13. Evolution of ion currents of CO_2 (m/e 44), acrolein (m/e 56), and acrylic acid (m/e 72) obtained by mass spectrometric analysis of the gas phase composition during thermal treatment of hex- $\text{MoO}_3\text{-SBA-15}$ or $\alpha\text{-MoO}_3$ in propene and oxygen (20–500 °C, 4 K/min, 1% propene and 5% oxygen in He).

This was not observed during catalytic testing of $\alpha\text{-MoO}_3$. Binary Mo oxides without additional metal sites were assumed to be incapable of oxidizing propene to acrylic acid. Our data suggest that an increased activity and selectivity is possible without introduction of additional metal centers. The stabilized structure of the hexagonal MoO_3 supported on SBA-15 showed not only an increased selectivity but also a new functionality. Therefore, additional metal centers in molybdenum oxide based catalysts are not necessarily required. Evidently, a suitable molybdenum oxide structure alone is capable of activating propene and gas phase oxygen, and selectively oxidizing propene to acrylic acid (Fig. 13). Intriguingly, the stabilized structure of hexagonal MoO_3 supported on SBA-15 possesses structural motifs (i.e. an open channel structure) similar to those of the highly active Mo_5O_{14} or “ MoVNbTe ” catalysts. Hence,

structural complexity of molybdenum oxides is sufficient to improve functional molybdenum sites for the activation of oxygen and alkene followed by selective oxidation of the alkene. Additional metal sites may add functionality and result in further improved catalytic properties. However, adjusting the microstructure of the catalyst (*structural complexity*) may be more important than adjusting chemical composition (*chemical complexity*).

Previous approaches to elucidating structure–activity relationships employing mixed oxide catalysts often simultaneously altered both chemical and structural complexity. This makes it difficult to unravel their individual effects. Hexagonal MoO₃ supported on SBA-15 appears to be more suitable to further elucidate the correlations between the structure of molybdenum oxides and the catalytic performance. In particular, the characteristic electronic structure (shape of XANES spectra) of the more active and selective MoO_x–SBA-15 under reaction conditions (Fig. 2) could serve as a basis for further theoretically modeling and structural characterization. Once a reliable correlation between structure and properties has been established, further metal centers may be introduced to unravel the effect of additional functional sites on the catalytic performance.

4. Conclusions

Supported Mo oxides may exhibit structural and catalytic properties different from those of the corresponding bulk oxides. The interaction between support and molybdenum oxide stabilizes a particular structure that would otherwise not be available for investigations under reaction conditions. Hexagonal MoO₃ supported on SBA-15 is more stable than bulk hex-MoO₃ and more active and selective in the oxidation of propene to acrolein than the reference α -MoO₃. Moreover, hex-MoO₃–SBA-15 is capable of directly oxidizing propene to acrylic acid without additional metal sites. Thus, the electronic and geometric structure of the Mo oxide under reaction conditions may serve as lead structure for future function property correlations of Mo based oxidation catalysts.

Acknowledgments

HASYLAB, Hamburg is acknowledged for providing beamtime for this work. We are grateful to A. Hahn and A. Stys

for participating in the XAS measurements and to O. Timpe, Fritz-Haber-Institut, Berlin, for providing the hexagonal MoO₃ reference sample. The authors acknowledge the German Research Foundation (DFG) for financial support.

References

- [1] J.-D. Guo, P.Yu. Zavalij, M.S. Whittingham, *Eur. J. Solid State Inorg. Chem.* 31 (1994) 833–842.
- [2] L. Kihlberg, *Arkiv Kemi* 21 (40) (1963) 427–437; L. Kihlberg, *Acta Chem. Scand.* 23 (1969) 1834–1835.
- [3] M. Hatano, A. Kayou, US patent 5,049,692 (1991).
- [4] T. Ushikubo, K. Oshima, A. Kayou, M. Hatano, *Stud. Surf. Sci. Catal.* 112 (1997) 473–480.
- [5] R.K. Grasselli, D.J. Buttrey, P. DeSanto Jr., J.D. Burrington, C.G. Lugmair, A.F. Volpe, T. Weingand, *Catal. Today* 91–92 (2004) 251–258.
- [6] S. Breiter, M. Estenfelder, H.-G. Lintz, A. Tenten, H. Hibst, *Appl. Catal. A* 134 (1996) 81–89.
- [7] O. Ovsitser, Y. Uchida, G. Mestl, G. Weinberg, A. Blume, J. Jäger, M. Dieterle, H. Hibst, R. Schlögl, *J. Mol. Catal. A* 185 (2002) 291–303.
- [8] T. Ressler, R.E. Jentoft, J. Wienold, T. Neisius, *J. Catal.* 210 (2002) 67–83.
- [9] T. Ressler, J. Wienold, R.E. Jentoft, F. Girgsdies, *Eur. J. Inorg. Chem.* 2 (2003) 301–312.
- [10] D.Y. Zhao, Q.S. Huo, J.L. Feng, B.F. Chmelka, G.D. Stucky, *J. Am. Chem. Soc.* 120 (1998) 6024.
- [11] D. Zhao, J. Feng, Q. Huo, N. Melosh, G.H. Fredrickson, B.F. Chmelka, G.D. Stucky, *Science* 279 (1998) 548.
- [12] D.E. Keller, B.M. Weckhuysen, D.C. Koningsberger, *J. Phys. Chem. B* 110 (29) (2006) 14313.
- [13] B.M. Weckhuysen, D.E. Keller, *Catal. Today* 78 (2003) 25–46.
- [14] P. Topka, H. Balcar, J. Rathousky, N. Zilkova, F. Verpoort, J. Cejka, *Microporous Mesoporous Mater.* 96 (2006) 44–54.
- [15] G. Murali Dhara, G. Muthu Kumarana, Manoj Kumara, K.S. Rawata, L.D. Sharma, B. David Rajub, K.S. Rama Rao, *Catal. Today* 99 (2005) 309–314.
- [16] Z. Huang, T. Vitoya, D. Deng, H. Modrow, W. Bensch, T. Ressler, *J. Mater. Sci.* 43 (2008) 244–253.
- [17] S. Knobl, Ph.D. thesis, Technical University, Berlin (2004).
- [18] T. Ressler, *J. Synch. Rad.* 5 (1998) 118–122.
- [19] J.J. Rehr, C.H. Booth, F. Bridges, S.I. Zabinsky, *Phys. Rev. B* 49 (1994) 12347–12350.
- [20] T. Ressler, S.L. Brock, J. Wong, S.L. Suib, *J. Phys. Chem. B* 103 (1999) 6407–6420.
- [21] J. Wienold, R.E. Jentoft, T. Ressler, *Eur. J. Inorg. Chem.* 6 (2003) 1058–1071.
- [22] T. Ressler, O. Timpe, F. Girgsdies, J. Wienold, T. Neisius, *J. Catal.* 231 (2005) 279–291.
- [23] T. Ressler, O. Timpe, *J. Catal.* 247 (2007) 231–237.
- [24] C.H. Bamford (Ed.), *Comprehensive Chemical Kinetics*, vol. 2, Elsevier, Amsterdam, 1968.

5 Conclusions

i) Cobalt and nickel promoted (W)MoS₂ catalysts supported on SBA-15 were investigated with respect to the influence of the thiosalt precursor, the activation method, the impregnation method as well as the type of the support material (different pore sizes, Ti modified) onto the HDS performance applying DBT as model molecule. The supported catalysts prepared by the solvent evaporation/calcination route show significantly lower DBT HDS activity with respect to the catalysts derived from the filtration/calcination method. The reason of the low HDS activity is a poor dispersion of the catalytically active MoS₂. It was demonstrated that the filtration/calcination route is not suitable for the preparation of SBA-15 supported WS₂ catalysts due to weak metal-support interaction.

The synergetic effect of the promoters Co and Ni is demonstrated to be strongly correlated to the nature of the thiosalt precursors and the mode of activation. The *ex-situ* decomposition of ATM precursors in H₂/N₂ leads to the generation of HDS catalysts with a comparable activity to a commercial HDS catalyst. This result is surprising because a significant pore blocking and a pronounced MoS₂ stacking were observed. It was claimed in the literature that catalysts with a very low number of MoS₂ slabs are required for high active materials. But the present results suggest that a low MoS₂ stacking is not a prerequisite for a good HDS performance and also not a sign of deactivation or lower activity. The presence of large amount of CUS could be responsible for the high HDS activity and strong preference for the DDS pathway observed for the catalysts prepared during the present work. The study of the selectivity change of the (Co)MoS₂/SBA-15 catalysts with respect to the pore size of the SBA-15 support has shown that a confinement effect is present which is not a dominating effect for the selectivity. The strong improvement for the DDS pathway was not observed for NiMo/SBA-15 catalysts suggesting that the active site for HYD is different from that for HDS.

Furthermore, the *ex-situ* activation of the catalytic material is not beneficial for the preparation of HDS active phases when a carbon containing thiomolybdate is employed as precursor. The low HDS performance can be ascribed to the presence of an unfavorable MoS₂ morphology such as big needle-like aggregates and closed shell structures (nano-onions). In contrast, the *in-situ* activation mode during the HDS reaction is a very promising way for the preparation of NiMo/SBA-15 catalysts. For CoMo/SBA-15

catalysts, the *in-situ* activation resulted also in an enhanced synergetic effect of Co when a carbon containing thiosalt precursor (TMATM) is used. The improved HDS performance may be associated with the positive carbon effect.

ii) For MoO₃/SBA-15, the stable α -MoO₃ phase was observed at high Mo-loadings above 13 wt.%. HRTEM, X-ray patterns and N₂ isotherms evidence that the mesoporous structure of SBA-15 is maintained after the impregnation with MoO₃ species and HAADF images clearly show that the MoO₃ particles are located inside the pores of SBA-15. Interestingly, the generation of the metastable hexagonal MoO₃ modification has been confirmed by EXFAS investigations. The stabilized hex-MoO₃-SBA-15 exhibits an unexpected high catalytic activity and selectivity for the propene oxidation reaction. The use of hex-MoO₃-SBA-15 as catalyst leads interestingly to the formation of acrylic acid which is normally only observed applying MoO₃ catalysts which contain additional promoters like V, Te and Nb. The stabilized structure of hexagonal MoO₃ supported on SBA-15 possesses an open channel structure similar to those of the highly active Mo₅O₁₄ or MoVNbTe catalysts. Hence, the structure of molybdenum oxides might be the most important factor for the synthesis of new catalysts.

6 Appendix

6.1 Acknowledgements

The present work was performed in the Institute for Inorganic Chemistry at the Christian-Albrechts-Universität zu Kiel. By this way it is my pleasure to acknowledge every person who was very helpful in any situation during the PhD thesis.

First of all, I thank Prof. Dr. Wolfgang Bensch for the opportunity of working on this highly interesting topic, for helpful suggestions, rich discussions and all his support during the work. I am very proud of his supervision.

To the whole working group I would like to thank for all the help and support they gave me and the nice moments we shared together. In particular I thank: Dr. Teske, Dr. Wu, Dr. Wontcheu and Dr. Poisot.

To Mrs. Uschi Cornelissen and Mrs. Stefanie Pehlke I thank for the spectroscopic studies and CHNS-analysis performed.

I thank PD Dr. L. Kienle for the nice HRTEM measurements. Many thanks also to Dr. G. Alonso and Mr. C. Ornelas for the HDS catalytic tests and to Prof. Dr. T. Ressler for the EXAFS evaluation and the catalytic activity test of propene oxidation. I also acknowledge the help of Dr. T. Vitova and PD Dr. H. Modrow who have collected the EXAFS data of the MoO₃-SBA-15 samples.

I greatly thank my wife, Li Han, for her love and her consistent support during my PhD work.

6.2 List of Publications

G. Friedrichs, M. Colberg, M. Fikri, **Z.-D. Huang**, J. Neumann, F. Temps, Validation of an extended Simultaneous Kinetics and Ringdown Model by Measurements of the Reaction $\text{NH}_2 + \text{NO}$. *J. Phys. Chem. A*, **2005**, *109*, 4785-4795.

Z.-D. Huang, W. Bensch, W. Sigle, P. A. van Aken, L. Kienle, T. Vitoya, H. Modrow, T. Ressler, The modification of MoO_3 nanoparticles supported on mesoporous SBA-15: characterization using X-ray scattering, N_2 physisorption, transmission electron microscopy, high-angle annular darkfield technique, Raman and XAFS spectroscopy, *J. Mater. Sci.* **2008**, *43*, 244-253.

Z.-D. Huang, W. Bensch, L. Kienle, S. Fuentes, G. Alonso, C. Ornelas, SBA-15 as support for MoS_2 and Co- MoS_2 Catalysts derived from Thiomolybdate Complexes in the Reaction of HDS of DBT, *Catal. Lett.* **2008**, *122*, 57-67.

T. Ressler, A. Walter, **Z.-D. Huang**, W. Bensch, Structure and Properties of a Supported MoO_3 -SBA-15 Catalyst for Selective Oxidation of Propene, *J. Catal.*, **2008**, *254*, 170-179.

Z.-D. Huang, W. Bensch, L. Kienle, S. Fuentes, G. Alonso, C. Ornelas, Preparation and Characterization of SBA-15 supported Cobalt-Molybdenum Sulfide Catalysts for HDS reaction: an all Sulfide Route to Hydrodesulfurization Catalysts, *Catal. Lett.* **2008**, accepted.

Z.-D. Huang, W. Bensch, L. Kienle, S. Fuentes, G. Alonso, C. Ornelas, SBA-15 as support for Ni- MoS_2 HDS Catalysts derived from Sulfur-containing Molybdenum and Nickel Complexes in the Reaction of HDS of DBT: an all Sulfide Route, *Catal. Lett.* submitted.

Z.-D. Huang, W. Bensch, L. Kienle, S. Fuentes, J. Bocarando, G. Alonso, C. Ornelas, SBA-15 as Support for Ni- MoS_2 HDS catalysts derived from Sulfur-containing

Molybdenum and Nickel Complexes: Effect of Activation mode, in preparation.

Z.-D. Huang, W. Bensch, L. Kienle, S. Fuentes, J. Bocarando, G. Alonso, C. Ornelas, Comparative study of Co-MoS₂/SBA-15 catalysts prepared by ex-situ/in-situ of Sulfur-containing Molybdenum and Cobalt Complexes, in preparation.

6.3 Curriculum Vitae

Name: Zhida Huang
Date of Birth: November 09th, 1977
Place of Birth: Guangdong, China
Nationality: Chinese

Education in China

09/1990 - 02/1992 Wuyun-Middleschool
03/1992 - 07/1996 Hepo-Middleschool
09/1996 - 07/1999 Guangdong University of Technology
Department: Chemical Engineering
Specialty: Industrial Analysis

Education in Germany

11/1999 - 03/2000 Volkshochschule Kiel, German course
04/2000 - 04/2001 University of Kiel, German course
04/2001 - 03/2005 University of Kiel, Diplom study
08/2004 - 03/2005 Department: Physical Chemistry
Diploma thesis: Untersuchung der Radikale OH, CH₃O
und HCCO mittels UV Cavity Ringdown Spektroskopie

04/2005- 07/2008 University of Kiel
Department: Inorganic Chemistry
PhD dissertation: Characterization and Catalytic
Activity Study of SBA-15-supported MoO₃, MoS₂, Ni
or Co promoted MoS₂ and Co promoted WS₂

References

- [1] C. T. Kresge, M. E. Leonowicz, W. J. Roth, J. C. Vartuli, and J. S. Beck, *Nature*, pp. 710–712, 1992.
- [2] J. S. Beck, J. C. Vartuli, W. J. Roth, M. E. Leonowicz, C. T. Kresge, K. D. Schmitt, C. T.-W. Chu, D. H. Olson, E. W. Sheppard, S. B. McCullen, J. B. Higgins, and J. L. Schlenker, *J. Am. Chem. Soc.*, vol. 114, pp. 10834–10843, 1992.
- [3] D.-Y. Zhao, Q.-S. Huo, J.-L. Feng, B. F. Chmelka, and G. D. Stucky, *J. Am. Chem. Soc.*, vol. 120, pp. 6024–6036, 1998.
- [4] D.-Y. Zhao, J.-L. Feng, Q.-S. Huo, N. Melosh, G. H. Fredrickson, B. F. Chmelka, and G. D. Stucky, *Science*, vol. 279, pp. 548–552, 1998.
- [5] F. L. Plantenga and R. G. Leliveld, *Appl. Catal. A: Gen.*, vol. 248, pp. 1–7, 2003.
- [6] M. Poisot, PhD thesis, Kiel, 2007.
- [7] R. A. Sánchez-Delgado, *Organometallic modeling of the hydrodesulfurization and hydrodenitrogenation reactions*, Kluwer Academic Publishers, 2002.
- [8] C.-S. Song, *Catal. Today*, vol. 86, pp. 211–263, 2003.
- [9] V. Rabarihoela-Rakotovoao, S. Brunet, G. Perot, and F. Diehl, *Appl. Catal. A: Gen.*, vol. 306, pp. 34–44, 2006.
- [10] H. Topsøe, B. S. Clausen, and F. E. Massoth, *Hydrotreating catalysis science and technology*, Springer-Verlag, 1996.
- [11] H. Topsøe and B. S. Clausen, *Catal. Rev.-Sci. Eng.*, vol. 26, pp. 395–420, 1984.
- [12] X. Carrier, J. F. Lambert, and M. Che., *J. Am. Chem. Soc.*, vol. 119, pp. 10137–10146, 1997.
- [13] R. Candia, O. Sørensen, J. Villadsen, N.-Y. Topsøe, B. S. Clausen, and H. Topsøe, *Bull. Soc. Chim. Belg.*, vol. 93, pp. 763–770, 1984.
- [14] M. Breyse, P. Afanasiev, C. Geantet, and M. Vrinat, *Catal. Today*, vol. 86, pp. 5–16, 2003.
- [15] M. J. B. Souza, B. A. Marinkovic, P. M. Jardim, A. S. Araujo, A. M. G. Pedrosa, and R. R. Souza, *Appl. Catal. A: Gen.*, vol. 316, pp. 212–218, 2007.
- [16] X. Li, A.-J. Wang, S. Zhang, Y.-Y. Chen, and Y.-K. Hu, *Appl. Catal. A: Gen.*, vol. 316, pp. 134–141, 2007.
- [17] D. Eliche-Quesada, E. Rodriguez-Castellon, and A. Jimenez-Lopez, *Micropor. Mesopor. Mater.*, vol. 99, pp. 268–278, 2007.
- [18] S.-K. Song, Y.-H. Wang, and S.-K. Ihm, *Catal. Today*, vol. 111, pp. 194–198, 2006.
- [19] M. Hussain, S.-K. Song, J.-H. Lee, and S.-K. Ihm, *Ind. Eng. Chem. Res.*, vol. 45, pp. 536–543, 2006.
- [20] J. R. Grzechowiak, K. Mrozinska, A. Masalska, J. Goralski, J. Rynkowski, and W. Tylus, *Catal. Today*, vol. 114, pp. 272–280, 2006.

-
- [21] M. J. B. Souza, A. S. Araujo, A. M. G. Pedrosa, J. M. F. B. Aquino, D. M. A. Melo, and A. O. S. Silva, *Stud. Surf. Sci. Catal.*, vol. 156, pp. 755–760, 2005.
- [22] J. M. Herrera, J. Reyes, P. Roquero, and T. Klimova, *Micropor. Mesopor. Mater.*, vol. 83, pp. 283–291, 2005.
- [23] T. Chiranjeevi, G. M. Kumaran, J. K. Gupta, and G. M. Dhar, *Catal. Comm.*, vol. 6, pp. 101–106, 2005.
- [24] R. Silva-Rodrigo, C. Calderon-Salas, J. A. Melo-Banda, J. M. Dominguez, and A. Vazquez-Rodriguez, *Catal. Today*, vol. 98, pp. 123–129, 2004.
- [25] P. Schacht, L. Norena-Franco, J. Ancheyta, S. Ramirez, I. Hernandez-Perez, and L.A. Garcia, *Catal. Today*, vol. 98, pp. 115 – 121, 2004.
- [26] U. T. Turaga and C.-S. Song, *Catal. Today*, vol. 86, pp. 129–140, 2003.
- [27] X. Li, A.-J. Wang, Z.-C. Sun, C. Li, J. Ren, B. Zhao, Y. Wang, Y.-Y. Chen, and Y.-K. Hu, *Appl. Catal. A: Gen.*, vol. 254, pp. 319–326, 2003.
- [28] A.-J. Wang, Y. Wang, T. Kabe, Y.-Y. Chen, A. Ishihara, W.-H. Qian, and P.-J. Yao, *J. Catal.*, vol. 210, pp. 319–327, 2002.
- [29] X. Li, A.-J. Wang, Y. Wang, Y.-Y. Chen, Y.-H. Liu, and Y.-K. Hu, *Catal. Lett.*, vol. 84, pp. 107–113, 2002.
- [30] A.-J. Wang, Y. Wang, T. Kabe, Y.-Y. Chen, A. Ishihara, and W.-H. Qian, *J. Catal.*, vol. 199, pp. 19–29, 2001.
- [31] M. V. Landau, L. Vradman, M. Herskowitz, Y. Koltypin, and A. Gedanken, *J. Catal.*, vol. 201, pp. 22–36, 2001.
- [32] K. M. Reddy, B.-L. Wei, and C.-S. Song, *Catal. Today*, vol. 43, pp. 261–272, 1998.
- [33] L. Vradman, M. V. Landau, M. Herskowitz, V. Ezersky, M. Talianker, S. Nikitenko, Y. Koltypin, and A. Gedanken, *J. Catal.*, vol. 213, pp. 163–175, 2003.
- [34] G. M. Dhar, G. M. Kumaran, M. Kumar, K. S. Rawat, L. D. Sharma, B. D. Raju, and K. S. R. Rao, *Catal. Today*, vol. 99, pp. 309–314, 2005.
- [35] O. Y. Gutierrez, G. A. Fuentes, C. Salcedo, and T. Klimova, *Catal. Today*, vol. 116, pp. 485–497, 2006.
- [36] O. Y. Gutierrez, D. Valencia, G. A. Fuentes, and T. Klimova, *J. Catal.*, vol. 249, pp. 138–151, 2007.
- [37] G. M. Kumaran, S. Garg, K. Soni, M. Kumar, L. D. Sharma, G. M. Dhar, and K. S. R. Rao, *Appl. Catal. A: Gen.*, vol. 305, pp. 123–129, 2006.
- [38] S. Eijsbouts, S. W. Mayo, and K. Fujita, *Appl. Catal. A: Gen.*, vol. 322, pp. 58–66, 2007.
- [39] F. Besenbacher, M. Brorson, B. S. Clausen, S. Helveg, B. Hinnemann, J. Kibsgaard, J. V. Lauritsen, P. G. Moses, J. K. Nørskov, and H. Topsøe, *Catal. Today*, vol. 130, pp. 86–96, 2008.
- [40] J. V. Lauritsen, J. Kibsgaard, G. H. Olesen, P. G. Moses, B. Hinnemann, S. Helveg, J. K. Nørskov, B. S. Clausen, H. Topsøe, E. Lægsgaard, and F. Besenbacher, *J. Catal.*, vol. 249, pp. 218–231, 2007.

-
- [41] J.V. Lauritsen, M. Nyberg, J. K. Nørskov, B.S. Clausen, H. Topsøe, E. Lægsgaard, and F. Besenbacher, *J. Catal.*, vol. 224, p. 94-106, 2004.
- [42] H. Topsøe and B. S. Clausen, *Appl. Catal.*, vol. 25, pp. 273-293, 1986.
- [43] M. F. L. Johnson, A. P. Voss, S. H. Bauer, and N.-S. Chiu, *J. Catal.*, vol. 98, pp. 51-63, 1986.
- [44] N.-S. Chiu, S. H. Bauer, and M. F. L. Johnson, *J. Catal.*, vol. 98, pp. 32-50, 1986.
- [45] N.-S. Chiu, M. F. L. Johnson, and S. H. Bauer, *J. Catal.*, vol. 113, pp. 281-294, 1988.
- [46] C. Thomazeau, C. Geantet, M. Lacroix, M. Danot, V. Harle, and P. Raybaud, *Appl. Catal. A: Gen.*, vol. 322, pp. 92-97, 2007.
- [47] S. Cristol, J.-F. Paul, E. Payen, D. Bougeard, F. Hutschka, and S. Clemendot, *J. Catal.*, vol. 224, pp. 138-147, 2004.
- [48] R. Nava, R. A. Ortega, G. Alonso, C. Ornelas, B. Pawelec, and J. L. G. Fierro, *Catal. Today*, vol. 127, pp. 70-84, 2007.
- [49] M. Karroua, H. Matralis, P. Grange, and B. Delmon, *J. Catal.*, vol. 139, pp. 371-374, 1993.
- [50] M. Daage and R. R. Chianelli, *J. Catal.*, vol. 149, pp. 414-427, 1994.
- [51] C. Glasson, C. Geantet, M. Lacroix, F. Labruyere, and P. Dufresne, *J. Catal.*, vol. 212, pp. 76-85, 2002.
- [52] H. Nava, C. Ornelas, A. Aguilar, G. Berhault, S. Fuentes, and G. Alonso, *Catal. Lett.*, vol. 86, pp. 257-265, 2003.
- [53] K. Al-Dalama, B. Aravind, and A. Stanislaus, *Appl. Catal. A: Gen.*, vol. 296, pp. 49-53, 2005.
- [54] L. Coulier, G. Kishan, J. A. R. van Veen, and J. W. Niemantsverdriet, *J. Phys. Chem. B*, vol. 106, pp. 5897-5906, 2002.
- [55] G. Kishan, L. Coulier, V. H. J. de Beer, J. A. R. van Veen, and J. W. Niemantsverdriet, *J. Catal.*, vol. 196, pp. 180-189, 2000.
- [56] S. M. A. M. Bouwens, F. B. M. Vanzon, M. P. Vandijk, A. M. Vanderkraan, V. H. J. Debeer, J. A. R. Vanveen, and D. C. Koningsberger, *J. Catal.*, vol. 146, pp. 375-393, 1994.
- [57] S. Eijsbouts, L. C. A. van den Oetelaar, and R. R. van Puijenbroek, *J. Catal.*, vol. 229, pp. 352-364, 2005.
- [58] E. Rödel, PhD thesis, Berlin, 2006.
- [59] R. K. Grasselli, *Topic Catal.*, vol. 21, pp. 79-88, 2002.
- [60] R. K. Grasselli, *Topic Catal.*, vol. 15, pp. 93-101, 2001.
- [61] Z. L. Wang, Ed., *Characterization of nanophase materials*, Wiley-VCH Verlag, 2000.
- [62] J.-D. Grunwaldt, S. Hannemann, J. Göttlicher, S. Mangold, M. A. Denecke, and A. Baiker, *Phys. Scr.*, vol. T115, pp. 769-772, 2005.
- [63] M. Lemonnier, O. Collet, C. Depautex, J.-M. Esteva, and D. Raoux, *Nucl. Instrum. Methods*, vol. 152, pp. 109-111, 1978.

-
- [64] T. Allen, *Particle size measurement*, Chapman and Hall, 1997.
- [65] I. Langmuir, *J. Am. Chem. Soc.*, vol. 40, pp. 1361–1403, 1918.
- [66] S. Brunauer, P. H. Emmett, and E. Teller, *J. Am. Chem. Soc.*, vol. 60, pp. 309–319, 1938.
- [67] E. D. Barret, L. G. Joyner, and P. P. Halenda, *J. Am. Chem. Soc.*, vol. 73, pp. 373–380, 1951.
- [68] R. Prins, A. Egorova, A. Röthlisberger, Y. Zhao, N. Sivasankar, and P. Kukula, *Catal. Today*, vol. 111, pp. 84–93, 2006.
- [69] J. L. Brito, F. Severino, N. N. Delgado, and J. Laine, *Appl. Catal. A: Gen.*, vol. 173, pp. 193–199, 1998.
- [70] P. Van Der Voort, P. I. Ravikovitch, K. P. De Jong, M. Benjelloun, E. Van Bavel, A. H. Janssen, A. V. Neimark, B. M. Weckhuysen, and E. F. Vansant, *J. Phys. Chem. B*, vol. 106, pp. 5873–5877, 2002.